

¹ SEARCH FOR EXOTIC HIGGS DECAYS TO LIGHT
² NEUTRAL SCALARS IN FINAL STATES WITH
³ BOTTOM QUARKS AND TAU LEPTONS

⁴ KA YU STEPHANIE KWAN

⁵ A DISSERTATION
⁶ PRESENTED TO THE FACULTY
⁷ OF PRINCETON UNIVERSITY
⁸ IN CANDIDACY FOR THE DEGREE
⁹ OF DOCTOR OF PHILOSOPHY

¹⁰ NOT YET RECOMMENDED FOR ACCEPTANCE
¹¹ BY THE DEPARTMENT OF PHYSICS
¹² ADVISER: ISOBEL OJALVO

¹³ MAY 2024

¹⁴

© Copyright by Ka Yu Stephanie Kwan, 2024.

¹⁵

All Rights Reserved

Abstract

Open questions in particle physics may be addressed by the existence of an extended Higgs sector beyond the Standard Model Higgs boson with mass 125 GeV, which was discovered in 2012 at the Large Hadron Collider (LHC) by the CMS and ATLAS experiments. Many properties of a potential extended Higgs sector remain unconstrained by current measurements, making direct searches of exotic Higgs decays a powerful probe of new physics. The decay of the 125 GeV Higgs boson into two light neutral scalar particles ($h \rightarrow aa$) is allowed in extensions of the Standard Model, such as Two Higgs Doublet Models extended with a scalar singlet (2HDM+S). We present a search at CMS for exotic decays of the 125 GeV Higgs boson to two light neutral scalars, which decay to two bottom quarks and two tau leptons ($h \rightarrow aa \rightarrow bb\tau\tau$). This analysis is combined with a different search where the light scalars decay to two bottom quarks and two muons. The results from the $bb\tau\tau$ analysis and the combined analyses are interpreted in 2HDM+S scenarios. In a different extension of the Standard Model, the Two Real Singlet Model (TRSM), the 125 GeV Higgs boson can decay to two light scalars with unequal mass ($h \rightarrow a_1a_2$). This decay has not been searched for to date at CMS. We present ongoing work on a search for $h \rightarrow a_1a_2$, where the a_2 decays into two a_1 , resulting in four bottom quarks and two tau leptons in the final state, in the $\mu\tau_h$ channel of the $\tau\tau$ decay. Such searches for rare processes will directly benefit from the increased datasets that will be generated by the High-Luminosity LHC (HL-LHC), which is scheduled to increase the LHC’s number of simultaneous proton-proton collisions by a factor of five to seven. To contribute to the performance of the CMS Level-1 Trigger in selecting collisions with interesting physics, this thesis presents an upgraded algorithm for reconstructing electrons and photons in the barrel calorimeter, which will use information with higher spatial granularity to distinguish genuine electrons and photons from background.

⁴²

Acknowledgements

⁴³ Placeholder acknowledgements.

⁴⁵ Contents

⁴⁶	Abstract	iii
⁴⁷	Acknowledgements	iv
⁴⁸	List of Tables	xi
⁴⁹	List of Figures	xiii
⁵⁰	1 Introduction	1
⁵¹	1.1 History of the Standard Model	1
⁵²	1.2 The Standard Model as a gauge theory	3
⁵³	1.3 The Higgs Mechanism	6
⁵⁴	1.4 Two-Higgs Doublet Models	8
⁵⁵	1.5 Two Real Singlet Model	11
⁵⁶	2 The Large Hadron Collider and the CMS Experiment	15
⁵⁷	2.1 The Large Hadron Collider	16
⁵⁸	2.2 Luminosity and pileup	17
⁵⁹	2.3 The High-Luminosity LHC	20
⁶⁰	2.4 The CMS Detector	21
⁶¹	2.5 Sub-detectors of CMS	22
⁶²	2.5.1 Inner tracking system	23
⁶³	2.5.2 ECAL	24
⁶⁴	2.5.3 HCAL	25

65	2.5.4 Muon detectors	27
66	2.5.5 The Level-1 Trigger	28
67	2.5.6 The High-Level Trigger	31
68	2.5.7 Particle reconstruction	32
69	2.5.8 Data storage and computational infrastructure	32
70	3 The Phase-2 Upgrade of CMS	33
71	3.1 High-Luminosity LHC and CMS	33
72	3.2 The Phase-2 Level-1 Trigger	33
73	3.3 Standalone Barrel Calorimeter electron/photon reconstruction	36
74	3.3.1 Phase-2 geometry of the ECAL Barrel trigger	36
75	3.3.2 Phase-2 electron/photon reconstruction algorithm	37
76	4 Datasets and Monte Carlo samples	46
77	4.1 Datasets used	46
78	4.2 Monte Carlo samples	46
79	4.3 Embedded samples	48
80	5 Object reconstruction and corrections applied	51
81	5.1 Object reconstruction	51
82	5.1.1 Taus	51
83	5.1.2 Muons	55
84	5.1.3 Electrons	56
85	5.1.4 Jets	58
86	5.1.5 B-flavored jets	59
87	5.2 Reconstruction of the $\tau\tau$ mass	60
88	5.2.1 Original SVFit “standalone”: maximum likelihood	61
89	5.2.2 “Classic SVFit” with matrix element	62
90	5.2.3 FastMTT: optimized SVFit	63

91	5.3 Corrections applied to simulation	63
92	5.3.1 Tau energy scale	64
93	5.3.2 Muon energy scale	64
94	5.3.3 Electron energy scale	65
95	5.3.4 τ_h identification efficiency	66
96	5.3.5 Trigger efficiencies	66
97	5.3.6 Tau trigger efficiencies	66
98	5.3.7 Single muon trigger efficiencies	67
99	5.3.8 Single electron trigger efficiencies	68
100	5.3.9 $e\mu$ cross-trigger efficiencies	69
101	5.3.10 Electrons and muons faking τ_h : energy scales	70
102	5.3.11 Electrons and muons faking τ_h : misidentification efficiencies .	71
103	5.3.12 Electron ID and tracking efficiency	72
104	5.3.13 Muon ID, isolation, and tracking efficiencies	73
105	5.3.14 Recoil corrections	74
106	5.3.15 Drell-Yan corrections	75
107	5.3.16 Pileup reweighing	75
108	5.3.17 Pre-firing corrections	76
109	5.3.18 Top p_T spectrum reweighing	77
110	5.3.19 B-tagging efficiency	77
111	5.3.20 Jet energy resolution and jet energy smearing	77
112	6 Event selection	79
113	6.1 General procedure for all channels	79
114	6.2 Event selection in the $\mu\tau_h$ channel	80
115	6.3 Event selection in the $e\tau_h$ channel	82
116	6.4 Event selection in the $e\mu$ channel	83
117	6.5 Extra lepton vetoes in all channels	84

¹¹⁸	7 Background estimation	88
¹¹⁹	7.1 Z+jets	88
¹²⁰	7.2 W+jets	89
¹²¹	7.3 $t\bar{t}$ + jets	89
¹²²	7.4 Single top	90
¹²³	7.5 Diboson	90
¹²⁴	7.6 Standard Model Higgs	90
¹²⁵	7.7 Jet faking τ_h	91
¹²⁶	7.8 QCD multijet background	92
¹²⁷	8 Systematic uncertainties	94
¹²⁸	8.1 Uncertainties associated with physics objects	95
¹²⁹	8.1.1 Uncertainties in the lepton energy scales	95
¹³⁰	8.1.2 Uncertainties from other lepton corrections	96
¹³¹	8.1.3 Uncertainties from jet energy scale and resolution	96
¹³²	8.1.4 Uncertainties from b-tagging scale factors	97
¹³³	8.1.5 Uncertainties from MET	98
¹³⁴	8.2 Uncertainties associated with samples used	98
¹³⁵	8.3 Other uncertainties	99
¹³⁶	8.4 Pulls and impacts	99
¹³⁷	9 Event categorization and signal extraction	101
¹³⁸	9.1 B-tag jet multiplicity	101
¹³⁹	9.2 DNN-based event categorization	101
¹⁴⁰	9.3 Methodology for signal extraction	104
¹⁴¹	9.3.1 Model building and parameter estimation	105
¹⁴²	9.3.2 Hypothesis testing	107
¹⁴³	9.3.3 Confidence intervals	108

144	9.3.4 Profile likelihood ratio	110
145	9.3.5 Modified frequentist method: CL_S	111
146	10 Results	112
147	10.1 Results from $bb\tau\tau$	112
148	10.2 Combination with $bb\mu\mu$ final state	114
149	11 Asymmetric exotic Higgs decays	125
150	11.1 Signal masses	125
151	11.2 Cascade scenario signal studies	126
152	11.3 Current control plots for $\mu\tau_h$ channel	128
153	12 Conclusion and outlook	132

¹⁵⁴ List of Tables

¹⁵⁵	4.1	Expected event composition after selecting two muons in the embedded technique, before additional cuts (i.e. inclusive), and after adding a requirement on the di-muon mass $m_{\mu\mu} > 70$ GeV, or a requirement on the number of b-tag jets in the event.	50
¹⁵⁶	5.1	Energy scales applied to genuine hadronic tau decays τ_h by data-taking year/era and decay mode, along with systematic errors.	64
¹⁵⁷	5.2	Energy scales and systematic errors applied to genuine muons.	65
¹⁵⁸	5.3	Energy scales and systematic errors applied to electrons in embedded samples by data-taking year/era.	66
¹⁵⁹	5.4	Tau ID efficiency for the DeepTau vs. jet medium working point, with central, up, and down values for 2018, binned in the tau p_T	66
¹⁶⁰	5.5	Energy scales and up/down systematic uncertainties applied to electrons misidentified as hadronic taus.	70
¹⁶¹	5.6	Tau mis-identification efficiency for the DeepTau Tight and Very Loose (VLoose) working points vs. muons in 2018.	72
¹⁶²	5.7	Tau mis-identification efficiency for the DeepTau Tight and Very Loose (VLoose) working points vs. electrons in 2018.	72

172	6.1	Trigger thresholds used for the leptons in the $bb\mu\mu$ analysis and the	
173		$bb\tau\tau$ analysis (the focus of this work). The thresholds for the three $bb\tau\tau$	
174		channels ($e\mu$, $e\tau_h$, and $\mu\tau_h$) are listed separately, with some channels	
175		and years taking the logical OR of two triggers with different thresholds.	80
176	6.2	High-Level Trigger (HLT) paths used to select data and simulation	
177		events in 2016 for the three $\tau\tau$ channels.	85
178	6.3	High-Level Trigger (HLT) paths used to select data and simulation	
179		events in 2017 for the three $\tau\tau$ channels.	85
180	6.4	High-Level Trigger (HLT) paths used to select data and simulation	
181		events in 2018 for the three $\tau\tau$ channels. In 2018 a HLT trigger path	
182		using the hadron plus strips (HPS) tau reconstruction algorithm be-	
183		came available.	86
184	9.1	Event categorization based on DNN scores for events with exactly 1	
185		b-tag jet (1bNN), for the three $\tau\tau$ channels and three eras.	104
186	9.2	Event categorization based on DNN scores for events with 2 b-tag jets	
187		(2bNN), for the three $\tau\tau$ channels and three eras.	105

¹⁸⁸ **List of Figures**

189	1.1	Table of Standard Model particles showing the grouping of the fermions into three generations of matter and the bosons, responsible for carrying the three fundamental forces in the Standard Model. The masses, charges, and spins of the particles are shown. The antimatter counter- parts of the fermions are not shown. The possible interactions between the fermions and gauge bosons are highlighted.	3
190	1.2	An illustration of the Higgs potential.	8
191	1.3	Branching ratios of a singlet-like pseudoscalar in Type II 2HDM+S for $\tan \beta = 0.5$ (left) and $\tan \beta = 5$ (right).	11
192	1.4	Benchmark plane BP1 for benchmark scenario 1, for the decay signa- ture $h_{125} \rightarrow h_1 h_2$ with $h_{125} \equiv h_3$, defined in the (M_1, M_2) plane. . . .	14
193	2.1	Aerial view of the Large Hadron Collider (LHC).	18
194	2.2	Distribution of the mean number of inelastic collisions per bunch cross- ing (pileup) in data, for proton-proton collisions in 2016-2018	20
195	2.3	Sketch of particle trajectories of muons, electrons, charged and neutral hadrons, and photons in a transverse cross-section of the CMS detector.	22
196	2.4	Cross section of the current Phase-1 CMS tracker.	24
197	2.5	Longitudinal view of the CMS detector showing the hadron calorimeter barrel (HB), endcap (HE), outer (HO), and forward (HF) calorimeters.	26

208	2.6	Layout of the CMS barrel muon drift tube (DT) chambers in one of the five wheels.	28
209			
210	2.7	Dataflow for the Phase-1 Level-1 Trigger.	29
211			
212	3.1	Functional diagram of the CMS L1 Phase-2 upgraded trigger design. .	34
213	3.2	Summary of the links between the trigger primitives, the trigger ob- jects, the Level-1 algorithms, and the physics channels in the Phase-2 menu.	37
214			
215	3.3	Schematic of the geometry of the Phase-2 ECAL barrel in the Regional Calorimeter Trigger (RCT), showing the division of the barrel region into 36 Regional Calorimeter Trigger (RCT) cards (<i>red</i>). Each card spans 17×4 towers in $\eta \times \phi$ (<i>green</i>), and each tower is 5×5 in single crystals in $\eta \times \phi$. Towers in the overlap region (<i>shaded yellow</i>) are read out to both the barrel and endcap.	40
216			
217	3.4	Schematic of two example RCT cards in the negative eta (<i>top</i>) and positive eta (<i>center</i>) regions of the ECAL barrel. Each RCT card is divided into five regions: four regions are of size 3×4 towers in $\eta \times \phi$ (<i>bottom left</i>), and a fifth smaller overlap region of size 2×4 towers (<i>bottom right</i>). Each tower is 5×5 ($\eta \times \phi$) in crystals.	41
218			
219	3.5	Schematic of the Phase-2 ECAL barrel in the Global Calorimeter Trig- ger (GCT), which will process the outputs of the Regional Calorimeter Trigger (RCT) in three cards (<i>magenta highlights</i>). Each card in the GCT processes the equivalent of sixteen RCT cards, with the center twelve being unique to that GCT card (<i>shaded pink</i>), and the remain- ing four processed in overlap with the other GCT cards.	42
220			
221			
222			
223			
224			
225			
226			
227			
228			
229			
230			
231			

232	3.6 Illustration of an example electron/photon (e/γ) cluster in the Phase-	
233	2 Level-1 Trigger standalone barrel e/γ reconstruction, in a region of	
234	15×20 crystals (3×4 towers). Each small pink square is one crystal,	
235	the highest-granularity ECAL trigger primitives available to the L1	
236	Trigger in Phase-2. The core cluster consists of the energy sum in a	
237	3×5 window of crystals, (<i>shaded light blue</i>) centered around the seed	
238	crystal (<i>red</i>). Bremsstrahlung corrections are checked in the adjacent	
239	3×5 windows in the ϕ direction (<i>shaded light yellow</i>). The relative	
240	energies in windows of size 2×5 and 5×5 in crystals (<i>dashed dark blue</i>	
241	<i>and dark red</i>) are used to compute shower shape variables to identify	
242	true e/γ objects. Lastly, an isolation sum is computed in a window of	
243	size 7×7 in towers (not shown in figure).	43
244	3.7 Efficiency of the standalone barrel e/γ reconstruction, as a function of	
245	the true electron's transverse momentum p_T	44
246	3.8 Rates of the standalone barrel e/γ reconstruction measured as a func-	
247	tion of the minimum energy (E_T) required of the reconstructed e/γ	
248	object in each event.	45
249	4.1 Cumulative delivered and recorded luminosity versus time for 2015-	
250	2018 at CMS, in proton-proton collision data only, at nominal center-	
251	of-mass energy.	47
252	4.2 Schematic view of the four main steps of the embedding technique for	
253	τ leptons.	49
254	5.1 Distributions of $m_{\tau\tau}$ reconstructed by the classic SVFit algorithm, and	
255	masses of visible tau decay products (before SVFit).	62
256	5.2 Electron/photon energy scale factors and uncertainties for 2018. . . .	65

257	5.3 Hadronic tau leg efficiency of the cross-triggers for $\mu\tau_h$ (<i>left</i>) and $e\tau_h$ (<i>right</i>) triggers as a function of offline tau p_T for 2016, 2017, and 2018.	68
258		
259	5.4 Trigger efficiencies in data (<i>top panels</i>) and ratio of efficiencies af- ter/before a HLT muon reconstruction update (<i>bottom panels</i>) for the	
260	muon in the isolated single muon trigger with threshold $p_T > 24$ GeV	
261	in the data-taking year 2018, as functions of the muon p_T (<i>left</i>) and	
262	muon $ \eta $ (<i>right</i>).	69
263		
264	5.5 Trigger efficiencies in data and the data/MC ratio for the electron in the single electron trigger with threshold $p_T > 32$ GeV in the data- taking year 2018, as functions of the electron p_T (<i>left</i>) and electron $ \eta $ (<i>right</i>).	70
265		
266	5.6 Efficiencies of the electron leg vs. p_T (<i>left</i>) and the muon log vs. η (<i>right</i>), for the HLT path with online thresholds of 12 GeV for the	
267	electron and 23 GeV for the muon, with the data-taking years 2016 through 2018 overlaid.	71
268		
269	5.7 Efficiencies in data (<i>top panels</i>) and the ratio of efficiencies in data/MC (<i>bottom panels</i>), for the electron multivariate analysis (MVA) identifi- cation (<i>left</i>) and for the Gaussian-sum filter (GSF) tracking (<i>right</i>). . .	73
270		
271	5.8 Muon identification efficiencies in 2015 data and MC as a function of the muon p_T for the loose ID (<i>left</i>) and tight ID (<i>right</i>) working points.	74
272		
273	5.9 Muon isolation efficiencies in Run-2 data as a function of the muon p_T (<i>left</i>) and $ \eta $ (<i>right</i>).	75
274		
275	5.10 Muon tracking efficiencies as a function of $ \eta $ for standalone muons in	
276	Run-2 data (<i>black</i>) and Drell-Yan (<i>blue</i>) MC simulation.	76
277		
278		
279	7.1 Leading-order Feynman diagrams of Higgs production.	91
280		
281	8.1 Top sixty impacts for the combination of all channels and years.	100

283	9.1 Schematic of the Neyman construction for confidence intervals.	109
284	10.1 Postfit final observed and expected $m_{\tau\tau}$ distributions in the $\mu\tau_h$ chan-	
285	nel, for the 1 b-tag jet and 2 b-tag jet signal and control regions.	116
286	10.2 Postfit final observed and expected $m_{\tau\tau}$ distributions in the $e\tau_h$ chan-	
287	nel, for the 1 b-tag jet and 2 b-tag jet signal and control regions.	117
288	10.3 Postfit final observed and expected $m_{\tau\tau}$ distributions in the $e\mu$ channel.	118
289	10.4 Observed 95% CL exclusion limits (<i>black, solid lines</i>) and expected 95%	
290	CL and 68% CL limits (<i>shaded yellow and green</i>) on the branching	
291	fraction $B(h \rightarrow aa \rightarrow bb\tau\tau)$ in percentages, assuming the Standard	
292	Model production for the 125 GeV Higgs (h). Limits are shown for the	
293	$\mu\tau_h$ channel (<i>top left</i>), the $e\tau_h$ channel (<i>top right</i>), and the $e\mu$ channel	
294	(<i>bottom left</i>), and lastly the combination of all three channels (<i>bottom</i>	
295	<i>right</i>) The dataset corresponds to 138 fb^{-1} of data collected in the	
296	years 2016-2018 at a center-of-mass energy 13 TeV.	119
297	10.5 Observed 95% CL upper limits on $B(h \rightarrow aa)$ in %, for the $bb\tau\tau$ final	
298	state (<i>left</i>) and $bb\mu\mu$ final state (<i>right</i>) using the full Run 2 integrated	
299	luminosity of 138 fb^{-1} in 2HDM+S type I (<i>blue</i>), type II with $\tan\beta =$	
300	2.0 (<i>orange dashed</i>), type III with $\tan\beta = 2.0$ (<i>dotted green</i>), and type	
301	IV with $\tan\beta = 0.6$ (<i>red dashed</i>).	120
302	10.6 Observed 95% CL upper limits on the branching fraction of the 125	
303	GeV Higgs boson to two pseudoscalars, $B(h \rightarrow aa)$, in percentages,	
304	as a function of the pseudoscalar mass m_a , in 2HDM+S type I (<i>blue</i>),	
305	type II with $\tan\beta = 2.0$ (<i>orange dashed</i>), type III with $\tan\beta = 2.0$	
306	<i>(dotted green)</i> , and type IV with $\tan\beta = 0.6$ (<i>red dashed</i>), for the	
307	combination of $bb\mu\mu$ and $bb\tau\tau$ channels using the full Run 2 integrated	
308	luminosity of 138 fb^{-1}	121

309	10.7 Observed 95% CL upper limits on $\mathcal{B}(h \rightarrow aa)$ in %, for the combination	
310	of $bb\mu\mu$ and $bb\tau\tau$ channels using the full Run 2 integrated luminosity	
311	of 138 fb^{-1} for Type II (<i>left</i>), Type III (<i>middle</i>), and Type IV (<i>right</i>)	
312	2HDM+S in the $\tan\beta$ vs. m_a phase space.	122
313	10.8 Summary plot of current observed and expected 95% CL limits on the	
314	branching ratio of the 125 GeV Higgs boson to two pseudoscalars, nor-	
315	malized to the Standard Model Higgs production cross-section, $\frac{\sigma(h)}{\sigma_{\text{SM}}} \times$	
316	$B(h \rightarrow aa)$, in the 2HDM+S type I scenario, obtained at CMS with	
317	data collected at 13 TeV.	122
318	10.9 Summary plot of current observed and expected 95% CL limits on the	
319	branching ratio of the 125 GeV Higgs boson to two pseudoscalars, nor-	
320	malized to the Standard Model Higgs production cross-section, $\frac{\sigma(h)}{\sigma_{\text{SM}}} \times$	
321	$B(h \rightarrow aa)$, in the 2HDM+S type II scenario with $\tan\beta = 2.0$, ob-	
322	tained at CMS with data collected at 13 TeV.	123
323	10.10 Summary plot of current observed and expected 95% CL limits on the	
324	branching ratio of the 125 GeV Higgs boson to two pseudoscalars, nor-	
325	malized to the Standard Model Higgs production cross-section, $\frac{\sigma(h)}{\sigma_{\text{SM}}} \times$	
326	$B(h \rightarrow aa)$, in the 2HDM+S type III scenario with $\tan\beta = 2.0$, ob-	
327	tained at CMS with data collected at 13 TeV.	124
328	11.1 Generator-level b-flavor jet transverse momenta p_T , for $h \rightarrow a_1 a_2$ cas-	
329	cade scenario in the $4b2\tau$ final state, for mass hypotheses $(m_{a_1}, m_{a_2}) =$	
330	$(100, 15) \text{ GeV}$ (<i>left</i>) and $(40, 20) \text{ GeV}$ (<i>right</i>). In each plot the generator-	
331	level p_T of the leading (<i>black</i>), sub-leading (<i>red</i>), third (<i>blue</i>), and	
332	fourth (<i>light green</i>) are overlaid.	127

³⁵⁵ Chapter 1

³⁵⁶ Introduction

³⁵⁷ The Standard Model is the current prevailing theoretical framework that encompasses
³⁵⁸ all known elementary particles to date and describes their interactions, yet falls short
³⁵⁹ of describing open problems in physics. Here, we describe the history of the Standard
³⁶⁰ Model and its particle content (Section 1.1), and provide a mathematical motivation of
³⁶¹ the SM as a gauge theory (Section 1.2). We introduce the Higgs mechanism (Section
³⁶² 1.3), and outline two groups of theoretical extensions to the Standard Model that
³⁶³ feature extended Higgs sectors (Sections 1.4 and 1.5).

³⁶⁴ 1.1 History of the Standard Model

³⁶⁵ The building blocks of our modern-day understanding of particle physics were estab-
³⁶⁶ lished over the course of many decades by experimental discoveries and theoretical
³⁶⁷ advances, culminating in the development of a theoretical framework known as the
³⁶⁸ Standard Model (SM). In the 1880s, the electron was the first subatomic particle to
³⁶⁹ be identified, through measurements of particles produced by ionizing gas. By the
³⁷⁰ 1930s, atoms were known to consist mostly of empty space, with protons and neutrons
³⁷¹ concentrated at the center and orbited by electrons. Spurred by advances in parti-
³⁷² cle accelerator technology, the experimental discoveries of the positron, the muon,

and the pion, painted an increasingly complicated picture of particle physics that could not be described solely with atomic physics [1]. Quantum field theory (QFT) began to be developed in the early 20th century as an extension of the conceptual framework of quantum mechanics to electromagnetic fields [2]. In 1927, Dirac coined the name quantum electrodynamics (QED), which was the first part of QFT that was developed. QED quantized the electromagnetic field and supplied a relativistic theory of the electron, and could be applied to concrete physical processes such as the scattering of high-frequency photons by free electrons (Compton scattering), and the production of electron-positron pairs by photons [2]. In the 1940s the QED-only picture was challenged by the realization that the four-fermion theory of weak interactions had infinities at higher orders of perturbation theory which could not be removed via the technique of renormalization [3], i.e. shifting divergences into parts of the theory that do not influence empirical measurements [2].

In the 1950s and 1960s, QFT was extended to describe not only the electromagnetic force, but also the strong and weak force, with the final picture forming the Standard Model. This took place in the development and maturation of three principles: the quark model, the idea of gauge (or local) symmetry, and spontaneously broken symmetry [3]. In the fully fledged QFT, Lagrangians had to be formed that contained new classes of quantum fields, or particles [2].

The particle content of the Standard Model is summarized in Fig. 1.1. Particles are grouped into fermions, which comprise all known matter, and bosons, which mediate the interactions between particles. Fermions consist of quarks and leptons, and are grouped into three generations. For example, the electron belongs to the first generation of leptons. The second and third generation counterparts of the electron are the muon and the tau lepton, and are over 200 and 30,000 times heavier than the electron respectively. The quarks are also organized into three generations (top and bottom quarks, charm and strange quarks, and up and down quarks), and

400 carry fractional electric charge. Bosons are force carriers; the interaction of fermions
401 with bosons corresponds to fundamental forces. The Standard Model describes the
402 electromagnetic force, the strong nuclear force, and the weak nuclear force. Through
403 the strong force, quarks can form composite particles known as hadrons. Familiar
404 examples of hadrons are the protons and neutrons in the nucleus of an atom.

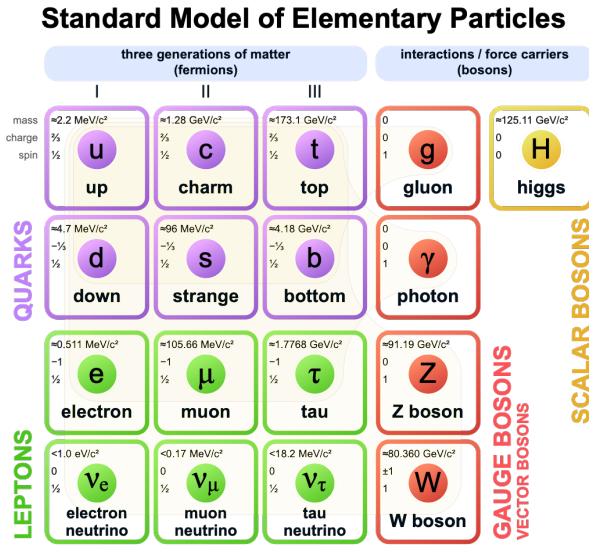


Figure 1.1: Table of Standard Model particles showing the grouping of the fermions into three generations of matter and the bosons, responsible for carrying the three fundamental forces in the Standard Model. The masses, charges, and spins of the particles are shown. The antimatter counterparts of the fermions are not shown. The possible interactions between the fermions and gauge bosons are highlighted.

1.2 The Standard Model as a gauge theory

406 In this section we lay the theoretical foundations of the Standard Model as a gauge
407 theory, starting from the principle of gauge invariance (gauge symmetry), with local
408 gauge symmetries giving rise to interactions between particles.

⁴⁰⁹ Gauge theories of elementary particle interactions originate from a freedom of
⁴¹⁰ choice in the mathematical description of particle fields which has no effect on the
⁴¹¹ particles' physical states [4]. The existence and form of the particles' interactions,

412 can be deduced from the existence of physically indeterminate, gaugable quantities.

413 An example of this gauge invariance is classical physics is the electromagnetic
414 interaction, where the fundamental field is the four-vector potential A^μ [4]. The
415 physical electromagnetic fields and Maxwell's equations arise from the elements of
416 the tensor $F_{\mu\nu}(x) = \partial_\mu A_\nu(x) - \partial_\nu A_\mu(x)$. Any two choices of A^μ that are related by a
417 transformation of the form

$$A_\mu \rightarrow A_\mu + \partial_\mu \alpha \quad (1.1)$$

418 for any real, differentiable function $\alpha(x)$, describe the same physical configuration,
419 and has no effect on Maxwell's equations. This "redundancy" in the choice of gauge
420 in Eqn. 1.1 is called a gauge symmetry.

421 One important consequence of gauge symmetry comes from the application of
422 Noether's theorem, which states that for every global transformation under which the
423 Lagrangian density is invariant, there exists a conserved quantity. If $\mathcal{L}(\Psi(x), \partial_\mu \Psi(x))$
424 is invariant under the transformation of the wave function $\Psi(x) \rightarrow \Psi'(x)$, where
425 $\Psi'(x) = \Psi(x) + \delta\Psi(x)$, then there exists a conserved current

$$\partial_\mu \left(\frac{\partial \mathcal{L}(x)}{\partial (\partial_\mu \Psi(x))} \delta\Psi(x) \right) = 0 \quad (1.2)$$

426 In classical mechanics, the conservation of linear momentum, angular momentum,
427 and energy follows from translational invariance, rotational variance, and invariance
428 under translations in time [4]. Likewise, charge conservation can be shown to arise
429 from the invariance of the Dirac Lagrangian density $\mathcal{L}_{\text{Dirac}} = \bar{\Psi}(i\gamma^\mu \partial_\mu - m)\Psi$ under the
430 particle wavefunction's phase transformation, $\Psi'(x) = \exp(i\epsilon\chi)\Psi(x)$. Thus Noether's
431 theorem establishes a correspondence between a gauge symmetry and a conserved
432 internal property (e.g. charge or momentum).

433 Interactions between particles arise if we modify the wave function with a phase

⁴³⁴ transformation $\Psi'(x) = \exp(ie\chi)\Psi(x)$, and allow the phase χ to be a function of
⁴³⁵ spacetime [4]. A wave function of the form

$$\Psi'(x) = \exp(ie\chi(x))\Psi(x) \quad (1.3)$$

⁴³⁶ can be verified to *not* be a solution to the Dirac equation for free particles: $(i\gamma^\mu\partial_\mu -$
⁴³⁷ $m)\Psi(x) = 0$. This necessitates a modified Dirac equation, where the derivative takes
⁴³⁸ into account that the vector field $V(x)$ needs to be compared at two displaced space-
⁴³⁹ time points in a curvilinear coordinate system:

$$\mathcal{D}_\mu \equiv \lim_{\Delta x^\mu \rightarrow 0} \frac{V_{||}(x + \Delta x) - V(x)}{\Delta x^\mu} \quad (1.4)$$

⁴⁴⁰ We define a covariant derivative,

$$D_\mu = \partial_\mu + ieA_\mu \quad (1.5)$$

⁴⁴¹ where $A_\mu(x)$ is a 4-vector potential. Thus the modified Dirac equation reads:

$$(i\gamma^\mu\mathcal{D}_\mu - m)\Psi(x) = 0 \quad (1.6)$$

⁴⁴² The simultaneous gauge transformation $A'_\mu(x) = A_\mu(x) - \partial_\mu\chi(x)$ and wavefunction
⁴⁴³ transformation $\Psi'(x) = \exp(ie\chi(x))\Psi(x)$ leaves the covariant-derivative form of the
⁴⁴⁴ Dirac equation (Eqn 1.1) invariant.

⁴⁴⁵ The generalization of this result is as follows: if a theory is invariant for unitary
⁴⁴⁶ transformations U of the particle states according to

$$\Psi' = U\Psi \quad (1.7)$$

447 One must define a derivative of the form

$$D^\mu = \partial^\mu + igB^\mu \quad (1.8)$$

448 to keep the theory invariant under Eqn. 1.7. The four-potential B^μ represents the
449 interacting four-potential which must be added to keep the theory invariant.

450 In the case of the Standard Model, the theory is built around the gauge trans-
451 formations $G = SU(3) \times SU(2) \times U(1)$. $SU(3)$ is associated to the strong force
452 (subscripted C); $SU(2)$ is associated to the weak force (subscripted L); and $U(1)$ is
453 hypercharge (subscripted Y). The gauge-covariant derivative is

$$\mathcal{D}_\mu = \partial_\mu - ig'B_\mu \frac{Y}{2} - igW_\mu^\alpha \frac{\tau_a}{2} - ig_s G_\mu^k \frac{\lambda_k}{2} \quad (1.9)$$

454 • In the $U(1)_Y$ term, B_μ is the weak hypercharge field.

455 • In the $SU(2)_L$ term, $W_\mu(x) = (W_\mu^1(x), W_\mu^2(x), W_\mu^3(x))$ are a triplet of four-
456 potentials. $\tau/2$ are the Pauli matrices, generators of the $SU(2)$ transformation.

457 • In the $SU(3)_C$ term, the gluon (color) field is G_μ . λ_k are the Gell-Man matrices,
458 generators of the $SU(3)$ transformation.

459 The invariance of the Standard Model under $SU(3)_C \times SU(2)_L \times U(1)_Y$ requires
460 massless fermions and massless force carriers.

461 1.3 The Higgs Mechanism

462 To introduce mass into the theory, i.e. to change the propagation of the gauge par-
463 ticles and all the fermions, the physical vacuum cannot have all the symmetries of
464 the Standard Model Lagrangian [4]. The symmetries of the physical vacuum must
465 be spontaneously broken, without affecting gauge invariance in the Lagrangian. The

466 Higgs mechanism proposes the existence of a scalar field, or fields, with nonzero vac-
467uum expectation values, which reduce the gauge symmetries of the physical vacuum
468 from $SU(3)_C \times SU(2)_L \times U(1)_Y$ down to $SU(3)_C \times U(1)_{EM}$.

469 The Higgs field interacts with the gauge bosons and fermions throughout space,
470 impeding their free propagation. The resulting broken symmetry correctly predicts
471 the mass ratio of the neutral (Z) and charged (W) massive electroweak bosons, and
472 predicts that at least one physical degree of freedom in the Higgs field is a particle
473 degree of freedom, called the Higgs boson. The location of the minimum of the Higgs
474 potential can be constrained from previously measured Standard Model parameters,
475 but the shape of the mass distribution of the Higgs boson must be experimentally
476 measured.

477 The minimal choice of Higgs field comes from the breaking of $SU(2)_L \times U(1)_Y$
478 down to $U(1)_{EM}$. The smallest $SU(2)$ multiplet is the doublet. The existence of three
479 massive electroweak bosons leads the Higgs sector to have at least three degrees of
480 freedom. The minimal single-doublet complex scalar Higgs field is

$$\Phi(x) = \begin{pmatrix} \phi^+(x) \\ \phi^0(x) \end{pmatrix} = \frac{1}{\sqrt{2}} \begin{pmatrix} \phi_1^+(x) + i\phi_2^+(x) \\ \phi_1^0(x) + i\phi_2^0(x) \end{pmatrix} \quad (1.10)$$

481 where ϕ_1^+ , ϕ_2^+ , ϕ_1^0 , and ϕ_2^0 are real (four degrees of freedom). By convention, the
482 nonzero vacuum expectation value is assigned to ϕ_1^0 .

483 The minimal self-interacting Higgs potential that is invariant under $SU(2)_L \times$
484 $U(1)_Y$ is given by

$$V(\Phi^\dagger \Phi) = -\mu^2 \Phi^\dagger \Phi + \lambda (\Phi^\dagger \Phi)^2, \quad \mu^2 > 0, \lambda > 0 \quad (1.11)$$

485 where λ is the coupling strength of the four-point Higgs interaction. The potential

486 energy is minimized at

$$\Phi_{\min} = \frac{1}{\sqrt{2}} \begin{pmatrix} 0 \\ v \end{pmatrix}, \text{ where } v = \sqrt{\mu^2/\lambda} \quad (1.12)$$

487 Choosing a fixed orientation of $\langle \Phi \rangle$ out of a continuous set of possible ground states
 488 spontaneously breaks the symmetry of the physical vacuum, as illustrated in Fig 1.2.

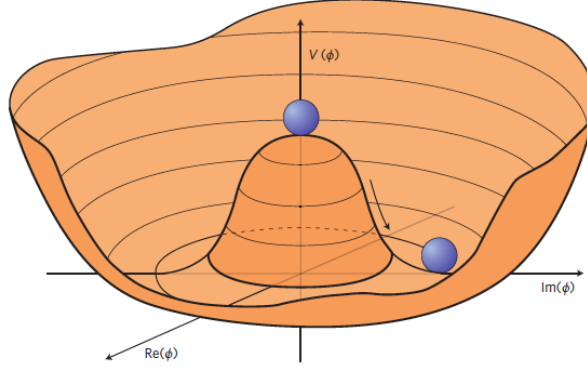


Figure 1.2: An illustration of the Higgs potential [5]. Choosing any of the points at the bottom of the potential breaks spontaneously the rotational $U(1)$ symmetry.

489 The excitations of the Higgs field with respect to the minimum Φ_{\min} are parame-
 490 terized by

$$\Phi(x) = \exp(i\xi(x) \cdot \tau) \frac{1}{\sqrt{2}} \begin{pmatrix} 0 \\ v + H(x) \end{pmatrix} \quad (1.13)$$

491 Three degrees of freedom are coupled directly to the electroweak gauge bosons; this
 492 is often referred to as the gauge bosons “eating” the Goldstone bosons to form the
 493 longitudinal polarizations of the massive spin-1 boson states. The $H(x)$ excitation is
 494 in the radial direction and corresponds to the free particle state of the Higgs boson.

495 1.4 Two-Higgs Doublet Models

496 One of the simplest possible extensions to the Standard Model is adding a doublet
 497 to the minimal Higgs sector of the Standard Model, which is a $SU(2)_L$ doublet H

498 with hypercharge $Y = +\frac{1}{2}$, denoted here as $H \sim 2_{+1/2}$. These extensions are found
499 in several theories such as supersymmetry. A general 2HDM can be extended with a
500 light scalar (2HDM+S) to obtain a rich set of exotic Higgs decays [6].

The charges of the Higgs fields are chosen to be $H_1 \sim 2_{-1/2}$ and $H_2 \sim 2_{+1/2}$, which acquire vacuum expectation values $v_{1,2}$ which are assumed to be real and aligned [6]. Expanding about the minima yields two complex and four real degrees of freedom:

$$H_1 = \frac{1}{\sqrt{2}} \begin{pmatrix} v_1 + H_{1,R}^0 + iH_{1,I}^0 \\ H_{1,R}^- + iH_{1,I}^- \end{pmatrix} \quad (1.14)$$

$$H_2 = \frac{1}{\sqrt{2}} \begin{pmatrix} H_{2,R}^+ + iH_{2,I}^+ \\ v_2 + H_{2,R}^0 + iH_{2,I}^0 \end{pmatrix} \quad (1.15)$$

501 The charged scalar and pseudoscalar mass matrices are diagonalized by a rotation
502 angle β , defined as $\tan \beta = v_2/v_1$. One charged (complex) field and one neutral
503 pseudoscalar combination of $H_{1,2,I}^0$ are eaten by the SM gauge bosons after electroweak
504 symmetry breaking [6]. The other complex field yields two charged mass eigenstates
505 H^\pm , which are assumed to be heavy. The remaining three degrees of freedom yield
506 one neutral pseudoscalar mass eigenstate

$$A = H_{1,I}^0 \sin \beta - H_{2,I}^0 \cos \beta \quad (1.16)$$

507 and two neutral scalar mass eigenstates (where $-\pi/2 \leq \alpha \leq \pi/2$)

$$\begin{pmatrix} h \\ H^0 \end{pmatrix} = \begin{pmatrix} -\sin \alpha & \cos \alpha \\ \cos \alpha & \sin \alpha \end{pmatrix} \begin{pmatrix} H_{1,R}^0 \\ H_{2,R}^0 \end{pmatrix} \quad (1.17)$$

508 We assume that the 2HDM is near or in the decoupling limit: $\alpha \rightarrow \pi/2 - \beta$, where
509 the lightest state in the 2HDM is h , which we identify as the 125 GeV Higgs particle
510 [6]. In this limit, the fermion couplings of h become identical to the Standard Model

511 Higgs, while the gauge boson couplings are very close to Standard Model-like for
 512 $\tan \beta \gtrsim 5$. All of the properties of h can be determined by just two parameters: $\tan \beta$
 513 and α , and the fermion couplings to the two Higgs doublets.

514 2HDM can be extended by a scalar singlet (2HDM+S) [6]:

$$S = \frac{1}{\sqrt{2}}(S_R + iS_I) \quad (1.18)$$

515 If this singlet only couples to the Higgs doublets $H_{1,2}$ and has no direct Yukawa
 516 couplings, all of its couplings to SM fermions result from mixing with $H_{1,2}$. Under
 517 these simple assumptions, exotic Higgs decays $h \rightarrow ss \rightarrow X\bar{X}Y\bar{Y}$ or $h \rightarrow aa \rightarrow$
 518 $X\bar{X}Y\bar{Y}$, and $h \rightarrow aZ \rightarrow X\bar{X}Y\bar{Y}$ are permitted, where $s(a)$ is a (pseudo)scalar mass
 519 eigenstate mostly composed of $S_R(S_I)$, and X, Y are Standard Model fermions or
 520 gauge bosons. There are two pseudoscalars in the 2HDM+S, and the mostly singlet-
 521 like pseudoscalar can be chosen to be the one lighter than the SM-like Higgs. For
 522 $m_a < m_h - m_Z \sim 35$ GeV, the exotic Higgs decay $h \rightarrow Za$ is possible, and for
 523 $m_a < m_h/2 \approx 63$ GeV, the exotic Higgs decay $h \rightarrow aa$ is possible.

524 In 2HDM, and by extension 2HDM+S, there are four types of fermion couplings
 525 commonly discussed in the literature that forbid flavor-changing neutral currents at
 526 tree level [6]. These are referred to as Type I (all fermions couple to H_2), Type II
 527 (MSSM-like, d_R and e_R couple to H_1 , u_R to H_2), Type III (lepton-specific, leptons
 528 and quarks couple to H_1 and H_2 respectively) and Type IV (flipped, with u_R , e_R
 529 coupling to H_2 and d_R to H_1). The exact branching ratios of the pseudoscalars to
 530 Standard Model particles vary depending on the 2HDM+S model and the value of
 531 $\tan \beta$ (e.g. Fig. 1.3).

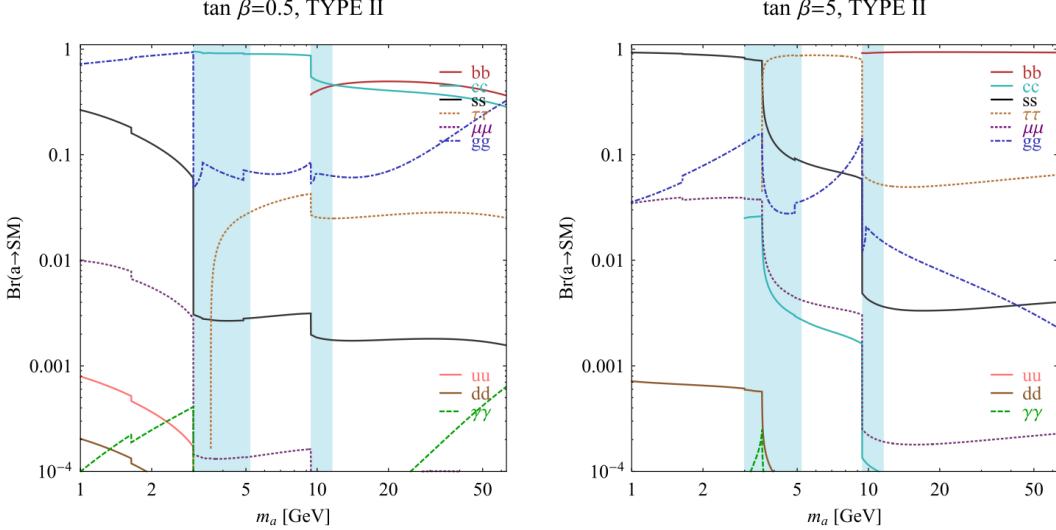


FIG. 7 (color online). Branching ratios of a singletlike pseudoscalar in the 2HDM + S for type-II Yukawa couplings. Decays to quarkonia likely invalidate our simple calculations in the shaded regions.

Figure 1.3: Branching ratios of a singlet-like pseudoscalar in Type II 2HDM+S for $\tan\beta = 0.5$ (left) and $\tan\beta = 5$ (right) from [6], showing the dependence of the branching ratios on $\tan\beta$, as well as the prominence of the branching ratios to bb and $\tau\tau$, the channels searched for in the analysis presented here.

1.5 Two Real Singlet Model

The two real singlet model (TRSM) adds two real singlet degrees of freedom to the Standard Model. These are written as two real singlet fields S and X . Depending on the vacuum expectation values acquired by the scalars, different phases of the model can be realized [7]. To reduce the number of free parameters, two discrete \mathbb{Z}_2 symmetries are introduced. The fields are decomposed as

$$\Phi = \begin{pmatrix} 0 \\ \frac{\phi_h + v}{\sqrt{2}} \end{pmatrix}, S = \frac{\phi_S + v_S}{\sqrt{2}}, X = \frac{\phi_X + v_X}{\sqrt{2}} \quad (1.19)$$

To achieve electroweak-breaking symmetry, $v = v_{SM} \sim 246$ GeV is necessary. If the vacuum expectation values $v_S, v_X \neq 0$ the \mathbb{Z}_2 are spontaneously broken, and the fields $\phi_{h,S,X}$ mix into three physical scalar states. This is called the broken phase and leads to the most interesting collider phenomenology.

542 The mass eigenstates $h_{1,2,3}$ are related to the fields $\phi_{h,S,X}$ through a 3×3 orthogonal
543 mixing matrix denoted R . The mass eigenstates are assumed to be ordered $M_1 \leq$
544 $M_2 \leq M_3$. R is parameterized by the three mixing angles θ_{hS} , θ_{hX} , θ_{SX} . The nine
545 parameters of the scalar potential can be expressed in terms of the three physical
546 Higgs masses, the three mixing angles, and the three vacuum expectation values.

547 After fixing one of the Higgs masses to the mass of the observed Higgs boson, and
548 fixing the Higgs doublet vacuum expectation value to its Standard Model value, there
549 are seven remaining free parameters of the TRSM [7].

550 In one benchmark scenario of TRSM [7], the heaviest scalar state h_3 is identified
551 with the 125 GeV Higgs, h_{125} , and it can decay asymmetrically $h_{125} \rightarrow h_1 h_2$, which
552 we also denote $h \rightarrow a_1 a_2$ to highlight the similarity with the symmetric decay $h \rightarrow aa$
553 typically interpreted in 2HDM+S as discussed. The parameter values in TRSM are
554 chosen such that the coupling of h_3 to Standard Model particles are nearly identical
555 to the Standard Model predictions.

556 In benchmark scenario 1 (benchmark plane 1, or BP1) (Fig. 1.4) [7], the maximal
557 branching ratios for $h_3 \rightarrow h_1 h_2$ reach up to 7 – 8% which translates into a signal
558 rate of around 3 pb. These maximal branching ratios are reached in the intermediate
559 mass state for h_2 , $M_2 \sim 60 – 80$ GeV. For $M_2 < 40$ GeV, although phase space opens
560 up significantly for light decay products, the branching ratio becomes smaller.

561 If the decay channel $h_2 \rightarrow h_1 h_1$ is kinematically open (i.e. $M_2 > 2M_1$), it is the
562 dominant decay mode leading to a significant rate for the $h_1 h_1 h_1$ final state, in a
563 “cascade” decay. In BP1, $BR(h_2 \rightarrow h_1 h_1) \simeq 100\%$ above the red line in Fig. 1.4. If,
564 in addition, $M_1 \gtrsim 10$ GeV, the h_1 decays dominantly to $b\bar{b}$ leading to a sizable rate
565 for the $b\bar{b}b\bar{b}b\bar{b}$ final state as shown in Fig. 1.4 (*bottom right*).

566 If the $h_2 \rightarrow h_1 h_1$ decay is kinematically closed (i.e. $M_2 < 2M_1$), both scalars decay
567 directly to Standard Model particles, with branching ratios identical to a Standard
568 Model-like Higgs boson, i.e. with the $b\bar{b}b\bar{b}$ final state dominating, as shown in Fig. 1.4

⁵⁶⁹ (*bottom left*), while at smaller masses, combinations with τ leptons and eventually
⁵⁷⁰ final states with charm quarks and muons become relevant [7].

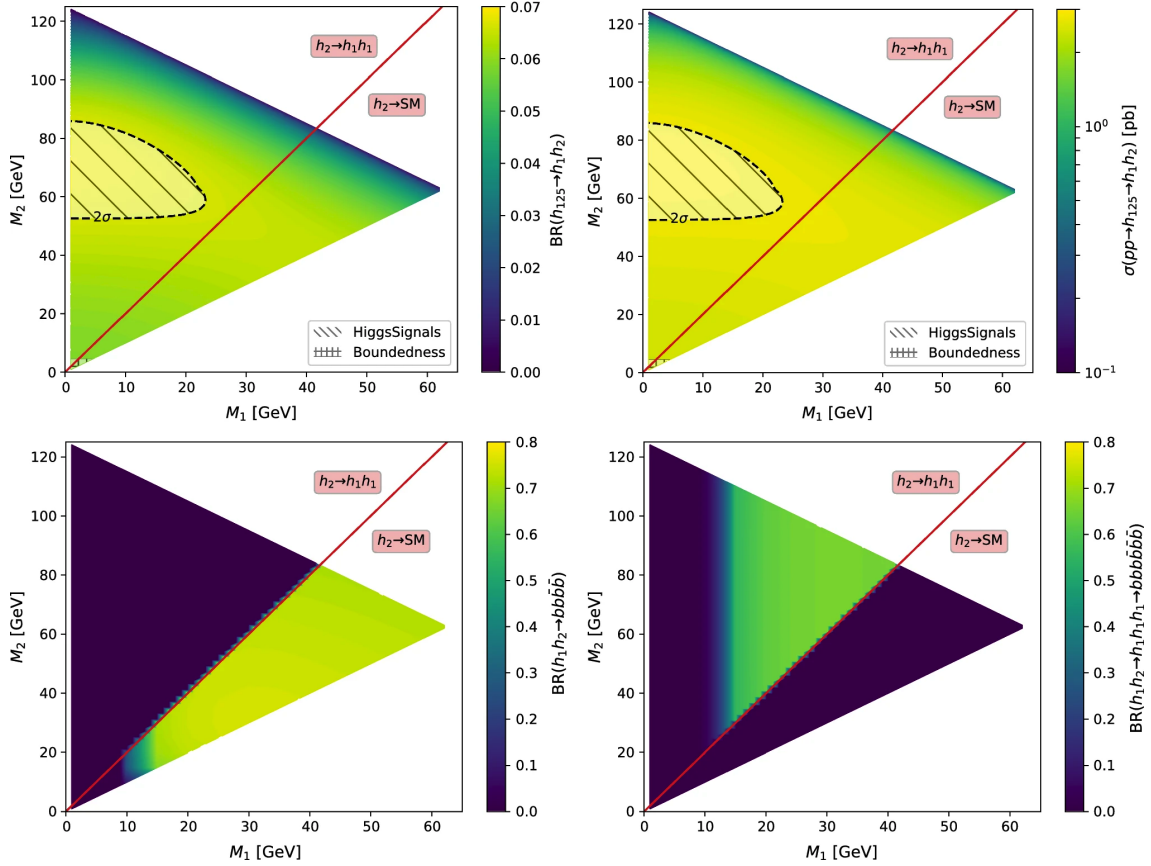


Figure 1.4: Benchmark plane BP1 for benchmark scenario 1 from [7], for the decay signature $h_{125} \rightarrow h_1 h_2$ with $h_{125} \equiv h_3$, defined in the (M_1, M_2) plane. The color code shows $\text{BR}(h_3 \rightarrow h_1 h_2)$ (*top left*) and the 13 TeV LHC signal rate for $pp \rightarrow h_3 \rightarrow h_1 h_2$ (*top right*). The red line separates the region $M_2 > 2M_1$, where $\text{BR}(h_2 \rightarrow h_1 h_1) \sim 100\%$, from the region $M_2 < 2M_1$, where $\text{BR}(h_2 \rightarrow F_{SM}) \sim 100\%$. The *bottom left* and *right* show the branching ratio of the $h_1 h_2$ into (respectively) $b\bar{b}b\bar{b}$, and through a $h_2 \rightarrow h_1 h_1$ cascade to $b\bar{b}b\bar{b}b\bar{b}$. The hatched region indicates where the decay rate slightly exceeds the 2σ upper limit inferred from the LHC Higgs rate measurements, though the region depends on the parameter choices and experimental searches should cover the whole mass range.

⁵⁷¹ **Chapter 2**

⁵⁷² **The Large Hadron Collider and the**
⁵⁷³ **CMS Experiment**

⁵⁷⁴ This chapter introduces the key aspects of the CERN Large Hadron Collider (LHC)
⁵⁷⁵ and the Compact Muon Solenoid (CMS) experiment where the work for this thesis was
⁵⁷⁶ conducted. Section 2.1 describes the history of accelerator developments at CERN
⁵⁷⁷ that led to the construction of the LHC, the current LHC configuration, and the
⁵⁷⁸ largest experiments located at the LHC. The concepts of beam luminosity and pileup,
⁵⁷⁹ which are critical for understanding and measuring high-energy particle collisions,
⁵⁸⁰ are described in Section 2.2 and discussed in the context of the High-Luminosity
⁵⁸¹ LHC (HL-LHC) upgrade in Section 2.3. Lastly, Section 2.4 describes the design
⁵⁸² and function of CMS and its subdetectors, and terminates in a description of data
⁵⁸³ processing at CMS, beginning from online event filtering in the Level-1 Trigger, to
⁵⁸⁴ processing in the High-Level Trigger, to offline particle reconstruction, and finally
⁵⁸⁵ long-term storage and processing of measured events.

586 2.1 The Large Hadron Collider

587 CERN, the European Organization for Nuclear Research, is an international organiza-
588 tion based in Meyrin, Switzerland which operates the world's largest particle physics
589 laboratory, and is the site of the Large Hadron Collider (LHC) [8]. The very first
590 accelerator built at CERN was the 600 MeV Synchrocyclotron (SC), which initially
591 provided beams for CERN's first experiments. The newer and more powerful Proton
592 Synchrotron (PS), which could accelerate particles to an energy of 28 GeV, began op-
593 erations in 1959 and is still in use today. The first hadron collider at CERN was the
594 Intersecting Storage Rings (ISR), which consisted of two interlaced rings each with a
595 diameter of 200. The ISR collided protons at a center-of-mass energy of 62 GeV and
596 began measuring collisions in 1971. In 1968 CERN began to accelerate heavy ions
597 in the Super Proton Synchrotron (SPS), which is 7 kilometers in circumference and
598 was the first of CERN's giant underground rings to be built. The SPS became the
599 forefront of CERN's particle physics program in 1976, and in 1981 was converted into
600 a proton-antiproton collider. The final and largest underground ring constructed at
601 CERN was the Large Electron-Positron (LEP) collider, which was commissioned in
602 July 1989 and hosted 5176 magnets and 128 accelerating cavities located around a
603 27-kilometer circumference. Over 11 years of research, four detectors, ALEPH, DEL-
604 PHI, L3, and OPAL measured the collisions, with collision energies reaching up to
605 209 GeV in the year 2000. In November 2000, LEP was closed down to make way for
606 the construction of the LHC in the same tunnel.

607 In its current configuration, the LHC accelerator complex at CERN is a suc-
608 cession of machines that accelerate particles in stages until they reach their final energy
609 of 6.5 TeV per beam [9] [10]. In Linear accelerator 4 (Linac4), negative hydrogen
610 ions (hydrogen atoms with an additional electron) are accelerated to 160 MeV, and
611 stripped of their two electrons, leaving only protons, before entering the Proton Syn-
612 chrotron Booster (PSB). These protons are accelerated to 2 GeV, then to 26 GeV in

613 the Proton Synchrotron (PS), and 450 GeV in the Super Proton Synchrotron (SPS).
614 The protons are transferred to the two beam pipes of the Large Hadron Collider
615 (LHC). The LHC is a 27-kilometer ring of superconducting magnets, inside which
616 one beam circulates clockwise and the other counterclockwise. Each LHC ring takes
617 4 minutes and 20 seconds to fill, and it takes about 20 minutes for the protons to
618 reach their maximum energy. During normal operating conditions, beams circulate
619 for many hours inside the LHC ring.

620 The beams of particles in the LHC are made to collide at a center-of-mass energy
621 of up to 14 TeV, at four positions at particle detector experiments located around
622 the ring: ATLAS, CMS, ALICE, and LHCb. An aerial view of the four major
623 experiments' locations is shown in Fig. 2.1 [11]. ATLAS and CMS are the two
624 general-purpose detectors with broad physics programmes spanning Standard Model
625 measurements and searches for signatures of new physics [12] [13]. The two experi-
626 ments use different technical solutions and different magnet system designs. ALICE
627 is a general-purpose detector dedicated to measuring LHC heavy-ion collisions, and
628 is designed to address the physics of strongly interacting matter, and the properties
629 of quark-gluon plasma [14]. The LHCb experiment specializes in investigating CP vi-
630 olation through measuring the differences in matter and antimatter, by using a series
631 of subdetectors to detect mainly forward particles close to the beam direction [15].

632 **2.2 Luminosity and pileup**

633 In order to search for rare processes, such as those resulting from a Higgs, W, or Z
634 boson, a large number of parton interactions per second are required at the LHC.
635 The number of events generated per second by the LHC collisions is given by

$$N_{event} = \mathcal{L} \cdot \sigma_{event} \quad (2.1)$$

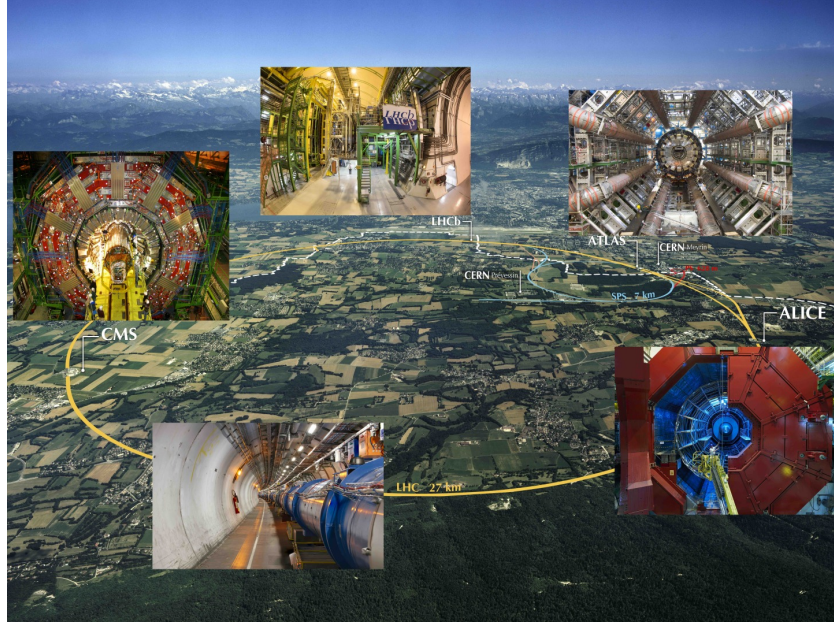


Figure 2.1: Aerial view of the Large Hadron Collider (LHC) spanning the border of France and Switzerland, and the four major experiments located around the ring: CMS (Compact Muon Solenoid), LHCb (LHC beauty), ATLAS (A Toroidal LHC Apparatus), and ALICE (A Large Ion Collider Experiment) [11].

636 where σ_{event} is the cross-section for the event under study, and \mathcal{L} the instantaneous
 637 luminosity. The instantaneous luminosity is measured in units of $\text{cm}^{-2} \text{ s}^{-1}$, and
 638 depends only on the beam parameters, and can be written for a Gaussian beam
 639 distribution as:

$$\mathcal{L} = \frac{N_b^2 n_b f_{rev} \gamma_r}{4\pi \epsilon_n \beta^*} F \quad (2.2)$$

640 where the parameters are as defined, along with some example typical nominal values
 641 in Phase-1 of the LHC [16] [17]:

- 642 • N_b is the number of particles per bunch ($N_b \approx 1.15 \times 10^{11}$ protons per bunch)
 643 • n_b is the number of bunches per beam (maximum 2808),
 644 • f_{rev} is the revolution frequency ($\approx 11 \text{ kHz}$),
 645 • γ_r is the relativistic gamma factor,

- ϵ_n is the normalized transverse beam emittance (area in a transverse plane occupied by the beam particles),
- β^* is the beta function at the collision point ($\beta^* = 0.55$ m),
- and F is the geometric luminosity reduction factor due to the crossing angle at the interaction points ($F \approx 0.84$ for Phase-1. Note that complete overlap would give $F = 1$).

Peak luminosity at interaction points 1 and 5 reach values of $\sim 1.0 \times 10^{34} \text{ cm}^{-2} \text{ s}^{-1}$, with peak luminosity per bunch crossing reaching $\sim 3.56 \times 10^{34} \text{ cm}^{-2} \text{ s}^{-1}$.

Per Eqn. 2.1, the integrated luminosity over time is proportional to the number of events produced, and the size of LHC datasets is commonly presented in terms of integrated luminosity. Collider operation aims to optimize the integrated luminosity. Thus the exploration of rare events in the LHC collisions requires both high beam energies and high beam intensities.

The LHC’s nominal beam luminosities are sufficiently large for multiple proton-proton collisions to occur in the same time window of 25 nanoseconds in which proton bunches collide [18]. These multiple collisions will lead to particle interactions overlapping in the detector. To measure a proton-proton collision, the single collision must be separated from overlapping collisions, which are called “pileup” collisions. A distribution of pileup in the data-taking years 2016-2018 is shown in Fig. 2.2. The pileup is defined as the average number of pp collisions per bunch crossing.

CMS reports an inelastic pp cross section of $\sigma_{\text{inel}} = 68.6$ millibarns at a center-of-mass energy of $\sqrt{s} = 13 \text{ TeV}$ [19], which can be used to estimate pileup as follows:

$$\text{Pileup} = \frac{\mathcal{L} \times \sigma_{\text{inel}}}{n_b \cdot f} \quad (2.3)$$

With the example values above, pileup can be estimated to be ~ 22 .

669 While useful in the search for rare physics processes, higher luminosities create
 670 more intense pileup conditions, posing a greater challenge to detector performance
 671 and particle reconstruction and identification.

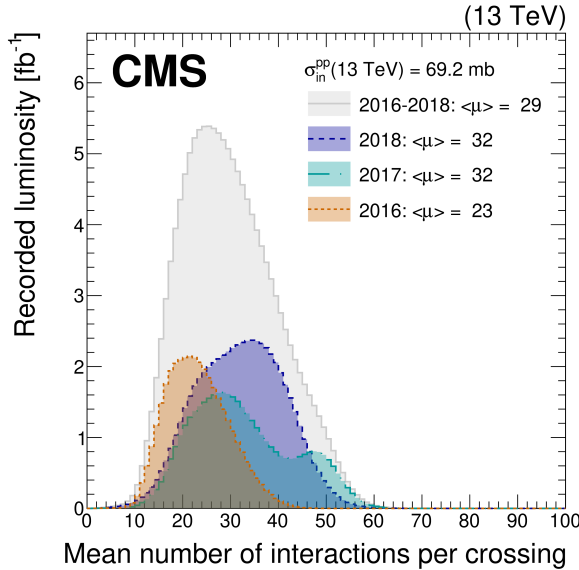


Figure 2.2: Distribution of the mean number of inelastic collisions per bunch crossing (pileup) in data [18], for proton-proton collisions in 2016 (*dotted orange*), 2017 (*dotted light blue*), 2018 (*dotted dark blue*), and integrated over 2016-2018 (*solid grey*). A cross-section of inelastic proton-proton collisions of 69.2 mbarns is assumed. In the running conditions of the High-Luminosity LHC, pileup will reach unprecedented levels of up to 200 per bunch crossing [20].

672 2.3 The High-Luminosity LHC

673 The High-Luminosity LHC (HL-LHC) is a major upgrade of the LHC scheduled
 674 to take place in the late 2020s, that will increase the instantaneous luminosity by
 675 a factor of five beyond the original design value, and the integrated luminosity
 676 by a factor of ten [20]. This will be accomplished through accelerator technological
 677 advances: for instance, reduction of the interaction point β^* from 0.55 m down to 0.15
 678 m by installation of new final-focusing magnets, and improvements in the geometric
 679 luminosity loss factor $F \approx 1$ through the installation of crab cavities that optimize

680 the orientation of colliding bunches. A further discussion of the HL-LHC upgrades
681 for the CMS detector follows in Chapter 3.

682 **2.4 The CMS Detector**

683 The Compact Muon Solenoid (CMS) experiment was conceived to study proton-
684 proton and lead-lead collisions at a center-of-mass energy of 14 TeV (5.5 TeV nucleon-
685 nucleon) and at luminosities up to $10^{34} \text{ cm}^{-2} \text{ s}^{-1}$ ($10^{27} \text{ cm}^{-2} \text{ s}^{-1}$) [21] [22]. Starting
686 from the beam interaction region at the center of the CMS detector, particles first
687 pass through a silicon pixel and strip tracker, in which charged-particle trajectories
688 (tracks) and origins (vertices) are reconstructed from signals (hits) in the sensitive
689 layers. The tracker is immersed in a high-magnetic-field superconducting solenoid
690 that bends the trajectories of charged particles, allowing the measurement of their
691 electric charge and momenta. Electrons and photons are then absorbed in an electro-
692 magnetic calorimeter (ECAL) comprised of lead-tungstate scintillating-crystals. The
693 corresponding electromagnetic showers are detected as clusters of energy recording in
694 neighboring cells, from which the direction and energy of the particles can be deter-
695 mined. Charged and neutral hadrons may initiate a hadronic shower in the ECAL
696 as well, which is then fully absorbed in the hadron calorimeter (HCAL). The result-
697 ing clusters are used to estimate their direction and energies. Muons and neutrinos
698 pass through the calorimeters with little to no interactions. Neutrinos escaped un-
699 detected; muons produce hits in additional gas-ionization chamber muon detectors
700 housed in the iron yoke of the flux-return. A sketch of example particle interactions
701 in a transverse slice of the CMS detector is shown in Fig. 2.3. The collision data is
702 recorded with the use of the Level-1 (L1) trigger (discussed in greater detail in 2.5.5),
703 the High-Level Trigger (HLT), and data acquisition systems ensuring high efficiency
704 in selecting physics events of interest.

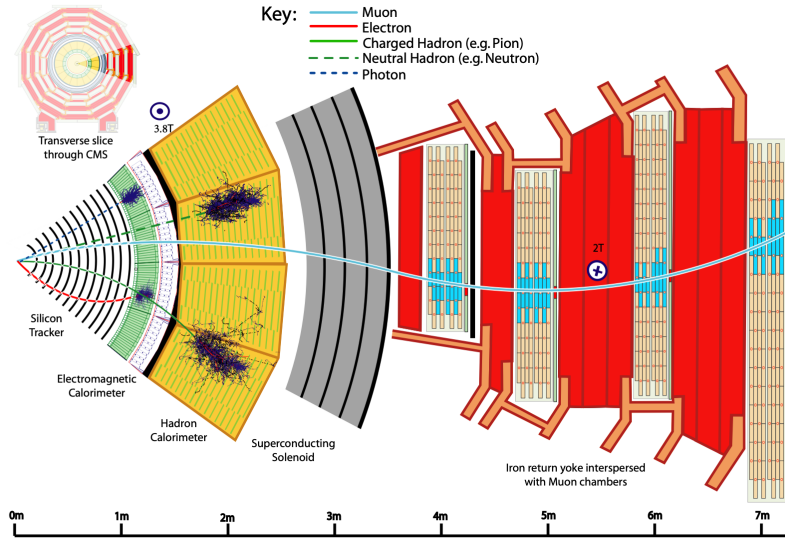


Figure 2.3: Sketch of particle trajectories of muons, electrons, charged and neutral hadrons, and photons in a transverse cross-section of the CMS detector [22].

705 CMS uses a right-handed coordinate system [21]. The origin is centered at the
 706 nominal collision point inside the experiment. The x axis points towards the center
 707 of the LHC, and the y axis points vertically upwards. The z axis points along the
 708 beam direction. The azimuthal angle, ϕ , is measured from the x axis in the x - y
 709 plane, and the radial coordinate in this plane is denoted by r . The polar angle, θ ,
 710 is measured from the z axis. The pseudorapidity, η , is defined as $\eta = -\ln \tan(\theta/2)$.
 711 The momentum and energy transverse to the beam direction, denoted by p_T and E_T
 712 respectively, are computed from the x and y components. The momentum imbalance
 713 in the transverse plane is called the missing transverse momentum, and its magnitude
 714 is denoted by E_T^{miss} .

715 2.5 Sub-detectors of CMS

716 This section details the sub-detectors of CMS that operate to identify and precisely
 717 measure muons, electrons, photons, and jets over a large energy range.

718 **2.5.1 Inner tracking system**

719 The CMS Tracker performs robust tracking and detailed vertex reconstruction in the
720 4 T magnetic field of the superconducting solenoidal magnet. The primary sensors
721 used in the tracker are p^+ on n -bulk devices, which allow high voltage operation and
722 are radiation-resistant [23] [24]. The active envelope of the CMS Tracker extends to a
723 radius of 115 cm, over a length of approximately 270 cm on each side of the interaction
724 point [23]. Charged particles in the region $|\eta| \lesssim 1.6$ benefit from the full momentum
725 measurement precision. In this region, a charged particle with p_T of 1000 GeV has a
726 sagitta of $\sim 195 \mu\text{m}$. The Tracker acceptance extends further to $|\eta| = 2.5$, with a
727 reduced radius of approximately 50 cm.

728 The high magnetic field of CMS causes low p_T charged particles to travel in helical
729 trajectories with small radii. The majority of events contain particles with a steeply
730 falling p_T spectrum, resulting in a track density which rapidly decreases at higher
731 radii.

732 A schematic view of the current Phase-1 CMS tracker [25], including the pixel
733 detector, is shown in Fig. 2.4. The Phase-1 pixel detector consists of three barrel
734 layers (BPIX) at radii of 4.4 cm, 7.3 cm, and 10.2 cm, and two forward/backward disks
735 (FPIX) at longitudinal positions of ± 34.5 cm and ± 46.5 cm, and extending in radius
736 from about 6 cm to 15 cm. These pixelated detectors produce 3D measurements along
737 the paths of charged particles with single hit resolutions between 10-20 μm .

738 After the pixel and on their way out of the tracker, particles pass through the
739 silicon strip tracker which reaches out to a radius of 130 cm (Fig. 2.4). The sensor
740 elements in the strip tracker are single-sided p -on- n type silicon micro-strip sensors
741 [21]. The silicon strip detector consists of four inner barrel (TIB) layers assembled
742 in shells, with two inner endcaps (TID), each composed of three small discs. The
743 outer barrel (TOB) consists of six concentric layers. Two endcaps (TEC) close off
744 the tracker on either end.

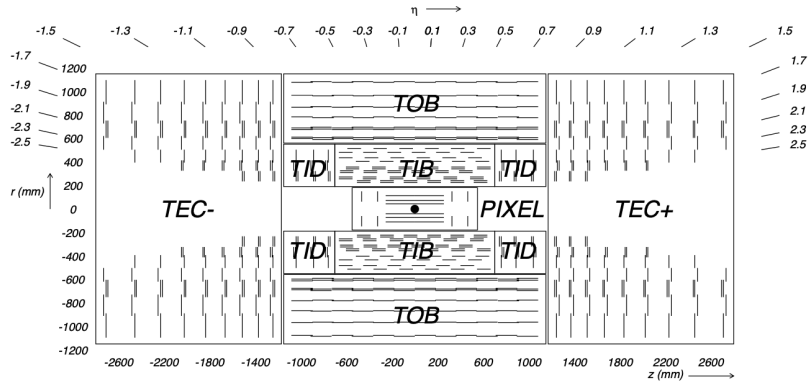


Figure 2.4: Cross section of the current Phase-1 CMS tracker [25]. Each line represents a detector module. Double lines indicate back-to-back modules which deliver two-dimensional (stereo) hits in the strip tracker.

2.5.2 ECAL

The electromagnetic calorimeter (ECAL) of CMS measures electromagnetic energy deposits with high granularity. One of the driving criteria in the design was the capability of detecting the Standard Model Higgs boson decay to two photons (in fact, the channel in which the 125 GeV Higgs boson was discovered at CMS). ECAL is a hermetic homogeneous calorimeter comprised of 61,200 lead tungstate (PbWO_4) crystals mounted in the central barrel, with 7,324 crystals in each of the two endcaps [21]. A preshower detector is located in front of the endcap crystals. Avalanche photodiodes (APDs) are used as photodetectors in the barrel and vacuum phototriodes (VPTs) in the endcaps.

The design of the ECAL is driven by the behaviour of high-energy electrons, which predominantly lose energy in matter via bremsstrahlung, and high-energy photons by e^+e^- pair production. The characteristic amount of matter traversed for these interactions is the radiation length X^0 , usually measured in units of g cm^{-2} . The radiation length is also the mean distance over which a high-energy electron loses all but $1/e$ of its energy via bremsstrahlung [26]. Thus high granularity in η and ϕ , and the length of the ECAL crystals, is designed to capture the shower of e/γ produced

762 by electrons and photons.

763 The barrel part of the ECAL (EB) covers the pseudorapidity range $|\eta| < 1.479$
764 [21]. The barrel granularity is 360-fold in ϕ and (2×85) -fold in η . The crystal cross-
765 section corresponds to approximately 0.0174×0.0174 in $\eta - \phi$ or 22×22 mm 2 at the
766 front face of the crystal, and 26×26 mm 2 at the rear face. The crystal length is 230
767 mm, corresponding to $25.8 X_0$.

768 The ECAL read-out acquires the signals of the photodetectors [21]. At each bunch
769 crossing, digital sums representing the energy deposit in a trigger tower, comprising
770 5×5 crystals in $\eta \times \phi$, are generated and sent to the Level-1 trigger system (detailed
771 in Section 2.5.5).

772 2.5.3 HCAL

773 The hadronic calorimeter (HCAL) of CMS measures hadronic energy, which is key to
774 characterizing the presence of apparent missing transverse energy which could arise
775 from hadron jets and neutrinos or exotic particles [21]. A schematic of the components
776 of HCAL are shown in Fig. 2.5. The HCAL barrel (HB) and endcaps (HE) are located
777 outside of the tracker and the ECAL, spanning a radius of 1.77 m (outer extent of
778 ECAL) up to 2.95 m (inner extent of the magnet coil). An outer hadron calorimeter
779 (HO) is placed outside the solenoid to complement the barrel calorimeter. Beyond
780 $|\eta| = 3$, the forward hadron calorimeter (HF) at 11.2 m from the interaction point
781 extend the pseudorapidity coverage to $|\eta| = 5.2$.

782 The HB is a sampling calorimeter covering the pseudorapidity range $|\eta| < 1.3$ [21].
783 It consists of 36 identical azimuthal wedges which form two half-barrels (HB+ and HB-
784), with a segmentation of $(\Delta\eta, \Delta\phi) = (0.087, 0.087)$. The HE covers pseudorapidity
785 $1.3 < |\eta| < 3$. The HB and endcap HE calorimeters are sampling calorimeters which
786 use brass as the absorber and plastic scintillator as the active material. Light from
787 the plastic scintillator is wavelength-shifted and captured in optic fibers which are

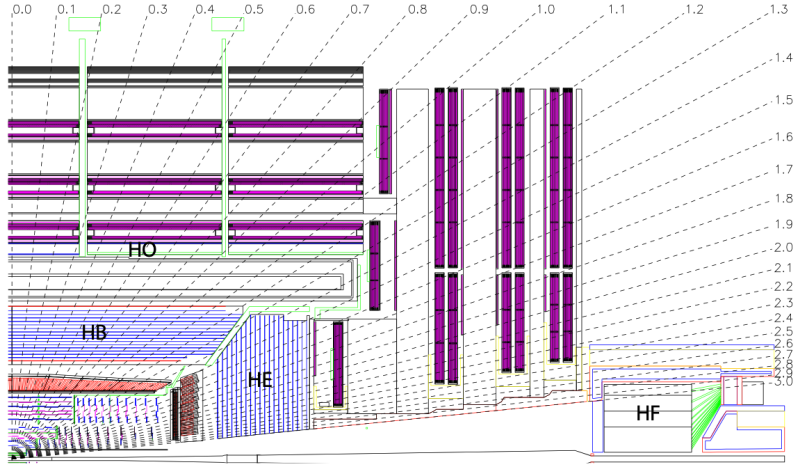


Figure 2.5: Longitudinal view of the CMS detector showing the hadron calorimeter barrel (HB), endcap (HE), outer (HO), and forward (HF) calorimeters from [21].

788 read out by front-end electronics [27].

789 In the central pseudorapidity region, the combined stopping power of EB plus the
 790 HB is insufficient to contain hadron showers [21]. To ensure adequate sampling depth,
 791 the hadron calorimeter is extended with a tail catcher, the HO. The size and position
 792 of the tiles are designed to roughly map the layers of the HB to make towers with
 793 the same granularity of 0.087×0.087 in η and ϕ . HO uses the same active material
 794 as the HB and HE calorimeters, but uses the steel return yoke and magnet material
 795 of CMS as absorbers [27].

796 The HF is a Cherenkov calorimeter based on a steel absorber and quartz fibers
 797 which run longitudinally through the absorber and collect Cherenkov light, primarily
 798 from the electromagnetic component of showers developed in the calorimeter [27].
 799 Photomultiplier tubes are used to collect light from the quartz fibers. The HF is
 800 designed to survive in the harsh radiation conditions and high particle flux of the
 801 forward region. On average, 760 GeV per proton-proton interaction is deposited into
 802 the two forward calorimeters, compared to only 100 GeV for the rest of the detector
 803 [21]. Furthermore, this energy has a pronounced maximum at the highest rapidities.

804 **2.5.4 Muon detectors**

805 The CMS muon system is designed to have the capability of reconstructing the mo-
806 mentum and charge of muons over the kinematic range of the LHC, since muons are a
807 powerful handle on signatures of interesting processes over the high background rate
808 of the LHC [21]. For instance, the decay of the Standard Model Higgs boson into
809 ZZ , which in turn decay to 4 leptons, can be reconstructed with high 4-particle mass
810 resolution if all the leptons are muons, since muons are less affected than electrons
811 by radiative losses in the tracker material.

812 The muon system consists of a cylindrical barrel section and two planar endcap
813 regions [21]. The barrel muon detector consists of drift tube (DT) chambers covering
814 the pseudorapidity region $|\eta| < 1.2$ (Fig. 2.6). The DTs can be used as tracking
815 detectors due to the barrel region's characteristic low neutron-induced backgrounds,
816 low muon rate, and relatively uniform 4T magnetic field contained in the steel yoke.

817 In the two endcap regions, the muon rates and background levels are high and the
818 magnetic field is large and non-uniform [21]. Here, the muon system uses cathode
819 strip chambers (CSCs) to identify muons between $0.9 < |\eta| < 2.4$. The cathode strips
820 of each chamber run radially outwards and provide a precision measurement in the
821 $r - \phi$ bending plane. The anode wires run approximately perpendicular to the strips
822 and are read out in order to measure η and the beam-crossing time of a muon.

823 In addition to the DT and CSC, a dedicated trigger system consisting of resistive
824 plate chambers (RPCs) in the barrel and endcap regions provide a fast, independent,
825 and highly-segmented trigger with a sharp p_T threshold over a large portion of the
826 pseudorapidity range ($|\eta| < 1.6$) of the muon system [21]. RPCs have good time
827 resolution but coarser position resolution compared to the DTs or CSCs. The RPCs
828 also play a role in resolving ambiguities in reconstructing tracks from multiple hits in
829 a chamber.

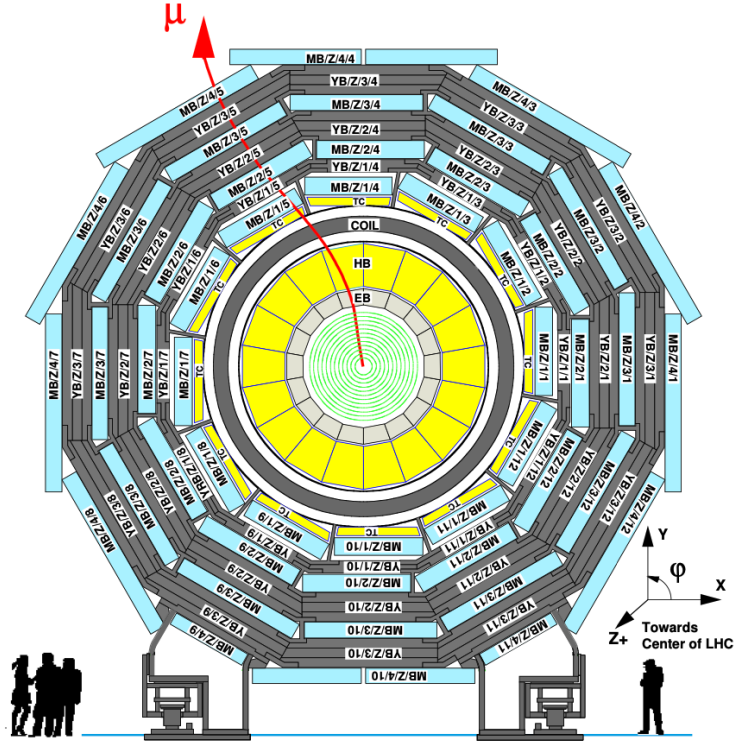


Figure 2.6: Layout of the CMS barrel muon drift tube (DT) chambers in one of the five wheels from [21]. The DTs are organized in 12 sectors of the yoke barrel (YB). In each of the 12 sectors of the yoke, there are 4 muon chambers per wheel (MB1, MB2, MB3, and MB4).

2.5.5 The Level-1 Trigger

The design performance of the LHC corresponds to an instantaneous luminosity of $10^{34} \text{ cm}^{-2} \text{ s}^{-1}$ with a 25 ns bunch crossing rate, giving an average pile-up (number of simultaneous events) of 25 per bunch crossing [28]. The large number of minimum bias events per bunch crossing, combined with the small cross-sections of possible physics discovery signatures, necessitates a sophisticated event selection system for filtering this large event rate, as it is impossible to save all events. This data filtering system is implemented by CMS in two stages. The first stage is the Level-1 (L1) Trigger, which is deployed in custom electronic hardware systems and is responsible for reducing the event rate to around 100 kHz. The second stage is the High-Level

840 Trigger (HLT) which is described in Section 2.5.6. This section describes the Phase-1
 841 configuration of the Level-1 Trigger.

842 The L1 Trigger data flow of Phase-1 is shown in Fig. 2.7 [28], with organization
 843 into the L1 calorimeter trigger, the L1 muon trigger, and the L1 global trigger.

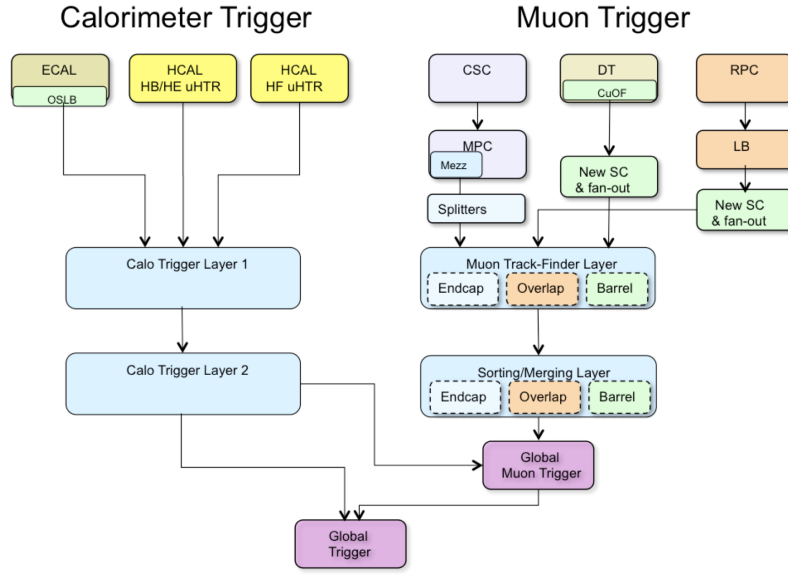


Figure 2.7: Dataflow for the Phase-1 Level-1 Trigger [28], which is implemented in custom hardware and is responsible for reducing the event rate from the LHC bunch crossing frequency of 400 MHz (bunch crossings every 25 ns) to a maximum rate of 100 kHz. In Phase-1, the Level-1 Trigger has access to information from the calorimeter and muon detectors.

844 The L1 calorimeter trigger begins with trigger tower energy sums formed by the
 845 ECAL, HCAL, and HF Trigger Primitive Generator (TPG) circuits from the indi-
 846 vidual calorimeter cell energies. In the original configuration, the ECAL energies
 847 were accompanied by a bit indicating the transverse extent of the electromagnetic
 848 energy deposits, and the HCAL energies were accompanied by a bit indicating the
 849 presence of minimum ionizing energy [29]. Between Long Shutdowns 1 and 2 (LS1
 850 and LS2), HF was upgraded to provide finer granularity information to the trigger,
 851 and the HCAL barrel and endcap front-end electronics were upgraded to provide
 852 high-precision timing information and depth segmentation information.

853 In the original design of the L1 calorimeter trigger, the trigger primitives are pro-
854 cessed by the Regional Calorimeter Trigger (RCT, upgraded to Calo Layer 1 after
855 LS2) which finds isolated and non-isolated electron/photon candidates [28]. At this
856 stage, electrons/photons candidates are treated together since they cannot be defini-
857 tively distinguished at this stage due to lack of tracking information in the L1 trigger.
858 The Global Calorimeter Trigger (GCT, upgraded to Calo Layer 2 after LS2) sorts
859 further the candidate electrons/photons, finds jets (classified as central, forward, and
860 tau) using the E_T sums and performs calibration of the clustered jet energies, and
861 calculates global quantities such as missing E_T . It sends the top four candidates of
862 each type to the global trigger (GT) [28].

863 Each of the L1 muon triggers has its own trigger logic [29]. The RPC strips are
864 connected to a Pattern Comparator Trigger (PACT), which forms trigger segments
865 that are used to build tracks and calculate p_T . The RPC logic also provides some
866 hit data to the CSC trigger system to resolve ambiguities caused by two muons in
867 the same CSC. The CSCs form local charged tracks (LCTs) from the cathode strips,
868 which are combined with the anode wire information. LCTs are combined into full
869 muon tracks and assigned p_T values.

870 The Global Muon Trigger (GMT) sorts the RPC, DT, and CSC muon tracks,
871 converts these tracks to the same η , ϕ , and p_T scale, and validates the muon sign [29].
872 It improves the trigger efficiency by merging muon candidates that were detected
873 in two complementary sub-systems (i.e. DT+RPC, or CSC+RPC). The GMT also
874 contains logic to correlate the found muon tracks with an $\eta-\phi$ grid of quiet calorimeter
875 towers to determine if the muons are isolated, as well as logic to remove duplicate
876 candidates originating in the overlap regions from both DT and CSC systems. The
877 final collection of muons are sorted based on their initial quality, correlation, and p_T ,
878 and the top four muons are sent to the Global Trigger [29].

879 Information from the GCT and GT are sent to the Global Trigger (GT), which

880 makes the Level-1 Accept (L1A) decision to either discard or accept the bunch crossing
881 [29]. This is accomplished by sorting ranked trigger objects that are accompanied by
882 positional information in η and ϕ , permitting the trigger to applying criteria with
883 thresholds that can vary based on the location of the trigger objects, and/or to
884 require trigger objects to be close to or opposite from each other. The GT L1A
885 decision arrives at the detector front end with a $3.8\ \mu\text{s}$ latency after the interaction
886 at a rate which is required to be less than 100 kHz, and triggers a full readout of the
887 detector for further processing.

888 **2.5.6 The High-Level Trigger**

889 The HLT is implemented in software running on a large computer farm of fast com-
890 mercial processors [30] [31]. The algorithms in HLT have access to full data from
891 all CMS sub-detectors, including the tracker, with full granularity and resolution.
892 The HLT reconstruction software is similar to what is used offline for full CMS data
893 analysis. As a result, the HLT can calculate quantities with a resolution compara-
894 ble to the final detector resolution, compared to the L1 Trigger. The HLT performs
895 more computationally-intensive algorithms, such as combining tau-jet candidates in
896 the calorimeter with high- p_T stubs in the tracker, to form a hadronic tau trigger. The
897 maximum HLT input rate from the L1 Trigger is 100 kHz, and the HLT output rate
898 is approximately 100 Hz.

899 The HLT contains trigger paths, each corresponding to a dedicated trigger [32].
900 A path consists of several steps implemented as software modules. Each HLT trigger
901 path must be seeded by one or more L1 trigger bits: the first module always looks
902 for a L1 seed, consisting of L1 bit(s) and L1 object(s). Each module performs a well-
903 defined task such as unpacking (raw to digitized quantities), reconstruction of physics
904 objects (electrons, muons, jet, missing transverse energy, etc.), making intermediate
905 decisions that trigger more detailed reconstruction modules, and calculating the final

906 decision for the trigger path. If an intermediate filter decision is negative, the rest of
907 the path is not executed, and the trigger rejects the event.

908 **2.5.7 Particle reconstruction**

909 To build a description of the physics objects present in the particle collision, the
910 basic elements from the detector layers (tracks and clusters of energy) are correlated
911 to identify each particle in the final state. Measurements from different sub-detectors
912 are combined to reconstruct the particle properties. This approach is called particle-
913 flow (PF) reconstruction [22]. Key to the success of the PF reconstruction is the
914 fine spatial granularity of the detector layers. Coarse-grained detectors can cause
915 the signals from different particles to merge, especially within jets. However, if the
916 subdetectors are sufficiently segmented to separate individual particles, it becomes
917 possible to produce a global event description that identifies all physics objects with
918 high efficiencies and resolution.

919 **2.5.8 Data storage and computational infrastructure**

920 The LHC generates over 15 petabytes (15 million gigabytes) of data every year, neces-
921 sitating a flexible computing system that can be accessed by researchers working at
922 the four main LHC experiments: ALICE, ATLAS, CMS, and LHCb. The Worldwide
923 LHC Computing Grid (WLCG) [33] is a global collaboration of computer centers that
924 links thousands of computers and storage systems in over 170 centers across 41 coun-
925 tries. These centers are arranged in “tiers”, and provide near real-time access to users
926 processing, analyzing, and storing LHC data. One of the final stages of data analy-
927 sis at LHC experiments is large-scale data processing taking place over distributing
928 computing, for instance, with the use of Condor [34], a distributed, scalable, flexible
929 batch processing system which accepts a computing job, allocates a resource to it,
930 executes it, and returns the result back to a user transparently.

931 Chapter 3

932 The Phase-2 Upgrade of CMS

933 3.1 High-Luminosity LHC and CMS

934 In order to sustain and extend the LHC’s physics discovery program and maintain
935 operability for a decade or more, the LHC is undergoing a major upgrade to the High-
936 Luminosity LHC (HL-LHC). In its final configuration, the HL-LHC will deliver a peak
937 luminosity of $7.5 \times 10^{34} \text{ cm}^{-2} \text{ s}^{-1}$, potentially leading to total integrated luminosity
938 of 4000 fb^{-1} after ten years of operations, scheduled to begin in 2027 [35]. This
939 integrated luminosity is about ten times the predicted luminosity reach of the LHC
940 in its initial configuration. To maximize the discovery potential of this unprecedented
941 amount of data, the CMS detector is undergoing Phase-2 upgrades in order to perform
942 high-precision measurements and searches for physics beyond the Standard Model in
943 the intense running conditions of the HL-LHC.

944 3.2 The Phase-2 Level-1 Trigger

945 To achieve the goals of the HL-LHC program and to ensure the collection of information-
946 rich datasets in the HL-LHC, the Phase-2 upgrade of the CMS Level-1 Trigger [35]
947 must be upgraded in conjunction with the CMS sub-detectors and their readouts, to

948 maintain physics selectivity. The HL-LHC will produce an intense hadronic environment
 949 corresponding to 200 simultaneous collisions per beam crossing, necessitating
 950 comprehensive upgrades of the trigger system outlined below.

951 To profit from the extended coverage and increased granularity of the upgraded
 952 CMS detector, the latency of the L1 trigger system (time available to produce a L1
 953 Accept signal) will be increased significantly from $3.8 \mu\text{s}$ to $12.5 \mu\text{s}$, with an increased
 954 maximum output bandwidth of 750 kHz [35]. With the increased latency, in addition
 955 to information from calorimeters and muon detectors (as in the Phase-1 system),
 956 information from the new tracker and high-granularity endcap calorimeter can also
 957 be included at L1 for the first time. This is illustrated in the functional diagram of
 958 the architecture of the Phase-2 trigger system in Fig. 3.1.

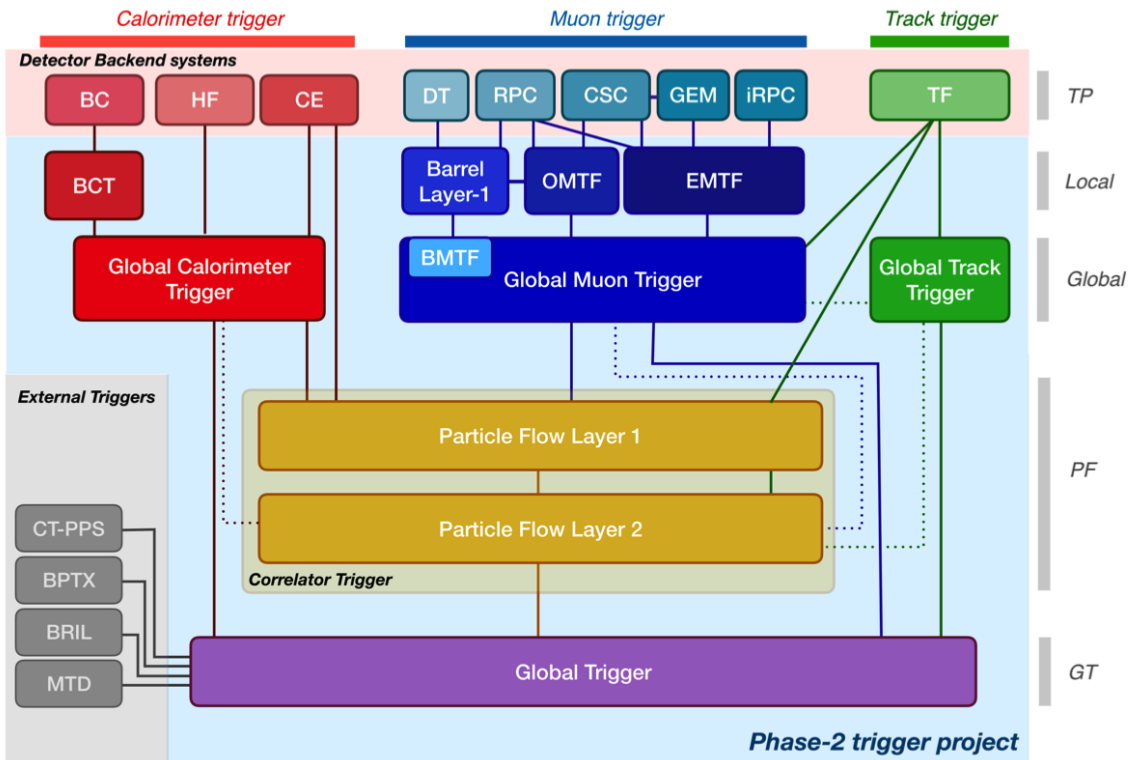


Figure 3.1: Functional diagram of the CMS L1 Phase-2 upgraded trigger design [35], showing the four trigger paths: calorimeter, muon, track, and Particle Flow. For the first time, tracking information will be available as early as the L1 Trigger.

959 The key feature of the Phase-2 L1 Trigger is the introduction of a correlator layer,

960 where algorithms produce higher-level trigger objects by combining information from
961 sub-detectors, with a selectivity approaching that of offline reconstruction in the
962 HLT [35]. Four independent data processing paths (grouped together in Fig. 3.1) are
963 implemented: tracking, calorimetry, muon systems, and particle-flow techniques:

- 964 • **Calorimeter Trigger path:** (*red*, Fig. 3.1) A barrel calorimeter trigger (BCT)
965 and the HGCAL backend are used to produce high-granularity information from
966 the calorimeters to produce high-resolution clusters and identification variables
967 used for later processing. Outputs from the BCT, HGCAL, and the HF are sent
968 to a global calorimeter trigger (GCT), where calorimeter-only objects such as
969 e/γ candidates, hadronically decaying tau lepton candidates, jets, and energy
970 sums are built.
- 971 • **Track Trigger path:** (*green*, Fig. 3.1) Tracks from the Outer Tracker are
972 reconstructed in the track finder (TF) processors as part of the detector back-
973 end. A global track trigger (GTT) will reconstruct the primary vertices of the
974 event, along with tracker-only based objects, such as jets and missing transverse
975 momentum.
- 976 • **Muon Trigger path:** (*blue*, Fig. 3.1) Trigger primitives are processed by
977 muon track finder algorithms, again separated into the barrel (barrel muon
978 track finder, BMTF), overlap (overlap muon track finder, OMTF), and endcap
979 (endcap muon track finder, EMTF). Standalone muons and stubs containing
980 information such as position, bend angle, and timing, as well as L1 tracks, are
981 sent to the global muon trigger (GMT).
- 982 • **Particle-Flow Trigger path:** (*yellow*, Fig. 3.1) The correlator trigger (CT)
983 aims to approach the performance of offline Particle Flow, and is implemented
984 in two layers. “Layer-1” produces the particle-flow candidates from matching

985 calorimeter clusters and tracks. “Layer 2” builds and sorts final trigger objects
986 and applies additional identification and isolation criteria.

The outputs from the above trigger paths are combined in the Global Trigger (GT) (*purple*, Fig. 3.1), which calculates the final trigger decision (Level-1 Accept), transmitting it to the Trigger Control and Distribution System (TCDS), which distributes it to the detector backend systems, initiating the readout to the DAQ. The GT also provides the interface to external triggers (*grey*, Fig. 3.1), such as triggers for the precision proton spectrometer (PPS), beam position and timing monitors (BPTX), and luminosity and beam monitoring (BRIL) detectors [35]. The design of the Phase-2 Level-1 Trigger allows for future inclusion of triggering information, for instance information about minimum ionizing particles (MIPs) from the MIP Timing Detector (MTD) [36].

3.3 Standalone Barrel Calorimeter electron/photon reconstruction

999 The reconstruction and identification of electrons and photons (e/γ) begin with the
 1000 trigger primitives of the barrel ECAL and HCAL detectors and endcap HGCAL
 1001 calorimeters, covering the pseudorapidity region $|\eta| < 3$. The barrel and endcap re-
 1002 gions of the detector are intrinsically different enough to warrant different approaches
 1003 to e/γ reconstruction. This work focuses on the Standalone Calorimeter e/γ recon-
 1004 struction taking place in the barrel (Fig. 3.2).

3.3.1 Phase-2 geometry of the ECAL Barrel trigger

¹⁰⁰⁶ In Phase-2, the upgrade of both on-detector and off-detector electronics for the barrel
¹⁰⁰⁷ calorimeters trigger primitive generator (TPG) will stream single crystal data from

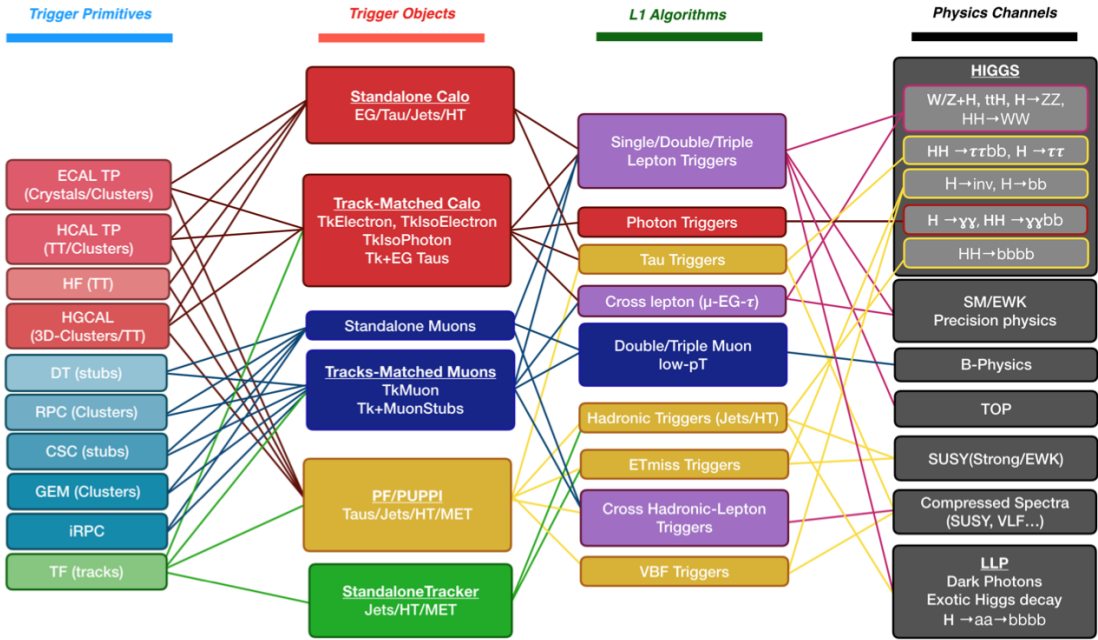


Figure 3.2: Summary of the links between the trigger primitives (*first column*), the trigger objects (*second column*), the Level-1 algorithms used in the menu (*3rd column*), and the physics channels (*4th column*), from [35], where a full description of the Phase-2 L1 algorithms can be found. This work focuses on developments for the Standalone Calorimeter electron and photon ("EG") reconstruction algorithm.

the on-detector to the backend electronics, in contrast to the lower-granularity output of the Phase-1 ECAL TPG that is restricted to providing trigger tower sums of 5×5 crystals [35]. A schematic representation of the geometry of the ECAL barrel in the Regional Calorimeter Trigger (RCT) is shown in Fig. 3.3. The barrel is spanned by 36 RCT cards, each spanning 17×4 towers in $\eta \times \phi$. Each RCT card is subdivided into five “regions” as shown in Fig. 3.4. After initial clustering and processing, the outputs of the RCT card are sent to the Global Calorimeter (GCT) trigger, which is processed in three cards as shown in Fig. 3.5.

3.3.2 Phase-2 electron/photon reconstruction algorithm

The standalone barrel algorithm for reconstructing and identifying electrons and photons in the Phase-2 Level-1 Trigger takes as input the digitized response of each crystal

1019 of the barrel ECAL, with a granularity 0.0175×0.0175 in $\eta \times \phi$, which is 25 times
1020 higher than the input to the Phase-1 trigger, which consisted of trigger towers with
1021 a granularity of 0.0875×0.0875 . In HCAL the tower size of 0.0875×0.0875 is un-
1022 changed. The trigger algorithm is designed to closely reproduce the algorithm used in
1023 the offline reconstruction, with limitations and simplifications due to trigger latency.

1024 In the RCT, an initial requirement of $p_T > 0.5$ GeV is imposed on the input
1025 trigger primitives (i.e. energies from the ECAL crystals and HCAL towers) to reject
1026 contribution from pileup. In one of the regions inside a RCT card (Fig. 3.4), the
1027 crystal containing the highest energy deposit is identified as the seed crystal, as shown
1028 in Fig. 3.6. The energy in the crystals in a window of size 3×5 in $\eta \times \phi$ around
1029 the seed cluster is added into a cluster. The energy is considered “clustered”. The
1030 process is repeated with the remaining “unclustered” energy, until up to four clusters
1031 are produced in the region.

1032 To improve e/γ identification and to reduce background contributions, identifica-
1033 tion and reconstruction algorithms are implemented at this stage:

- 1034 • Shower shape: The energy deposit sums around the seed crystal is computed in
1035 windows of size 2×5 and 5×5 (Fig. 3.6, *dashed lines*), with true e/γ clusters
1036 tending to produce showers that deposit most of their energy in a 2×5 region.
- 1037 • Bremsstrahlung recovery: e/γ tend to spread in the ϕ direction due to charged
1038 particles being bent by the magnetic field of the CMS solenoid. If sufficient
1039 energy comparable to the core 3×5 cluster is found in the adjacent 3×5
1040 windows (Fig. 3.6, *shaded yellow*), the energy is added to the core cluster and
1041 no longer considered unclustered energy.

1042 After parallel processing in the regions, the clusters in a RCT card are stitched
1043 together if they are located directly along the borders of a region (Fig. 3.3). The
1044 remaining unclustered ECAL energy is summed into ECAL towers.

1045 From each RCT card, the twelve highest-energy clusters, as well as any remaining
1046 unclustered energy, are sent to the GCT. Since each GCT card has information from
1047 sixteen RCT cards (Fig. 3.5), final stitching across the boundaries of the RCT cards
1048 is performed. One more identification algorithm is performed at this stage:

- 1049 • Isolation: One handle to reject backgrounds from e.g. pileup, comes from the
1050 tendency for background to be spread more uniformly across a large area in the
1051 detector, whereas genuine e/γ are expected to produce showers concentrated in
1052 the 3×5 crystal window. The energy sum in a large window of 7×7 in towers
1053 is computed and used to reject background.

1054 The performance of the standalone barrel e/γ algorithm in Phase-2 conditions is
1055 summarized in the efficiency and rates. The efficiencies are measured with a simulated
1056 Monte Carlo sample containing electrons. The rates are measured with a simulated
1057 minimum bias sample intended to closely mimic generic proton-proton collisions in
1058 the CMS detector. The performance of the Phase-2 emulator discussed in this work,
1059 which closely mimics the firmware logic and uses fixed-precision integers, is shown to
1060 be comparable to the previous emulator which used floats and idealized logic.

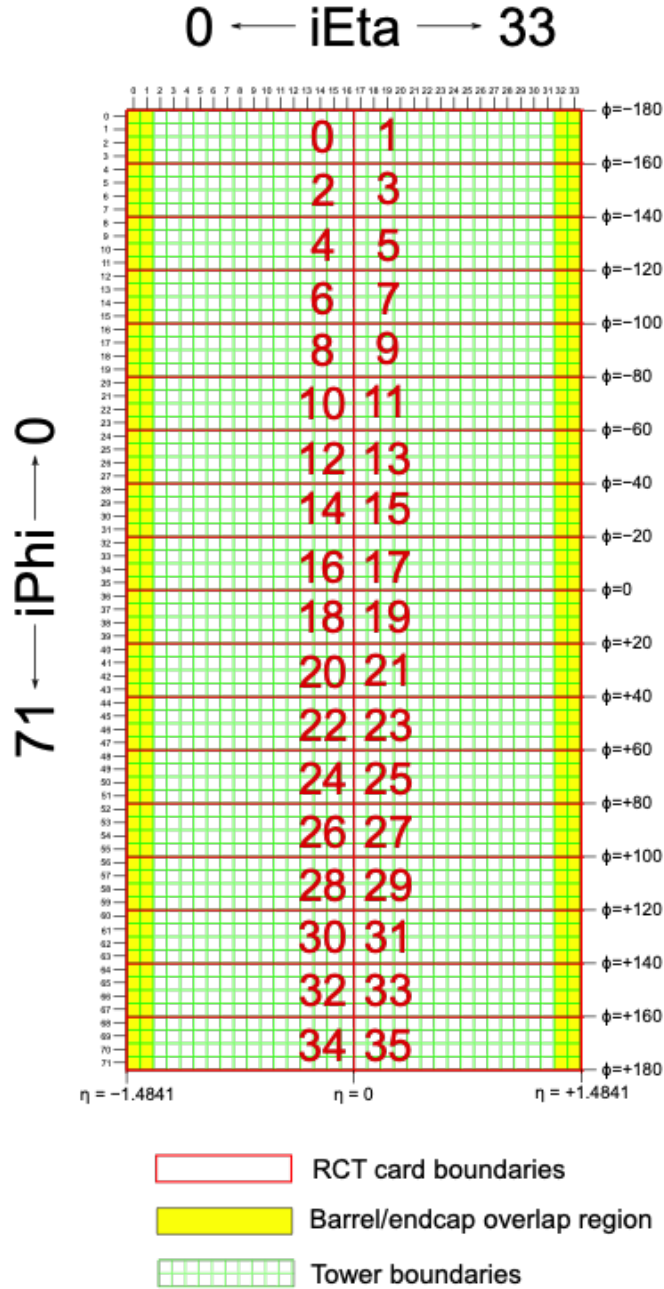


Figure 3.3: Schematic of the geometry of the Phase-2 ECAL barrel in the Regional Calorimeter Trigger (RCT), showing the division of the barrel region into 36 Regional Calorimeter Trigger (RCT) cards (*red*). Each card spans 17×4 towers in $\eta \times \phi$ (*green*), and each tower is 5×5 in single crystals in $\eta \times \phi$. Towers in the overlap region (*shaded yellow*) are read out to both the barrel and endcap.

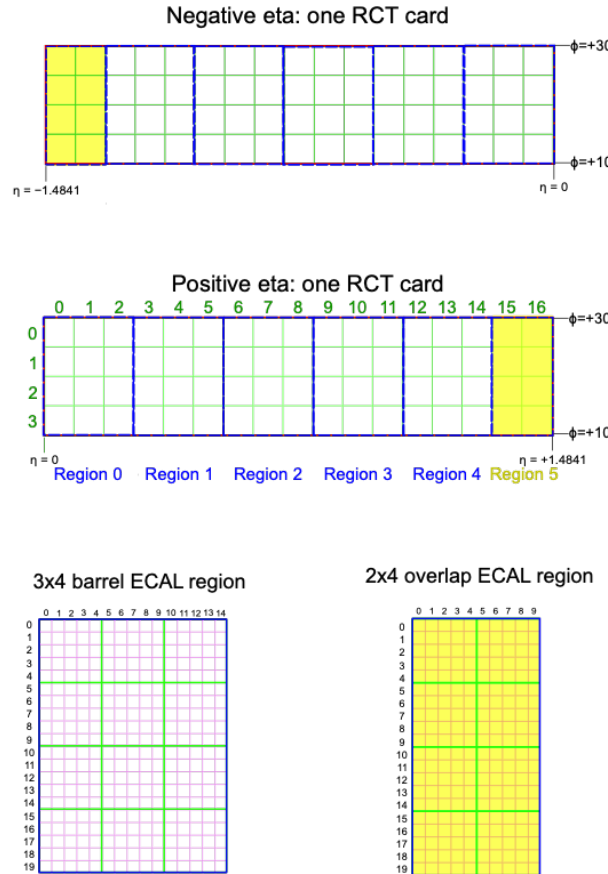


Figure 3.4: Schematic of two example RCT cards in the negative eta (*top*) and positive eta (*center*) regions of the ECAL barrel. Each RCT card is divided into five regions: four regions are of size 3×4 towers in $\eta \times \phi$ (*bottom left*), and a fifth smaller overlap region of size 2×4 towers (*bottom right*). Each tower is 5×5 ($\eta \times \phi$) in crystals.

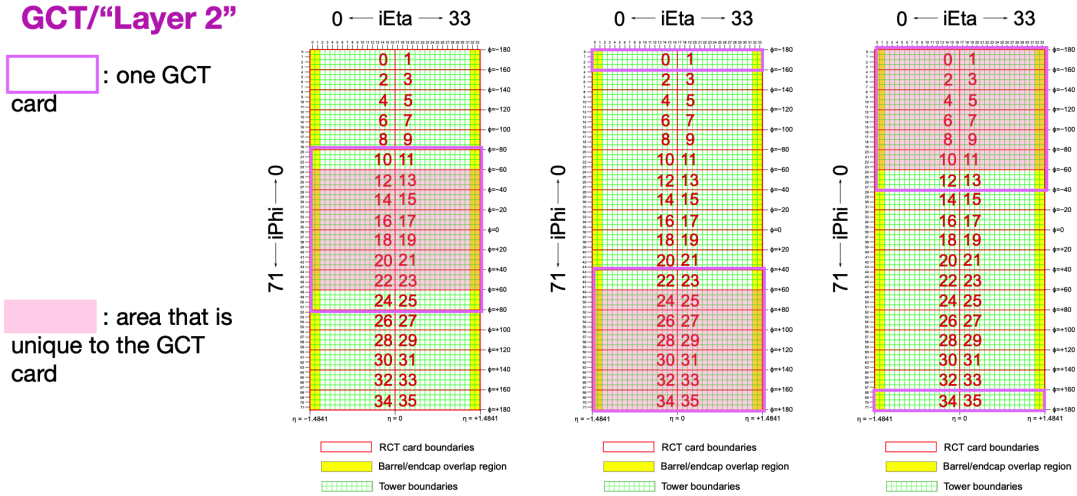


Figure 3.5: Schematic of the Phase-2 ECAL barrel in the Global Calorimeter Trigger (GCT), which will process the outputs of the Regional Calorimeter Trigger (RCT) in three cards (*magenta highlights*). Each card in the GCT processes the equivalent of sixteen RCT cards, with the center twelve being unique to that GCT card (*shaded pink*), and the remaining four processed in overlap with the other GCT cards.

3x4 barrel ECAL region

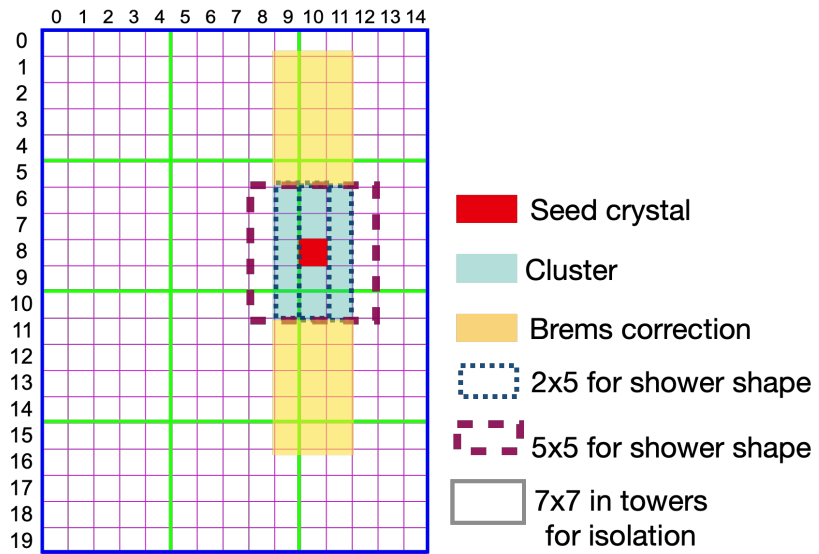


Figure 3.6: Illustration of an example electron/photon (e/γ) cluster in the Phase-2 Level-1 Trigger standalone barrel e/γ reconstruction, in a region of 15×20 crystals (3 \times 4 towers). Each small pink square is one crystal, the highest-granularity ECAL trigger primitives available to the L1 Trigger in Phase-2. The core cluster consists of the energy sum in a 3×5 window of crystals, (*shaded light blue*) centered around the seed crystal (*red*). Bremsstrahlung corrections are checked in the adjacent 3×5 windows in the ϕ direction (*shaded light yellow*). The relative energies in windows of size 2×5 and 5×5 in crystals (*dashed dark blue and dark red*) are used to compute shower shape variables to identify true e/γ objects. Lastly, an isolation sum is computed in a window of size 7×7 in towers (not shown in figure).

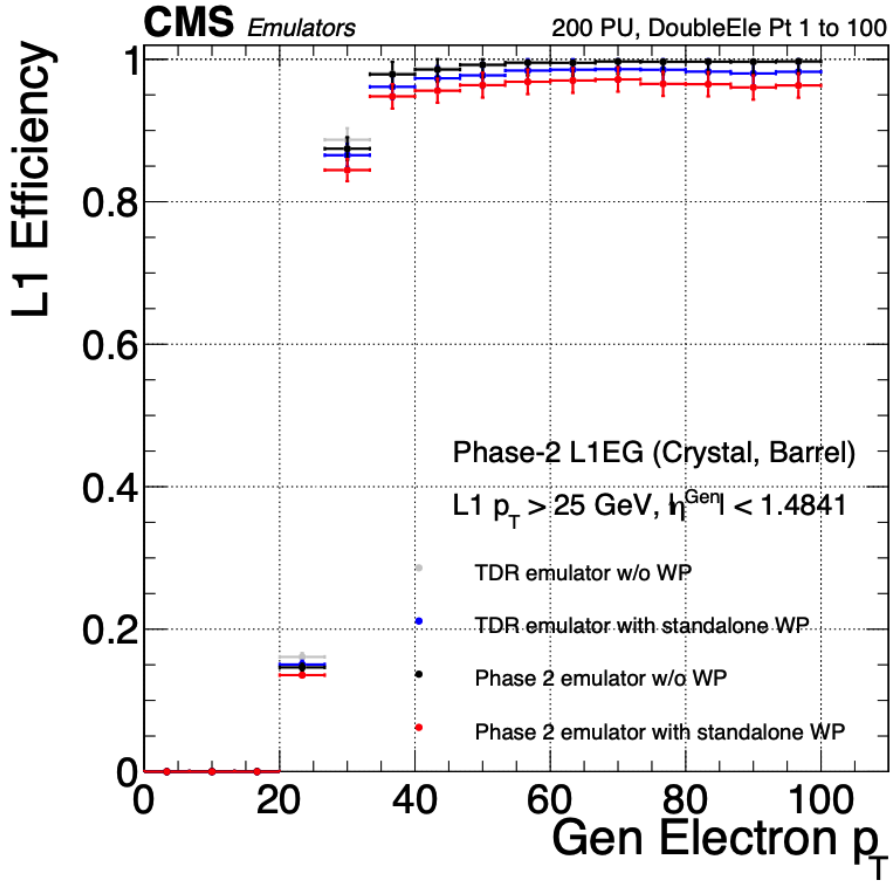


Figure 3.7: Efficiency of the standalone barrel e/γ reconstruction, measured in a simulated sample of electrons, as a function of the true electron’s transverse momentum p_T . The performance of the previous, idealized algorithm as shown in the 2021 Phase-2 TDR [35] with and without the isolation and shower shape discrimination variables (“standalone working point/ WP”) (*dark blue, grey*). The Phase-2 emulator discussed in this work with and without the same working point (*black, red*) is shown to have comparable performance.

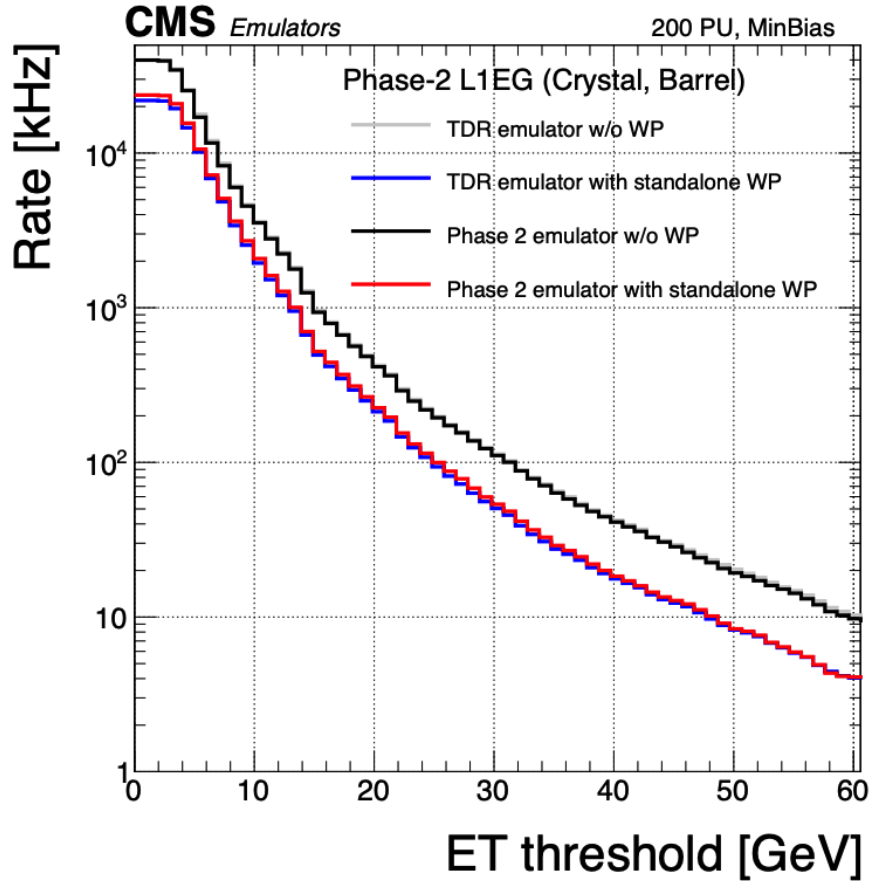


Figure 3.8: Rates of the standalone barrel e/γ reconstruction, evaluated on a minimum bias sample, measured as a function of the minimum energy (E_T) required of the reconstructed e/γ object in each event. The performance of the previous, idealized algorithm as shown in the 2021 Phase-2 TDR [35] with and without the isolation and shower shape discrimination variables (“standalone working point/ WP”) (*dark blue, grey*). The Phase-2 emulator discussed in this work with and without the same working point (*black, red*) is shown to have comparable performance.

1061 **Chapter 4**

1062 **Datasets and Monte Carlo samples**

1063 **4.1 Datasets used**

1064 The $h \rightarrow aa \rightarrow 2b2\tau$ analysis (CMS CADI line HIG-22-007) is based on proton-proton
1065 collision data at a center-of-mass energy of 13 TeV collected in full Run-2 (2016-
1066 18) with the CMS detector. The data analyzed corresponds to a total integrated
1067 luminosity of 138 fb^{-1} (36.33 fb^{-1} for 2016, 41.53 fb^{-1} for 2017, and 59.74 fb^{-1} for
1068 2018) [37] [38] [39]. The cumulative delivered and recorded luminosity versus time
1069 for 2015-2018 is shown in Fig. 4.1.

1070 Data collected with the single muon trigger is used for the $\mu\tau_h$ channel. For the
1071 $e\tau_h$ channel, data collected with the single electron trigger is used; and for the $e\mu$
1072 channel, data collected with the electron + muon trigger is used. A more in-depth
1073 discussion of the triggers used follows in a later section.

1074 A full list of samples used can be found in the full documentation [41] [42].

1075 **4.2 Monte Carlo samples**

1076 Modeling and computing observables originating from arbitrary physics processes at
1077 the tree level and at next-to-leading order (NLO) is performed by Monte Carlo (MC)

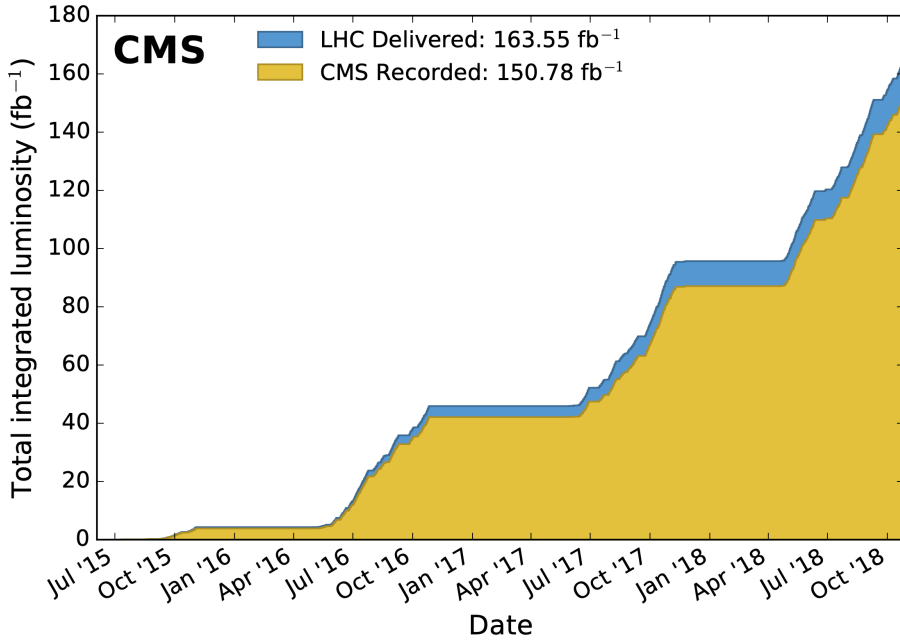


Figure 4.1: Cumulative delivered and recorded luminosity versus time for 2015-2018 at CMS, in proton-proton collision data only, at nominal center-of-mass energy [40].

event generators, such as Powheg and MadGraph5_amCNLO [43] [44]. The information generated, e.g. the computation of the differential cross sections and kinematics of the final state particles, is saved in a compressed file and used to generate MC samples that are used in physics analyses. The samples are digitized using GEANT4 [45], a platform used at the LHC and other facilities to comprehensively simulate the passage of particles through matter. The digitized samples are passed through the same detector reconstruction as real data events collected in the detector.

The samples for modeling the signal ($h \rightarrow aa \rightarrow 2b2\tau$ and $h \rightarrow a_1a_2$) in the 2HDM+S and TRSM are generated at tree-level, for a range of masses of the light neutral scalar a . For $h \rightarrow aa$, the mass hypotheses for the a range from $m_a = (12 \text{ GeV}, 62.5 \text{ GeV})$. For $h \rightarrow a_1a_2$, the mass hypotheses for the two light scalars span combinations of m_{a1} , m_{a2} ranging from $(12 \text{ GeV}, 62.5 \text{ GeV})$ for the two scalars.

1090 4.3 Embedded samples

1091 An important background for Higgs boson studies and searches for additional Higgs
1092 bosons is the decay of Z bosons into pairs of τ leptons ($Z \rightarrow \tau\tau$). An embedded tech-
1093 nique was developed in the context of Standard Model Higgs to $\tau\tau$ measurements, to
1094 model $Z \rightarrow \tau\tau$ decays, and was expanded to also model all Standard Model processes
1095 that contain $\tau\tau$ [46]. The embedded technique has since been used successfully at
1096 CMS for the Standard Model $H \rightarrow \tau\tau$ measurement, as well as searches for minimal
1097 supersymmetric extensions to the Standard Model (MSSM) [47] [48].

1098 Fig. 4.2 shows a schematic of how embedded samples are produced. Data events
1099 containing $Z \rightarrow \mu\mu$ decays are selected. In these events, all energy deposits of the
1100 recorded muons are removed, and are replaced with simulated tau leptons with the
1101 same kinematic properties as the removed muons. This results in a hybrid data format
1102 containing information from both observed and simulated events, as illustrated in Fig.
1103 4.2 [46].

1104 In the selection step of the embedded technique, events are selected with at least
1105 one of a set of $\mu\mu$ trigger paths, which require $p_T > 17(8)$ GeV for the leading
1106 (sub-leading) muons, and a minimum requirement between 3.8 and 8.0 GeV on the
1107 invariant di-muon mass $m_{\mu\mu}$ [46]. The offline reconstructed muons must match the
1108 objects at trigger level and also have offline $p_T > 17(8)$ GeV. They must have $|\eta| < 2.4$
1109 and be located at a distance $|d_z| < 0.2$ cm to the primary vertex along the beam
1110 axis. To form a Z boson candidate, each muon is required to originate from a global
1111 muon track. The muon pairs must have opposite charges with an invariant mass of
1112 $m_{\mu\mu} > 20$ GeV. If more than two di-muon pairs are found, the pair with the invariant
1113 mass closest to the Z boson mass (91.19 GeV) is chosen.

1114 This selection is designed to be tight enough to ensure a high purity of genuine
1115 $\mu\mu$ events, and also loose enough to minimize biases of the embedded event samples.
1116 Isolation requirements are avoided, since they would introduce a bias towards less

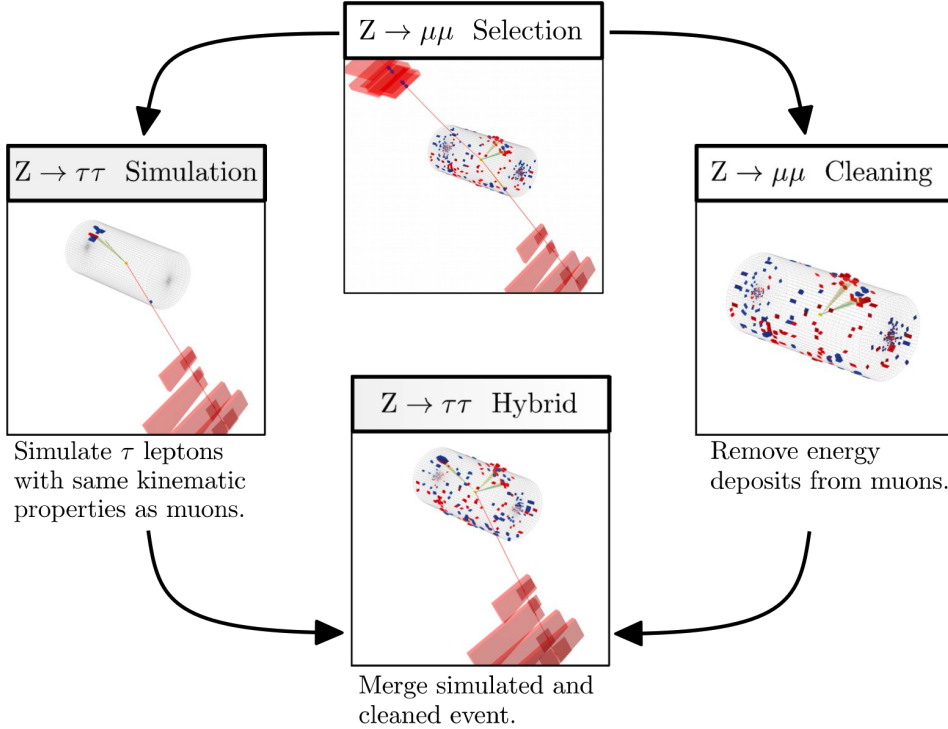


Figure 4.2: Schematic view of the four main steps of the embedding technique for τ leptons, as described in Section 4.3 [46]. A $Z \rightarrow \mu\mu$ event is selected in data ($Z \rightarrow \mu\mu$ selection), all of the energy deposits associated with the muons are removed ($Z \rightarrow \mu\mu$ cleaning), and two τ leptons and their decays are simulated in an empty detector ($Z \rightarrow \tau\tau$ simulation). Lastly, all energy deposits of the simulated τ decays are combined with the data event ($Z \rightarrow \tau\tau$ hybrid).

hadronic activity in the vicinities of the embedded leptons that will appear more isolated than expected in data. The selection results in an expected mixture of events summarized in Table 4.1 from [46]. $Z \rightarrow \mu\mu$ is the dominant process modeled by the embedded technique, with $t\bar{t}$, QCD, and diboson and single top processes becoming more significant when considering events with b-tag jets.

The advantage of the embedded technique is that aspects of the event that are difficult to model and describe are directly taken from data, resulting in a better data description than can be achieved with only the $Z \rightarrow \tau\tau$ simulation [46]. The simulation must be tuned extensively to accurately model aspects of the data, such as time-dependent pileup profiles, the production of additional jets, e.g. in multijet and vector boson fusion topologies, the number of reconstructed primary interaction

Process	Fraction (%)		
	Inclusive	$m_{\mu\mu} > 70 \text{ GeV}$	N(b-tag jets) > 0
$Z \rightarrow \mu\mu$	97.36	99.11	69.25
QCD	0.84	0.10	2.08
$t\bar{t}$	0.78	0.55	25.61
$Z \rightarrow \tau\tau$	0.71	0.05	0.57
Diboson, single t	0.17	0.17	2.35
W+jets	0.08	0.02	0.14

Table 4.1: Expected event composition after selecting two muons in the embedded technique [46], before additional cuts (i.e. *inclusive*, *column 2*), and after adding a requirement on the di-muon mass $m_{\mu\mu} > 70 \text{ GeV}$ (*column 3*), or a requirement on the number of b-tag jets in the event (*column 4*).

1128 vertices, and the missing transverse momentum p_T^{miss} . Since all events with genuine
 1129 $\tau\tau$ are estimated with samples made with the embedded technique (referred to as
 1130 embedded samples from here on), events in Monte Carlo simulation with genuine $\tau\tau$
 1131 are not used, in order to avoid double-counting.

¹¹³² **Chapter 5**

¹¹³³ **Object reconstruction and**
¹¹³⁴ **corrections applied**

¹¹³⁵ In this chapter on object reconstruction and corrections, Section 5.1 reviews the
¹¹³⁶ physical properties of the objects most pertinent to the analyses presented in this
¹¹³⁷ work: taus (τ), muons (μ), electrons (e), and jets, with a focus on jets originating from
¹¹³⁸ b quarks (b-flavor jets), as well as the methodology used to reconstruct the particles
¹¹³⁹ from their characteristic signatures in the CMS detector. Section 5.2 describes the
¹¹⁴⁰ method used to reconstruct the invariant full $\tau\tau$ mass which is used for the final signal
¹¹⁴¹ extraction. Lastly, Section 5.3 describes the corrections applied to the simulated
¹¹⁴² samples which improve their modeling of data.

¹¹⁴³ **5.1 Object reconstruction**

¹¹⁴⁴ **5.1.1 Taus**

¹¹⁴⁵ The tau (τ) is the heaviest known lepton. With a rest mass of 1776.86 MeV, it can
¹¹⁴⁶ decay to not only electrons and muons, but also hadrons. The mean lifetime of the τ
¹¹⁴⁷ is $\tau = 290 \times 10^{-15}$ seconds, corresponding to $c\tau = 87.03 \mu\text{m}$, which is short enough

₁₁₄₈ that taus decay in the CMS detector before reaching the detector elements.

₁₁₄₉ In two thirds of the cases, τ leptons decay hadronically, typically into one or three
₁₁₅₀ charged mesons (predominantly π^+ , π^-), often accompanied by neutral pions (that
₁₁₅₁ decay $\pi^0 \rightarrow \gamma\gamma$), and a ν_τ . These hadronic decays are denoted τ_h . In the remainder of
₁₁₅₂ the decays, the tau decays to the lighter leptons (electron or muon), termed leptonic
₁₁₅₃ decays. In all cases, at least one neutrino is produced, resulting in missing transverse
₁₁₅₄ energy in the CMS detector. The tau's largest decay branching ratios (proportional
₁₁₅₅ to probability of decay) are listed below [26]:

₁₁₅₆ • 17.8% decay to $e^- \bar{\nu}_e \nu_\tau$

₁₁₅₇ • 17.4% decay to $\mu^- \bar{\nu}_\mu \nu_\tau$

₁₁₅₈ • 25.5% decay to $\pi^- \pi^0 \nu_\tau$ (ρ^- resonance at 770 MeV)

₁₁₅₉ • 10.8% decay to $\pi^- \nu_\tau$

₁₁₆₀ • 9.3% decay to $\pi^- \pi^0 \pi^0 \nu_\tau$ (a_1^- resonance at 1200 MeV)

₁₁₆₁ • 9.0% decay to $\pi^- \pi^- \pi^+ \nu_\tau$ (a_1^- resonance at 1200 MeV)

₁₁₆₂ The neutrinos escape undetected from the CMS detector and are not considered
₁₁₆₃ in the reconstruction. Charged hadrons leave tracks in the tracking detector before
₁₁₆₄ being absorbed in the hadronic calorimeter; in CMS tau reconstruction terminology,
₁₁₆₅ they are often called “prongs”, i.e. the dominant τ_h decay modes are termed “1 prong”
₁₁₆₆ (π^\pm), “1 prong + $\pi^0(s)$ ”, and “3-prong”. Neutral pions decay to two photons which
₁₁₆₇ lose their energy in the electromagnetic calorimeter. Taus that decay to electrons
₁₁₆₈ and muons, are typically triggered on and reconstructed as electrons and muons
₁₁₆₉ respectively.

1170 **Hadron plus strips (HPS) reconstruction of τ_h**

1171 At CMS, hadronically decaying tau leptons are reconstructed with the hadron plus
1172 strips (HPS) algorithm [49] [50]. The HPS algorithm capitalizes on photon conversions
1173 in the CMS tracker material, which originate from the neutral pion (π^0) decaying
1174 to two photons. The bending of electron/positron tracks due to the CMS solenoid
1175 magnetic field leads to a spread of the neutral pions' calorimeter signatures in the ϕ
1176 direction. This motivates the reconstruction of photons in “strips”: objects that are
1177 built out of PF photons and electrons. The strip reconstruction starts with centering
1178 a strip on the most energetic electromagnetic particle in a PF jet. Among other
1179 electromagnetic particles located in a window of size $\Delta\eta = 0.05$ and $\Delta\phi = 0.20$
1180 around the strip center, the most energetic one is associated with the strip and its
1181 momentum is added to the strip momentum. This is repeated iteratively until no
1182 further particles can be associated. Lastly, strips satisfying a requirement of $p_T^{\text{strip}} > 1$
1183 GeV are combined with charged hadrons to reconstruct individual τ_h decay modes,
1184 where h stands for both π and K :

1185 • *Single hadron:* $h^- \nu_\tau$ and $h^- \pi^0 \nu_\tau$ decay modes, in which the neutral pions have
1186 too little energy to be reconstructed as strips.

1187 • *One hadron + one strip:* $h^- \pi^0 \nu_\tau$ decay modes, where the photons from the π^0
1188 decay are close together in the calorimeter.

1189 • *One hadron + two strips:* $h^- \pi^0 \nu_\tau$ decay modes, where the photons from the π^0
1190 decay are well separated.

1191 • *Three hadrons:* $h^- h^+ h^- \nu_\tau$ decay modes. The three charged hadrons are re-
1192 quired to originate from the same secondary vertex.

1193 The $h^- \pi^0 \pi^0 \nu_\tau$ and $h^- h^+ h^- \pi^0 \nu_\tau$ decay modes do not have their own treatment are
1194 reconstructed with the above topologies.

1195 In the HPS algorithm, the direction of the reconstructed tau momentum $\vec{p}_T^{\tau_h}$
1196 is required to fall within a distance of $\Delta R = 0.1$ from the original PF jet. All
1197 charged hadrons and strips are required to be contained within a cone of size $\Delta R =$
1198 $(2.8 \text{ GeV})/p_T^{\tau_h}$, from the τ_h as reconstructed by the HPS.

1199 All charged hadrons are assumed to be pions, and they are required to be consis-
1200 tent with the masses of the intermediate meson resonances (if applicable), with the
1201 following allowed windows for candidates: 50-200 MeV for π^0 , 0.3-1.3 GeV for ρ , and
1202 0.8-1.5 GeV for a_1 . If the τ_h decay is compatible with more than one hypothesis, the
1203 one giving the highest $p_T^{\tau_h}$ is chosen. Lastly, an isolation requirement is applied: aside
1204 from the τ_h decay products, no charged hadrons or photons can be present within
1205 an isolation cone of size $\Delta R = 0.5$ around the direction of the τ_h . The outputs of
1206 the HPS algorithm are the reconstructed decay mode and the visible four-momentum
1207 (i.e. the four-momenta of all decay products excluding the neutrinos).

1208 DeepTau for identifying τ_h

1209 The identification of τ_h candidates in CMS has historically been divided into separate
1210 discriminators against jets, electrons, and muons. Discriminators versus jets and
1211 electrons use information from derived quantities, such as the p_T sum of particles
1212 near the τ_h axis. Building on the previous multivariate analysis (MVA) classifier [51]
1213 based on a boosted decision tree (BDT), DeepTau is a more recent classifier based on a
1214 deep neural network (DNN) that simultaneously discriminates against jets, electrons,
1215 and muons. The DNN uses a combination of high-level inputs, similar to previous
1216 algorithms, and also uses convolutional layers in $\eta\text{-}\phi$ space to process information
1217 from all reconstructed particles near the τ_h axis. Convolutional layers are based on
1218 the principle that an image can be processed independently of its position.

1219 The final DeepTau discriminators against jets, muons, and electrons are given by

$$D_\alpha(y) = \frac{y_\tau}{y_\tau + y_\alpha} \quad (5.1)$$

1220 where y_τ (y_α) are estimates of the probabilities for the τ_h candidate to come from
1221 a genuine τ_h (jet, μ , e). Working points for each discriminator with different τ_h
1222 identification efficiencies are defined for D_e , D_μ , and D_{jet} , for usage in physics analyses
1223 and derivation of data-to-simulation corrections [52].

1224 5.1.2 Muons

1225 Muons are the next lightest lepton after taus, with a mass of 105.66 MeV and a
1226 mean lifetime of $\tau = 2.20 \times 10^{-6}$ seconds, or $c\tau = 658.64$ m. At CMS, muons are
1227 identified with requirements on the quality of the track reconstruction and on the
1228 number of measurements in the tracker and the muon systems [53]. In the standard
1229 CMS reconstruction, tracks are first reconstructed independently in the inner tracker
1230 (tracker track) and in the muon system (standalone-muon track). Next, these tracks
1231 are processed in two different methods.

1232 The first is Global Muon reconstruction (outside-in) [53], which fits combined hits
1233 from the tracker track and standalone-muon track, using the Kalman-filter technique.
1234 At large transverse momenta, $p_T \gtrsim 200$ GeV, the global-muon fit can improve the
1235 momentum resolution compared to the tracker-only fit.

1236 The second is Tracker Muon reconstruction (inside-out) [53], which starts with
1237 tracker tracks with $p_T > 0.5$ GeV and total momentum $p_T > 2.5$ GeV. These tracks
1238 are extrapolated outwards to the muon system and matched to detector segments
1239 there, taking into account the magnetic field, expected energy losses, and multiple
1240 Coulomb scattering in the detector material. Tracker Muon reconstruction is more
1241 efficient than the Global Muon reconstruction at low momenta, $p \lesssim 5$ GeV, because

it only requires a single muon segment in the muon system, whereas Global Muon reconstruction typically requires segments in at least two muon stations.

To further suppress fake muons from decay in flight, isolation cuts are used. A relative isolation variable is defined to quantify the energy flow of particles near the muon trajectory. A relative isolation is defined similarly for muons and electrons:

$$I^\ell \equiv \frac{\sum_{\text{charged}} p_T + \max(0, \sum_{\text{neutral}} p_T - \frac{1}{2} \sum_{\text{charged, PU}} p_T)}{p_T^\ell} \quad (5.2)$$

where $\sum_{\text{charged}} p_T$ is the scalar sum of the p_T of the charged particles originating from the primary vertex and located in a cone of size $\Delta R = \sqrt{(\Delta\eta)^2 + (\Delta\phi)^2} = 0.4(0.3)$ centered on the direction of the muon (electron). The sum $\sum_{\text{neutral}} p_T$ is the equivalent for neutral particles. The sum $\sum_{\text{charged, PU}} p_T$ is the scalar sum of the p_T of the charged hadrons in the cone originating from pileup vertices. The factor 1/2 comes from simulation estimations, which find that the ratio of neutral to charged hadron production in the hadronization process of inelastic pp collisions is 1/2. Thus the subtracted term is intended to subtract contribution from pileup, from the neutral particle contribution to the isolation sum. Finally, this is divided by the lepton transverse momentum, p_T^ℓ .

5.1.3 Electrons

Electrons are the lightest lepton with a mass of 0.511 MeV. At CMS, electrons are reconstructed by associating a track reconstructed in the silicon tracking detector with a cluster of energy in the ECAL. Performance is maximized via a combination of a stand-alone approach and the complementary global particle-flow approach [54].

In the stand-alone approach, the electron energy, which is typically spread over several crystals of the ECAL, is clustered with the “hybrid” algorithm in the barrel and the “multi- 5×5 ” in the endcaps [54]. The hybrid algorithm collects energy in a

1265 small window in η and an extended window in ϕ . It identifies a seed crystal, and adds
1266 arrays of 5×1 crystals in $\eta \times \phi$ in a range of $N = 17$ crystals in both directions of
1267 ϕ , if their energies exceed a minimum threshold, thus forming a supercluster (SC). In
1268 the endcap, crystals are not arranged in an $\eta \times \phi$ geometry; instead clusters are build
1269 around seed crystals in clusters of 5×5 crystals that can partly overlap. Nearby
1270 clusters are grouped into a supercluster, and energy is recovered from associated
1271 deposits in the preshower.

1272 In the PF reconstruction [54], PF clusters are reconstructed by aggregating around
1273 a seed all contiguous crystals with energies two standard deviations above the elec-
1274 tronic noise observed at the beginning of a data-taking run. The energy of a given
1275 crystal can be shared among two or more clusters.

1276 The electron track reconstruction is performed in two ways [54]: the ECAL-based
1277 seeding, which begins with the SC energy and positioning, and the tracker-based
1278 seeding (part of the PF reconstruction algorithm), which uses tracks reconstructed
1279 from the general algorithm for charged particles, extrapolated towards the ECAL and
1280 matched to an SC. Kalman filter (KF) tracks with a small number of hits or that are
1281 not well-fitted, are re-fitted with a dedicated Gaussian sum Filter (GSF).

1282 A global identification variable [54] is defined using a multivariate analysis (MVA)
1283 technique that combines information on track observables (kinematics, quality of the
1284 KF track and GSF track), the electron PF cluster observables (shape and pattern),
1285 and the association between the two (geometric and kinematic observables). For
1286 electrons seeded only through the tracker-based approach, a weak selection is applied
1287 on this MVA variable. For electrons seeded through both approaches, a logical OR is
1288 taken.

1289 Electron isolation, i.e. the presence of energy deposits near the electron trajectory,
1290 is a separate key handle in rejecting significant background. Compared to isolated
1291 electrons, electrons from misidentified jets or genuine electrons within a jet resulting

1292 from semileptonic decays of b or c quarks tend to have significant energy deposits
 1293 near the primary trajectory [54]. Offline analyses benefit from the PF technique
 1294 for defining isolation, which sums the PF candidates reconstructed located within a
 1295 specified isolation cone around the electron candidate, as in Eqn. 5.2.

1296 5.1.4 Jets

1297 The vast majority of processes of interest at the LHC contains quarks or gluons in
 1298 the final state, but these particles cannot be observed directly. In a process called
 1299 hadronization, they fragment into spatially-grouped collections of particles called jets,
 1300 which can be detected in the tracking and calorimeter systems. Hadronization and
 1301 the subsequent decays of unstable hadrons can produce hundreds of nearby particles
 1302 in the CMS detector. Jets are reconstructed by the PF algorithm (PF jets), or from
 1303 the sum of the ECAL and HCAL energies deposited in the calorimeter towers (Calo
 1304 jets). In PF jets, typically used in offline analyses, jets are built using the anti- k_T
 1305 (AK) clustering algorithm [55]. The anti- k_T algorithm iterates over particle pairs and
 1306 finds the two that are closest in a distance measure d , and determines whether to
 1307 combine them:

$$d_{ij} = \min(p_{T,i}^{-2}, p_{T,j}^{-2}) \frac{\Delta_{ij}^2}{R^2}, \text{ combine when } d_{ij} < p_{T,i}^{-2}; \text{ stop when } d_{ij} > p_{T,i}^{-2} \quad (5.3)$$

1308 where $\Delta_{ij}^2 = (\eta_i - \eta_j)^2 + (\phi_i - \phi_j)^2$ and $p_{T,i}$, η_i , ϕ_i are the transverse momentum, rapid-
 1309 ity, and azimuthal angle of particle i . The power -2 means that higher-momentum
 1310 particles are clustered first, leading to jets that tend to be centered on the hardest
 1311 (highest p_T) particle.

1312 There are several methods to remove contributions of pileup collisions from jet
 1313 clustering [56]:

- 1314 • Charged hadron subtraction (CHS), which removes all charged hadron candi-

1315 dates associated with a track that is not associated with the primary vertex.

- 1316 • PileUp Per Particle Identification (PUPPI), which weighs input particles based
1317 on their likelihood of arising from pileup. QCD particles tend to have a collinear
1318 structure, compared to soft diffuse radiation coming from pileup. The local
1319 shape for charged pileup, used as a proxy for all pileup particles, is used on an
1320 event-by-event basis to calculate a weight for each particle. PUPPI is deployed
1321 in Run-2 and is more performant than CHS in high pileup scenarios.

1322 5.1.5 B-flavored jets

1323 Jets that arise from bottom-quark hadronization (b-flavor jets) have overwhelming
1324 background from processes involving jets from gluons (g) and light-flavor quarks (u, d,
1325 s), and from c-quark fragmentation. The ability to identify b-flavor jets, or b-tagging,
1326 exploits the b hadrons' relatively large masses, long lifetimes, and daughter particles
1327 with hard momentum spectra [55].

1328 The impact parameter (IP) of a track is the 3-dimensional distance between the
1329 track and the primary vertex (PV) at the point of closest approach. The IP is positive
1330 if the track originates from the decay of particles travelling along the jet axis. The
1331 resolution of the IP depends on the p_T and η of the track, motivating the use of the
1332 impact parameter significance S_{IP} (ratio of the IP to its estimated uncertainty) as an
1333 observable [55].

1334 Because of the large but finite lifetimes of the b hadrons, b hadrons tend to
1335 travel a short distance before decaying at a secondary vertex (SV), which can be
1336 measured and reconstructed separately from the primary vertex due to the excellent
1337 position resolution of the pixel detector [55]. Previous b-tagging algorithms (e.g.
1338 CSV, cMVAv2, and DeepCSV) have capitalized on variables such as the presence of
1339 a SV, the flight distance and direction (computed from the vector between the PV
1340 and the SV), and kinematics of the system of associated secondary tracks (e.g. track

1341 multiplicity, mass, and energy).

1342 The DeepJet (formerly known as DeepFlavour) algorithm [57] is a deep-neural-
1343 network multi-classification algorithm, which uses 16 properties of up to 25 charged
1344 and 6 properties of 25 neutral particle-flow jet constituents, as well as 17 properties
1345 from up to 4 secondary vertices associate with the jet. Compared to the previous clas-
1346 sifying algorithm DeepCSV, DeepJet has been demonstrated to have higher efficiency
1347 with lower misidentification probability in Phase-1 data [58].

1348 5.2 Reconstruction of the $\tau\tau$ mass

1349 The final signal extraction is done to the total $\tau\tau$ mass, which is estimated from the
1350 visible $\tau\tau$ mass using the FastMTT algorithm [59]. FastMTT is based on the SVFit
1351 algorithm, originally developed for the Standard Model $H \rightarrow \tau\tau$ analysis [60]. Both
1352 the SVFit algorithms, and the FastMTT algorithm, are described below, to give a
1353 complete picture of how tau decays are parameterized.

1354 To specify a hadronic τ decay, six parameters are needed [60]: the polar and
1355 azimuthal angles of the visible decay product system in the τ rest frame, the three
1356 boost parameters from the τ rest frame to the laboratory frame, and the invariant
1357 mass m_{vis} of the visible decay products. For a leptonic τ decay, two neutrinos are
1358 produced, and a seventh parameter, the invariant mass of the two-neutrino system, is
1359 necessary. The unknown parameters are constrained by four observables that are the
1360 components of the four-momentum of the system formed by the visible decay products
1361 of the τ lepton, measured in the laboratory frame. The remaining unconstrained
1362 parameters for hadronic and leptonic τ decays are thus:

- 1363 • The fraction of the τ energy in the laboratory frame carried by the visible decay
1364 products,
- 1365 • ϕ , the azimuthal angle of the τ direction in the laboratory frame,

- 1366 • $m_{\nu\nu}$, the invariant mass of the two-neutrino system in leptonic τ decays (for
 1367 hadronic τ decays, $m_{\nu\nu}$ is set to 0).

1368 E_x^{miss} and E_y^{miss} , the x and y components of the missing transverse energy \vec{E}_T^{miss}
 1369 provide two further constraints.

1370 **5.2.1 Original SVFit “standalone”: maximum likelihood**

1371 In one of the original versions of SVFit, called “standalone” SVFit [60], a maximum
 1372 likelihood fit method is used to reconstruct the mass $m_{\tau\tau}$ by combining the measured
 1373 observables E_x^{miss} and E_y^{miss} with a likelihood model that includes terms for the τ
 1374 decay kinematics and the \vec{E}_T^{miss} resolution [60]. The likelihood function $f(\vec{z}, \vec{y}, \vec{a}_1 \vec{a}_2)$
 1375 of the parameters $\vec{z} = (E_x^{\text{miss}}, E_y^{\text{miss}})$ in an event is constructed, where the remaining
 1376 parameters are the kinematics of the two τ decays, denoted $\vec{a}_1 = (x_1, \phi_1, m_{\nu\nu,1})$ and
 1377 $\vec{a}_2 = (x_2, \phi_2, m_{\nu\nu,2})$, and the four-momenta of the visible decay products with the
 1378 measured values $\vec{y} = (p_1^{\text{vis}}, p_2^{\text{vis}})$.

1379 The likelihood f is the product of three likelihood functions. The first two likelihood
 1380 functions model the decay parameters \vec{a}_1 and \vec{a}_2 of the two τ leptons. For leptonic
 1381 decays, the likelihood function is modeled using matrix elements for τ decays,
 1382 and integrated over the allowed phase space $0 \leq x \leq 1$ and $0 \leq m_{\nu\nu} \leq m_\tau \sqrt{1-x}$. For
 1383 hadronic τ decays, a model based on the two-body phase space is used and integrated
 1384 over $m_{\text{vis}}^2/m_{\tau\tau}^2 \leq x \leq 1$. The third likelihood function quantifies the compatibility of
 1385 a τ decay hypothesis with the reconstructed \vec{E}_T^{miss} in an event, assuming the neutrinos
 1386 are the only source of missing transverse energy. The expected \vec{E}_T^{miss} resolution
 1387 is represented by a covariant matrix, estimated on an event-by-event basis using a
 1388 significance algorithm [61].

1389 5.2.2 “Classic SVFit” with matrix element

1390 Classic SVFit is an improved algorithm of the original “standalone” SVFit using the
 1391 formalism of the matrix element (ME) method [59]. In the ME method, an estimate
 1392 for the unknown model parameter Θ (here, the mass $m_{\tau\tau}$) is obtained by maximizing
 1393 the probability density \mathcal{P} . The key ingredients of the probability density are the
 1394 squared modulus of the matrix element $|\mathcal{M}(\mathbf{p}, \Theta)|^2$ and the transfer function $W(\mathbf{y}|\mathbf{p})$
 1395 (probability density to observe the measured observables \mathbf{y} given the phase space
 1396 point \mathbf{p}). The best estimate $m_{\tau\tau}$ is obtained by computing the probability density \mathcal{P}
 1397 for a range of mass hypotheses and finding the value of $m_{\tau\tau}$ that maximizes \mathcal{P} .

1398 Distributions illustrating the performance of the classic matrix element SVFit
 1399 algorithm are shown in Fig. 5.1 from [59], showing the di-tau mass after and before
 1400 application of SVFit to recover energy lost to neutrinos. The SVFit algorithm is
 1401 found to improve the sensitivity of the Standard Model $H \rightarrow \tau\tau$ analysis performed
 1402 by CMS by about 30%, compared to performing the same analysis using only the
 1403 visible mass m_{vis} .

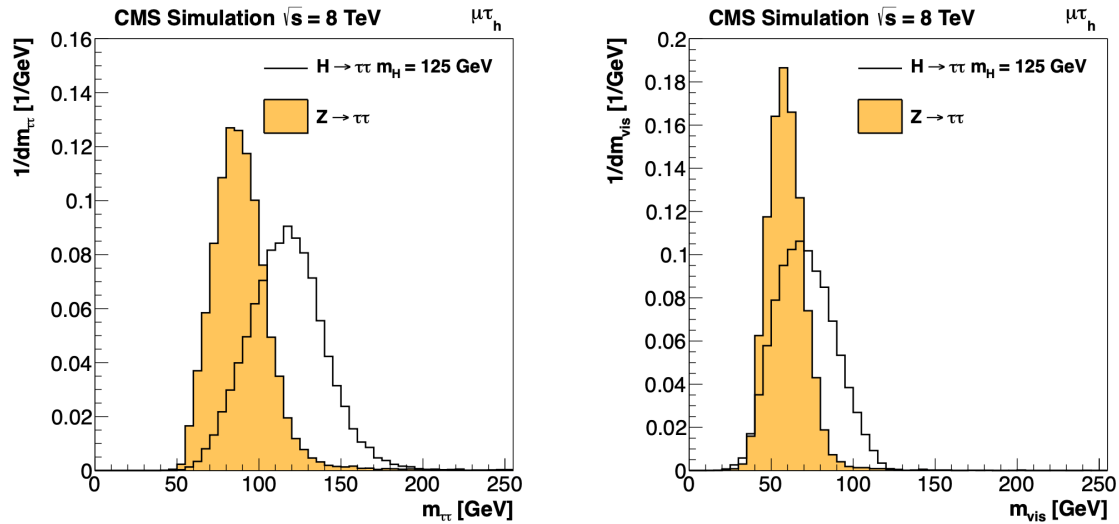


Figure 5.1: Distributions from [59], of $m_{\tau\tau}$ after reconstruction with the original SVFit algorithm (*left*), and before SVFit with only the visible tau decay products (*right*), for $H \rightarrow \tau\tau$ signal events of mass $m_H = 125$ GeV (*black line*) and the $Z/\gamma^* \rightarrow \tau\tau$ background (*orange, solid*), in the decay channel $\tau\tau \rightarrow \mu\tau_h$.

1404 5.2.3 FastMTT: optimized SVFit

1405 FastMTT [62] is a further simplification to the matrix element method of Classic
1406 SVFit which has comparable performance but is about 100 times faster. FastMTT
1407 drops the matrix element component of the computation without significant impact
1408 on the final mass resolution, and simplifies the computation of the transfer functions.
1409 The opening angle of the τ decay products with respect to the initial τ momenta ap-
1410 proaches 0 for τ with high $\gamma = E_\tau/m_\tau$, with typical τ decays from the Z boson decays
1411 already satisfying this condition. In this collinear approximation, the dimensionality
1412 of the transfer function can be reduced in the computation of FastMTT, while still
1413 yielding similar results to Classic SVFit [62].

1414 5.3 Corrections applied to simulation

1415 Corrections are applied to simulated samples to account for known effects in the event
1416 modeling and reconstruction and data-taking, and are intended to bring simulations
1417 in closer agreement with data. Corrections fall into two broad categories: *energy*
1418 *scale corrections* applied to physics objects, and *event-level corrections*. Energy scale
1419 corrections are multiplicative factors applied to the energy and transverse momentum
1420 p_T of simulated objects (e.g. leptons or jets), and bring the average reconstructed en-
1421 ergies of simulated particles into better agreement with those of objects reconstructed
1422 from data. Event-level corrections are applied as a per-event multiplicative weight,
1423 and account for effects such as mis-modeling in simulations of the underlying physics
1424 process, or changing detector operating conditions during data-taking. Event-level
1425 corrections change the shapes of the distributions of all the physical observables.

1426 Uncertainties in scale factors and corrections are also sources of systematic errors
1427 in the analysis, detailed in Chapter 8. Systematic uncertainties in the tau, muon, and
1428 electron energy scales can shift the p_T of the leptons up or down, which can change

1429 whether events pass or fail the offline p_T thresholds for the trigger paths described in
1430 the previous section, i.e. change the number of events in the signal region.

1431 5.3.1 Tau energy scale

1432 An energy scale is applied to the transverse momentum p_T and mass of the hadronic
1433 tau τ_h in the $\mu\tau_h$ and $e\tau_h$ channels, to correct for a deviation of the average recon-
1434 structed τ_h energy from the generator-level energy of the visible τ_h decay products.
1435 These correction factors are derived centrally [51], by fitting to events in $e\tau_h$ and $\mu\tau_h$
1436 final states in Z/γ^* events separately for the h^\pm , $h^\pm\pi^0$, and $h^\pm h^\mp h^\pm$ decays. The
1437 values used are shown in Table 5.1.

1438 When applying the energy scale to the τ_h , the 4-momentum of the missing trans-
1439 verse energy (MET) is adjusted such that the total 4-momenta of the τ_h and the MET
1440 remains unchanged [63].

Tau energy scale factor				
Decay mode	2018	2017	2016 pre-VFP	2016 post-VFP
0	0.991 ± 0.008	0.986 ± 0.009	0.987 ± 0.01	0.993 ± 0.009
1	1.004 ± 0.006	0.999 ± 0.006	0.998 ± 0.006	0.991 ± 0.007
10	0.998 ± 0.007	0.999 ± 0.007	0.984 ± 0.008	1.001 ± 0.007
11	1.004 ± 0.009	0.996 ± 0.01	0.999 ± 0.011	0.997 ± 0.016

Table 5.1: Energy scales applied to genuine hadronic tau decays τ_h by data-taking year/era and decay mode, along with systematic errors.

1441 5.3.2 Muon energy scale

1442 An energy scale is applied to the p_T and mass of genuine muons from τ decays in the
1443 $e\mu$ and $\mu\tau_h$ channels [64]. The applied values are the same for MC and embedded
1444 samples and are shown in Table 5.2. Following the SM $H \rightarrow \tau\tau$ analysis, Rochester
1445 corrections are not applied, and instead prescriptions from [65] are followed.

Muon energy scale factor	
Eta range	Value for all years
$ \eta \in [0.0, 1.2)$	1.0 ± 0.004
$ \eta \in [1.2, 2.1)$	1.0 ± 0.009
$ \eta \in [2.1, 2.4)$	1.0 ± 0.027

Table 5.2: Energy scales and systematic errors applied to genuine muons. The values are the same for MC and embedded for all years [66] [65].

1446 5.3.3 Electron energy scale

1447 Corrections to the electron energy scale are applied to genuine e from τ decays, and
 1448 are binned in two dimensions by electron p_T and η for barrel vs. endcap [67]. The
 1449 scale factors are binned in p_T and η for MC samples: e.g. values for 2018 are shown
 1450 in Fig. 5.2 from [68]. For embedded samples the electron energy scale is taken as
 1451 only binned in η (Table 5.3).

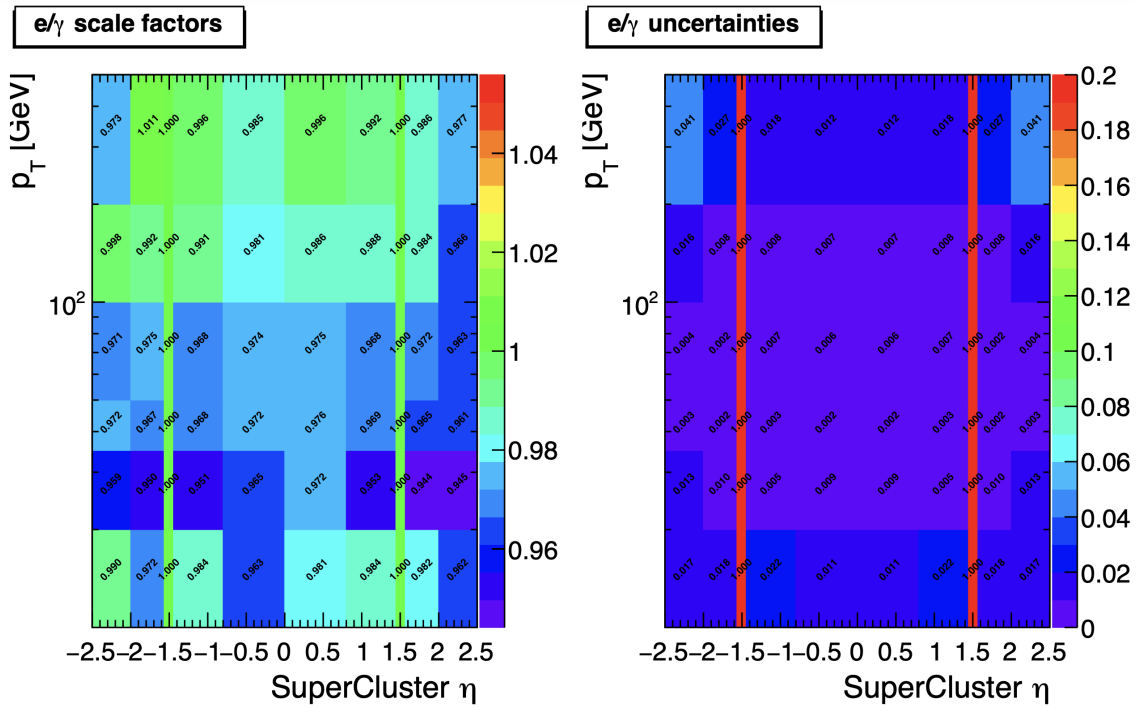


Figure 5.2: Electron/photon energy scale factors (*left*) and corresponding uncertainties (*right*) binned in the electron η and p_T , for the data-taking year 2018 [68].

Electron energy scale factor for embedded samples			
Eta range	2018	2017	2016
$ \eta \in [0.0, 1.479)$	0.973 ± 0.005	0.986 ± 0.009	0.9976 ± 0.0050
$ \eta \in [1.479, 2.4)$	0.980 ± 0.0125	0.887 ± 0.0125	0.993 ± 0.0125

Table 5.3: Energy scales and systematic errors applied to electrons in embedded samples, binned in the electron η , by data-taking year [69] [70] [71].

1452 5.3.4 τ_h identification efficiency

1453 The τ_h identification efficiency can differ in data and MC [63]. Recommended correc-
 1454 tions are provided by the Tau POG, and we use the medium DeepTau vs. jet working
 1455 point values. The identification efficiency is measured in $Z \rightarrow \tau\tau$ events in the $\mu\tau_h$
 1456 final state, and is binned in p_T due to clear p_T dependence of the DeepTau ID.

Tau ID efficiency for DeepTau Medium vs. jet WP in 2018						
p_T (GeV)	< 20	(20, 25]	(25, 30]	(30, 35]	(35, 40]	(40, 500]
Central value	0	0.945	0.946	0.916	0.921	1.005
Up value	0	1.001	0.981	0.946	0.950	1.035
Down value	0	0.888	0.981	0.883	0.893	0.953

Table 5.4: Tau ID efficiency for the DeepTau vs. jet medium working point, with central, up, and down values for 2018, binned in the tau p_T [63].

1457 5.3.5 Trigger efficiencies

1458 Scale factors are applied to correct for differences in trigger efficiencies between MC
 1459 and embedded vs. data, with values taken from tools provided by the Standard Model
 1460 $H \rightarrow \tau\tau$ working group which uses the same trigger paths [66]. In the following
 1461 sections we review relevant trigger efficiencies in data, which form the basis of the
 1462 trigger efficiency corrections applied to MC and embedded.

1463 5.3.6 Tau trigger efficiencies

1464 The efficiencies in data of the single- τ_h leg in $\mu\tau_h$, $e\tau_h$, and di- τ_h triggers is computed
 1465 centrally per using a Tag and Probe (TnP) method [72] which is outlined here. In

1466 this method, $Z \rightarrow \tau\tau \rightarrow \mu\tau_h$ are selected in data and a Drell-Yan simulated sample
 1467 ($Z \rightarrow \ell\ell, \ell = e, \mu, \tau_h$) with high purity. Cuts are applied to reject events not in this
 1468 final state, e.g. suppressing $Z \rightarrow \mu\mu$ by vetoing events with a single loose ID muon.
 1469 An isolated muon candidate (the tag) with online $p_T > 27$ GeV and $|\eta| < 2.1$ is
 1470 identified and matched to an offline μ . An offline τ_h candidate (the probe) is selected,
 1471 which is separated from the tag μ , and has $p_T > 20$ GeV and $|\eta| < 2.1$. The probe
 1472 τ_h must pass anti-muon and anti-electron discriminators to avoid fakes from muons
 1473 and electrons, and must pass the medium MVA tau isolation to suppress fakes from
 1474 QCD jets. The trigger efficiency in the TnP method is calculated as

$$\text{Efficiency} = \frac{\text{Number of events passing the TnP selection with fires the HLT path}}{\text{Number of events passing the TnP selection}} \quad (5.4)$$

1475 The efficiencies for the hadronic tau legs in the relevant channels of this analyses
 1476 ($\mu\tau_h$ and $e\tau_h$) as a function of the offline tau p_T and η , are shown for data taken in
 1477 2016, 2017, and 2018 in Figures 5.3a and 5.3b [72] [73]. In both figures, the different
 1478 HLT thresholds and differences in the L1 seed result in higher efficiencies in 2016 and
 1479 differences in shapes of the 2016 efficiencies compared to 2017 and 2018. The low
 1480 pileup in 2016 also leads to higher efficiencies in that year.

1481 **5.3.7 Single muon trigger efficiencies**

1482 The efficiencies for the single isolated muon trigger with $p_T > 24$ GeV used in this
 1483 analysis, is shown for the data-taking year 2018 in Fig. 5.4a as a function of the muon
 1484 p_T and as a function of the muon $|\eta|$ in Fig. 5.4b from [74]. The data is split with
 1485 respect to a HLT muon reconstruction update that was deployed on 15/05/2018. A
 1486 small asymmetry in efficiencies between negative and positive η in Fig. 5.4b is due to
 1487 disabled muon chambers (CSCs). The efficiencies shown are estimated using a Tag
 1488 and Probe method using $Z \rightarrow \mu\mu$ events, with the tag being an offline muon with

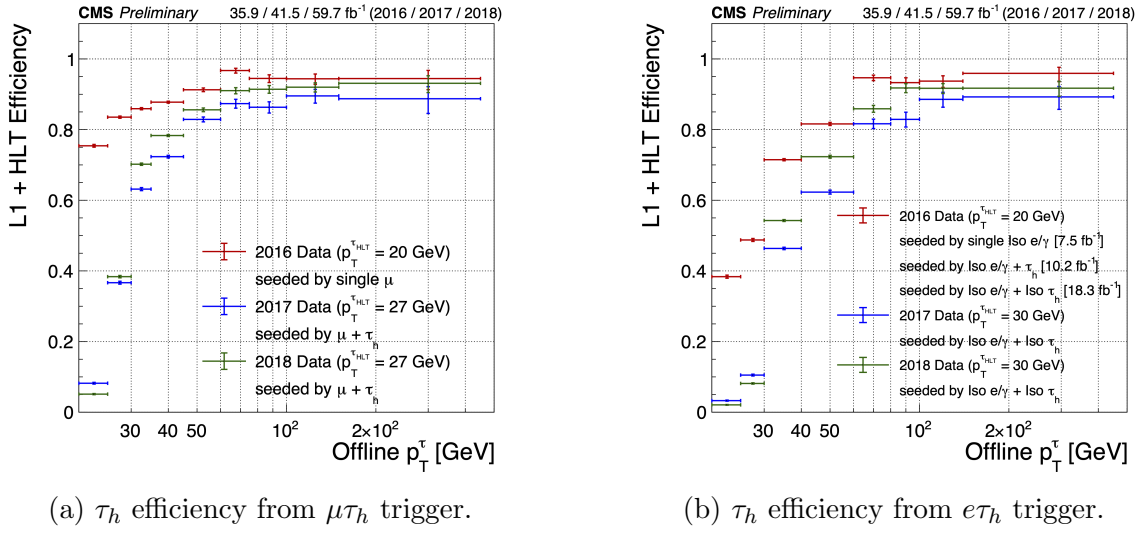


Figure 5.3: Hadronic tau leg efficiency of the cross-triggers for $\mu\tau_h$ (*left*) and $e\tau_h$ (*right*) triggers as a function of offline tau p_T for the years 2016 (red), 2017 (blue) and 2018 (green), from [73]. HLT p_T thresholds and L1 seeds are indicated in the legends.

1489 $p_T > 29$ GeV and $|\eta| < 2.4$ passing a tight ID criteria, and the probe is an online (L1)
1490 trigger object with $\Delta R < 0.3$ and passing tight ID and Particle Flow based isolation
1491 requirements with $p_T > 26$ GeV.

1492 5.3.8 Single electron trigger efficiencies

1493 The efficiencies in data, and the ratio between data and MC, of the single electron
1494 HLT trigger with p_T threshold 32 GeV used in this analysis are shown for 2018, as
1495 a function of the electron p_T in Fig. 5.5a and of the electron $|\eta|$ in Fig. 5.5b, from
1496 [75]. In the Tag and Probe method used for the 2018 dataset, the tag is an offline
1497 reconstructed electron with $|\eta| \leq 2.1$ and not in the barrel and endcap overlap region,
1498 with $p_T > 35$ GeV with tight isolation and shower shape requirements, firing the tag
1499 trigger. The probe is an offline reconstructed electron with $|\eta| \leq 2.5$ with $E_T^{\text{ECAL}} > 5$
1500 GeV with no extra identification criteria [75].

1501 The disagreement between data and MC, particularly at low transverse momen-
1502 tum, is in part due to detector effects that are difficult to simulate, such as crystal

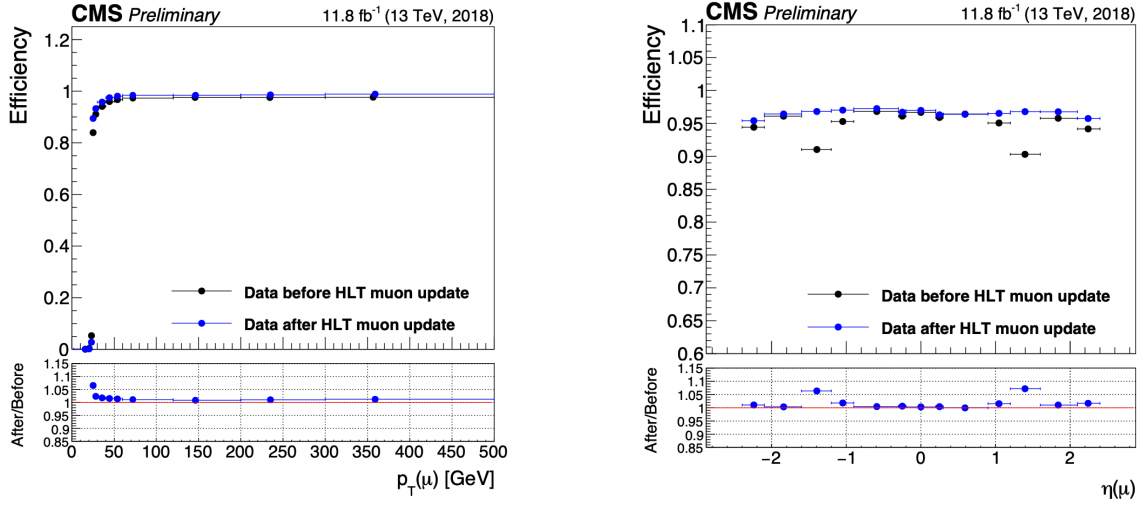
(a) Muon efficiency vs p_T for SingleMuon.(b) Muon efficiency vs $|\eta|$ for SingleMuon.

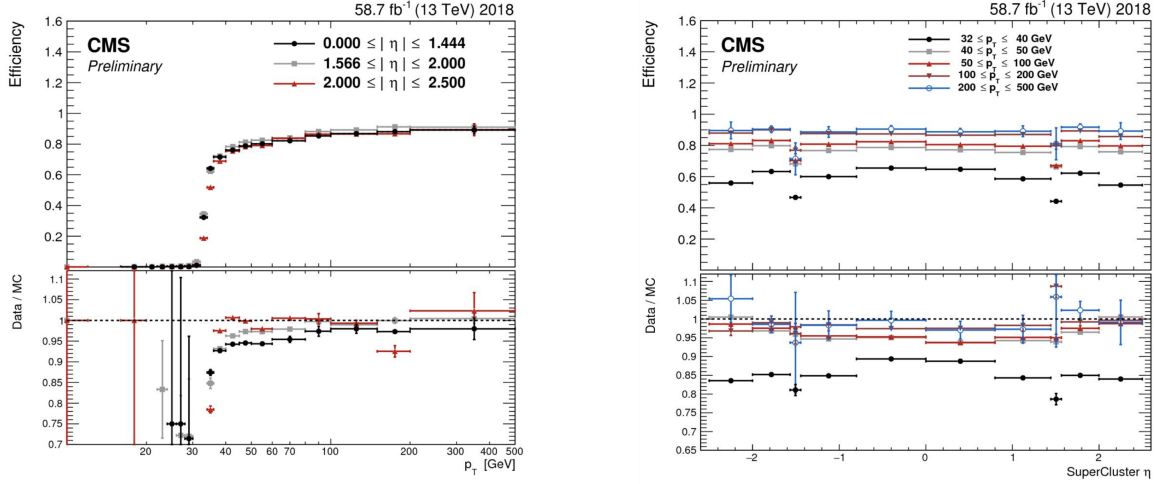
Figure 5.4: Trigger efficiencies in data (*top panels*) and ratio of efficiencies after/before a HLT muon reconstruction update (*bottom panels*) for the muon in the isolated single muon trigger with threshold $p_T > 24$ GeV in the data-taking year 2018, as functions of the muon p_T (*left*) and muon $|\eta|$ (*right*). Only statistical errors are shown [74].

1503 transparency losses in the ECAL and the evolution of dead regions in the pixel tracker
 1504 [75].

1505 5.3.9 $e\mu$ cross-trigger efficiencies

1506 The efficiencies of the electron and muons for the cross-trigger with leading muon
 1507 used in the $e\mu$ channel are shown for data in 2016, 2017, and 2018 in Figures 5.6a and
 1508 5.6b [76]. These efficiencies were measured centrally using a Tag and Probe in events
 1509 with Z to dileptons with the same flavor and opposite charge, where the tags are an
 1510 isolated muon or electron, and the probe (offline) candidate is required to satisfy the
 1511 same lepton selection as that of the tag candidate, be matched within $\Delta R < 0.1$ with
 1512 a corresponding online trigger object, and also to pass the cross-trigger. The trigger
 1513 efficiency is then:

$$\text{Efficiency} = \frac{\text{Events passing lepton pair selections and probe passing trigger}}{\text{Events passing lepton pair selections}} \quad (5.5)$$



(a) Electron efficiency vs p_T for single electron.

(b) Electron efficiency vs $|\eta|$ for single electron.

Figure 5.5: Trigger efficiencies in data, and the data/MC ratio for the electron in the single electron trigger with threshold $p_T > 32$ GeV in the data-taking year 2018, as functions of the electron p_T (left) and electron $|\eta|$ (right) [75]. In the plot vs. p_T , the region $1.442 \leq |\eta| \leq 1.566$ is not included as it corresponds to the transition between barrel and endcap parts of the ECAL.

1514 5.3.10 Electrons and muons faking τ_h : energy scales

1515 Energy scales for electrons misidentified as hadronic tau decays (e faking τ_h) are
 1516 provided by the Tau POG, and were measured in the $e\tau_h$ channel with the visible
 1517 invariant mass of the electron and hadronic tau system [66]. This energy scale is
 1518 applied for τ_h with $p_T > 20$ GeV regardless of which DeepTau vs. electron working
 1519 point was used. Values for 2018 are shown in Table 5.5.

Electrons faking τ_h energy scale factor in 2018	
Reconstructed decay mode of the fake τ_h	Central value and (up, down) shifts
0	1.01362 (+0.00474, -0.00904)
1	1.01945 (+0.01598, -0.01226)
10	0.96903 (+0.0125, -0.03404)
11	0.985 (+0.04309, -0.05499)

Table 5.5: Energy scales and up/down systematic uncertainties applied to electrons misidentified as hadronic taus for 2018, binned in decay mode of the fake τ_h [66].

1520 No nominal energy scale is applied for muons mis-reconstructed as τ_h , and the

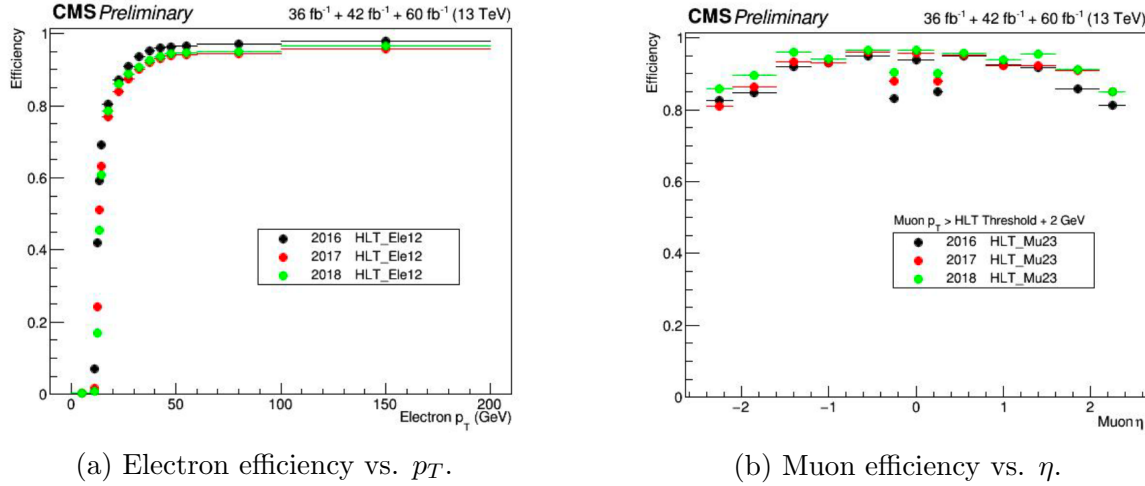


Figure 5.6: Efficiencies of the electron leg vs. p_T (*left*) and the muon leg vs. η (*right*), for the HLT path with online thresholds of 12 GeV for the electron and 23 GeV for the muon, for the data-taking years 2016 (*black*), 2017 (*red*), and 2018 (*green*) [76].

1521 uncertainty is treated as $\pm 1\%$ and uncorrelated in the reconstructed decay mode
1522 [66].

1523 5.3.11 Electrons and muons faking τ_h : misidentification effi- 1524 ciencies

1525 Corrections on identification efficiencies are applied to genuine electrons and muons
1526 misidentified as τ to account for differences in data and MC.

1527 The specific values depend on the vs. electron and vs. muon discriminator working
1528 points used. For misidentified $\mu \rightarrow \tau_h$, the scale factors are split into different $|\eta|$
1529 regions, determined by the CMS muon and tracker detector geometries, as shown in
1530 Table 5.6 for 2018 [63].

1531 For misidentified $e \rightarrow \tau_h$, the scale factors are split into barrel and endcap regions,
1532 dictated by the ECAL detector geometry, as shown in Table 5.7 for 2018.

Tau ID efficiency for DeepTau vs. muon WPs in 2018		
$ \eta $	Tight working point	VLoose working point
(0.0, 0.2)	0.767 ± 0.127	0.954 ± 0.069
(0.2, 0.6)	1.255 ± 0.258	1.009 ± 0.098
(0.6, 1.0)	0.902 ± 0.203	1.029 ± 0.075
(1.0, 1.45)	0.833 ± 0.415	0.928 ± 0.145
(1.45, 2.0)	4.436 ± 0.814	5.000 ± 0.377
(2.0, 2.53)	1.000 ± 0.000	1.000 ± 0.000

Table 5.6: Tau mis-identification efficiency for the DeepTau Tight and Very Loose (VLoose) working points vs. muons in 2018, binned in the muon $|\eta|$ [63].

Tau ID efficiency for DeepTau vs. electron WPs in 2018		
$ \eta $	Tight working point	VLoose working point
(0.0, 0.73)	1.47 ± 0.27	0.95 ± 0.07
(0.73, 1.509)	1.509 ± 0.0	1.00 ± 0.0
(1.509, 1.929)	1.929 ± 0.2	0.86 ± 0.1
(1.929, 2.683)	2.683 ± 0.9	2.68 ± 0.0

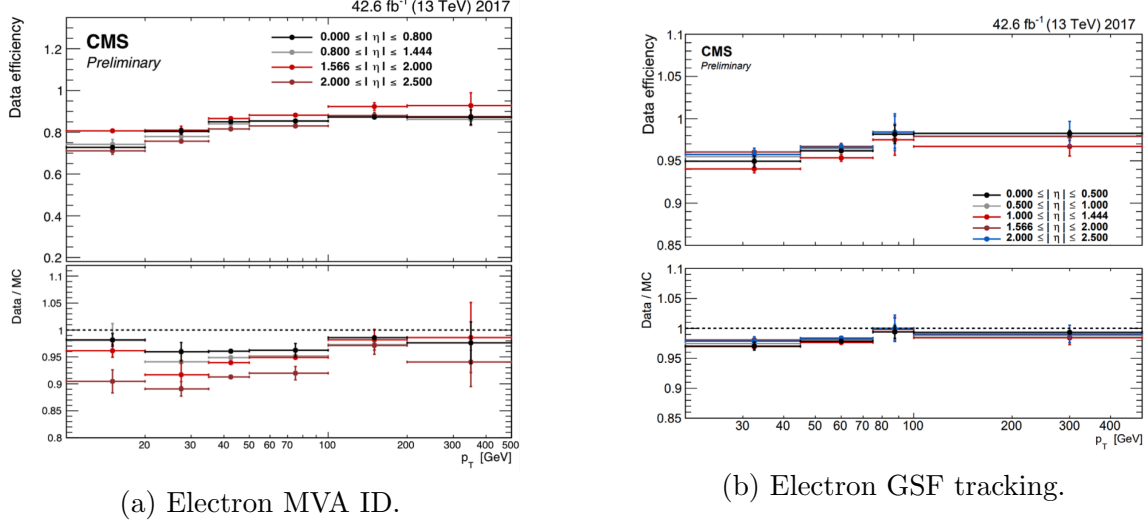
Table 5.7: Tau mis-identification efficiency for the DeepTau Tight and Very Loose (VLoose) working points vs. electrons in 2018, binned in the electron $|\eta|$ [63].

5.3.12 Electron ID and tracking efficiency

1533 Scale factors are applied to MC to correct for differences between MC and data in
 1534 the performance of electron identification (ID) and tracking.

1535 Electron and photon identification, as discussed earlier, use variables with good
 1536 signal vs. background discrimination power such as lateral shower shape and ratio
 1537 of energy deposited in the HCAL to energy deposited in the ECAL at the position
 1538 of the electron. The cut-based electron identification efficiencies in data and ratio of
 1539 efficiencies in data to MC are shown in Fig. 5.7a for the multivariate analysis (MVA)
 1540 identification working point.

1541 The tracking efficiencies in data and the data/MC ratio are shown in Fig. 5.7b
 1542 for the Gaussian-sum filter (GSF) tracking [77].



(a) Electron MVA ID.

(b) Electron GSF tracking.

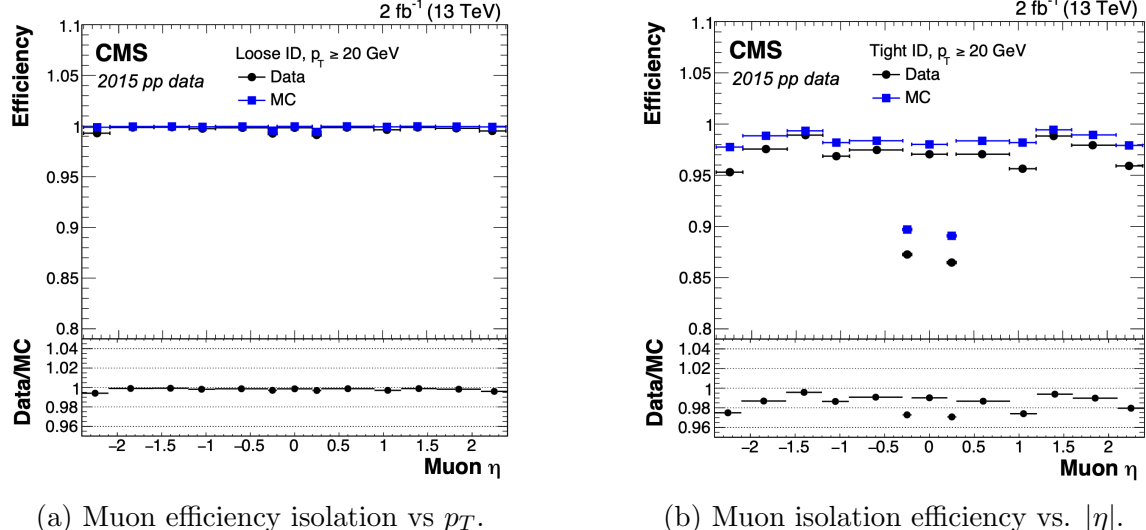
Figure 5.7: Efficiencies in data (*top panels*) and the ratio of efficiencies in data/MC (*bottom panels*), for the electron multivariate analysis (MVA) identification (*left*) and for the Gaussian-sum filter (GSF) tracking (*right*) [77]. Error bars represent statistical and systematic uncertainties.

5.3.13 Muon ID, isolation, and tracking efficiencies

Scale factors are applied to MC to correct for differences between MC and data in the performance of muon identification, isolation, and tracking, as detailed below.

The efficiencies for muon identification measured in 2015 data and MC simulation are shown in Figures 5.8a and 5.8b for the loose ID and tight ID respectively [78]. The loose ID is chosen such that efficiency exceeds 99% over the full η range, and the data and simulation agree to within 1%. The tight ID is chosen such that efficiency varies between 95% and 99% as a function of η , and the data and simulation agree to within 1-3%. The muon identification working point used in this analysis is the medium ID, which has an efficiency of 98% for all η and an agreement within 1-2% [78].

The efficiencies in data for the muon isolation, as measured in Level-3 muons (muons in one of the final stages of reconstruction in the HLT), as a function of the muon p_T and $|\eta|$ are shown in Figures 5.9a and 5.9b [78]. The HLT muon reconstruction consists of two steps: Level-2 (L2), where the muon is reconstructed in the muon



(a) Muon efficiency isolation vs p_T .

(b) Muon isolation efficiency vs. $|\eta|$.

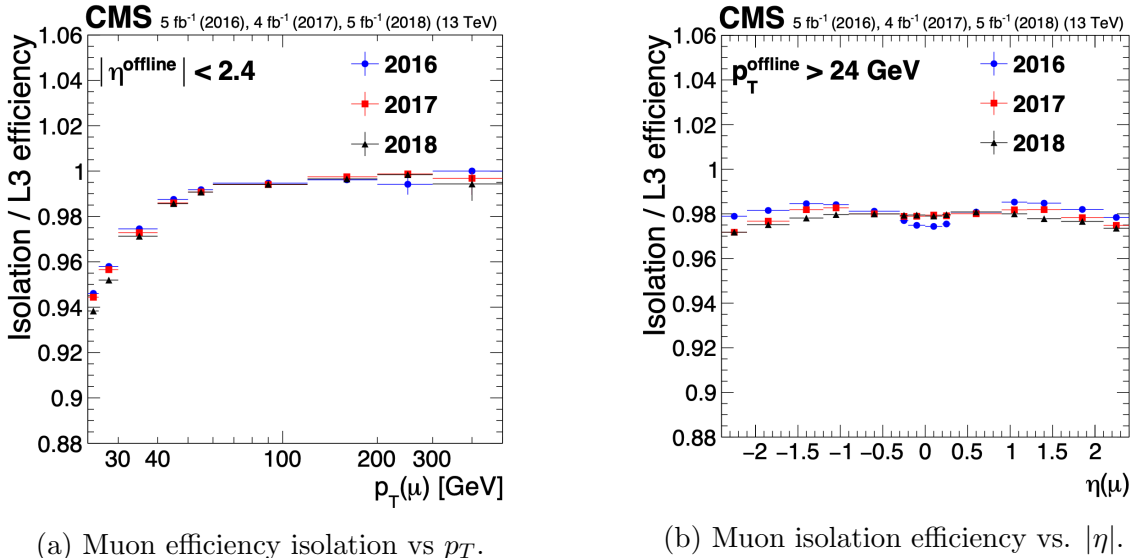
Figure 5.8: Muon identification efficiencies in 2015 data and MC as a function of the muon p_T for the loose ID (*left*) and tight ID (*right*) working points [78].

subdetectors only, and Level-3 (L3) which is a global fit of tracker and muon hits (i.e. the global muon reconstruction as described in Section 5.1.2) [79].

The muon tracking efficiencies as a function of $|\eta|$ for standalone muons (i.e. tracks from only the muon system, i.e. DT, CSC, and RPC, as discussed in Section 5.1.2), is shown for data and simulated Drell-Yan samples in Fig. 5.10 [80].

5.3.14 Recoil corrections

In proton-proton collisions, W and Z bosons are predominantly produced through quark-antiquark annihilation. Higher-order processes can induce radiated quarks or gluons that recoil against the boson, imparting a non-zero transverse momentum to the boson [81]. Recoil corrections accounting for this effect are applied to samples with W+jets, Z+jets, and Higgs bosons [66]. The corrections are performed on the vectorial difference between the measured missing transverse momentum and the total transverse momentum of neutrinos originating from the decay of the W, Z, or Higgs boson. This vector is projected onto the axes parallel and orthogonal to the boson p_T . This vector, and the resulting correction to use, is measured in $Z \rightarrow \mu\mu$ events,



(a) Muon efficiency isolation vs p_T .

(b) Muon isolation efficiency vs. $|\eta|$.

Figure 5.9: Muon isolation efficiencies in Run-2 data with respect to Level-3 muons (one of the final stages of HLT muon reconstruction) as a function of the muon p_T (*left*) and $|\eta|$ (*right*) [78].

since these events have leptonic recoil that do not contain neutrinos, allowing the 4-vector of the Z boson to be measured precisely. The corrections are binned in generator-level p_T of the parent boson and also the number of jets in the event.

5.3.15 Drell-Yan corrections

The Z boson transverse momentum distribution disagrees between leading-order (LO) simulations and data in a $Z \rightarrow \mu\mu$ control region with at least one b-tag jet [82]. Per-event weights derived by the 2016 data-only version of this analysis [82] are applied to $Z \rightarrow \tau\tau/\ell\ell$ events, as a function of the generator-level Z boson p_T to provide better matching of MC to data.

5.3.16 Pileup reweighting

Reweighting is performed to rescale MC events to account for differences between MC and data, in the distribution of the pileup (number of additional proton-proton interactions per bunch crossing). A tool for calculating the pileup reweighting for the

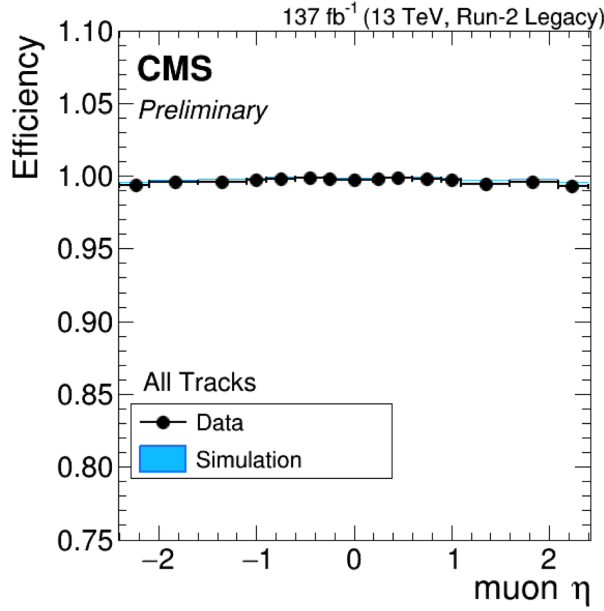


Figure 5.10: Muon tracking efficiencies as a function of $|\eta|$ for standalone muons in Run-2 data (*black*) and Drell-Yan MC simulation (*blue*) [80]. All Tracks refers to tracks which exploit the presence of muon candidates in the muon system to seed the track reconstruction in the inner tracker, in contrast to tracks that use tracker-only hits for seeding. Uncertainties shown are statistical.

1587 MC samples used is provided centrally by the Luminosity POG [83].

1588 5.3.17 Pre-firing corrections

1589 In 2016 and 2017 data-taking, a gradual timing shift of ECAL was not properly
1590 propagated to L1 trigger primitives (TPs), resulting in a large fraction of high η
1591 TPs being incorrectly associated with the previous bunch crossing. L1 trigger rules
1592 prevent two consecutive bunch crossings from firing, causing events to be rejected if
1593 significant ECAL energy was deposited in $2.0 < |\eta| < 3.0$. To account for this issue,
1594 MC simulations for 2016 and 2017 are corrected using an event-dependent weight.
1595 Embedded samples are not corrected [48].

1596 **5.3.18 Top p_T spectrum reweighting**

1597 In Run-1 and Run-2 it was observed that the p_T spectra of top quarks in $t\bar{t}$ data
1598 was significantly softer than those predicted by MC simulations [84]. Possible sources
1599 of this discrepancy are higher order QCD and/or electroweak corrections, and non-
1600 resonant production of $t\bar{t}$ -like final states. To account for this, corrections derived
1601 from Run-2 data by the Top Physics Analysis Group (PAG) are applied to the p_T
1602 of the top and anti-top quarks in MC simulations, computed as a function of their
1603 generator-level p_T [84].

1604 **5.3.19 B-tagging efficiency**

1605 In order to predict correct b-tagging discriminant distributions and event yields in
1606 data, the weight of selected MC events is reweighed according to recommendations by
1607 the BTV POG [85]. The reweighting depends on the jet p_T , η , and the b-tagging dis-
1608 criminant. In this method, there is no migration of events from one b-tag multiplicity
1609 bin to another.

1610 **5.3.20 Jet energy resolution and jet energy smearing**

1611 Calibration of jet energies, i.e. ensuring that the energy and momentum of the recon-
1612 structed jet matches that of the quark/gluon-initiated jet, is a challenging task due
1613 to time-dependent changes in the detector response and calibration and high pileup
1614 [86] [87]. Jet calibration is done via jet energy corrections (JECs) applied to the p_T
1615 of jets in MC samples, accounting successively for the effects of pileup, uniformity of
1616 the detector response, and residual data-simulation jet energy scale differences [88].
1617 Typical jet energy resolutions reported at $\sqrt{s} = 8$ TeV in the central rapidities are
1618 15-20% at 30 GeV and about 10% at 100 GeV [86]. Jet energy corrections are also
1619 propagated to the missing transverse energy.

1620 Measurements show that the jet energy resolution (JER) in data is worse than
1621 in simulation, and so the jets in MC need to be smeared to describe the data. JER
1622 corrections are applied after JEC on MC simulations, and adjust the width of the p_T
1623 distribution based on pileup, jet size, and jet flavor [89]. Tools for applying JEC and
1624 JER are provided centrally by the JER Corrections group.

1625 Chapter 6

1626 Event selection

1627 6.1 General procedure for all channels

1628 For the search for $h \rightarrow aa \rightarrow bb\tau\tau$, three final states of the $\tau\tau$ system are considered:
1629 $\mu\tau_h$, $e\tau_h$, and $e\mu$. The $\tau_h\tau_h$ final state is not considered because signal events in the
1630 $\tau_h\tau_h$ channel would typically produce hadronic taus with momenta below data-taking
1631 trigger thresholds.

1632 In all three final states, events are required to have at least one b-tag jet passing the
1633 medium working point of the DeepFlavour tagger, with $p_T > 20$ GeV, and $|\eta| < 2.4$.
1634 A second b-tag jet is not required because such a requirement would reduce signal
1635 acceptance by 80% compared to only requiring one b-tag jet.

1636 Events in MC samples are sorted into one of the three $\tau\tau$ channels if they pass the
1637 following trigger requirements and requirements on the offline reconstructed objects
1638 in the event, first checking the HLT paths for the $\mu\tau_h$ channel, then $e\tau_h$, and finally
1639 $e\mu$. The two leading leptons (e.g. muon and hadronic tau for the $\mu\tau_h$ channel) that
1640 were determined to have originated from the $\tau\tau$ decay, are called the $\tau\tau$ “legs” and
1641 are respectively subscripted 1 and 2 in this work. For events in data and embedded
1642 samples, the HLT paths requirements for the corresponding channel are checked.

1643 After sorting events by HLT paths and identifying the leading tau legs in the offline
 1644 reconstructed objects, the p_T of the offline objects is checked against the online trigger
 1645 thresholds. Trigger matching is also performed, which checks the correspondence
 1646 between each offline reconstructed object used in the analysis (e.g. a muon), and a
 1647 trigger object in the HLT (e.g. a HLT muon). An offline object is considered to be
 1648 matched, if it corresponds to a trigger object of the same object type, with $\Delta R < 0.5$.
 1649 This matched trigger object is also required to pass the filter(s) of the HLT trigger.
 1650 The trigger thresholds used for the $bb\tau\tau$ final state (the focus of this work) and the
 1651 $bb\mu\mu$ final state are summarized in Table 6.1 and detailed in the following sections.

Year	Single/dilepton trigger p_T	$bb\mu\mu$		$bb\tau\tau$			
		μ	$e\mu$	$e\tau_h$	$\mu\tau_h$	e	μ
2016	Single lepton	24	—	25	—	22	—
	p_T -leading lepton	17	23	23	—	—	20
	p_T -subleading lepton	8	12	8	—	19	—
2017	Single lepton	24	—	27, 32	—	24, 27	—
	p_T -leading lepton	17	23	23	—	30	—
	p_T -subleading lepton	8	12	8	24	—	20
2018	Single lepton	24	—	32, 35	—	24, 27	—
	p_T -leading lepton	17	23	23	—	30	—
	p_T subleading lepton	8	12	8	24	—	20

Table 6.1: Trigger thresholds used for the leptons in the $bb\mu\mu$ analysis and the $bb\tau\tau$ analysis (the focus of this work). The thresholds for the three $bb\tau\tau$ channels ($e\mu$, $e\tau_h$, and $\mu\tau_h$) are listed separately, with some channels and years taking the logical OR of two triggers with different thresholds.

1652 Further cuts are made on the offline objects in each channel to obtain the signal
 1653 region, or other data regions used to perform data-driven background estimations.

1654 6.2 Event selection in the $\mu\tau_h$ channel

1655 In all three years, a single muon trigger is used if the muon has sufficiently high p_T ,
 1656 otherwise a dilepton $\mu\tau_h$ cross-trigger is used (Tables 6.2, 6.3, and 6.4). For data

1657 taken in 2017-2018 (2016), the logical OR of the single muon triggers with online p_T
1658 thresholds 24 and 27 (23) GeV is used, with the corresponding offline muon required
1659 to have with p_T 1 GeV above the online threshold. For data taken in 2017-2018
1660 (2016), a dilepton $\mu + \tau_h$ cross-trigger with p_T thresholds of 20 (19) and 27 (20) GeV
1661 for the muon and tau respectively, is used. The τ_h is required to have $|\eta| < 2.3$ if the
1662 single trigger is fired, $|\eta| < 2.1$.

1663 The muon and τ_h are required to have opposite charge and be separated by $\Delta R >$
1664 0.4. The muon is required to have $|\eta| < 2.4$, and the τ_h is required to have $|\eta| < 2.3$
1665 unless a cross-trigger is required, in which case we require $|\eta| < 2.1$ as discussed
1666 above.

1667 The muon is required to pass the medium identification (ID) working point [90],
1668 which is defined by the Muon POG as a loose muon (i.e. a Particle Flow muon that is
1669 either a global or a tracker muon - see Section 5.1.2) with additional requirements on
1670 track quality and muon quality. This identification criteria is designed to be highly
1671 efficiently for prompt muons and for muons from heavy quark decays. In addition to
1672 the ID, for prompt muons it is recommended to apply cuts on the impact parameter
1673 [90]: we apply $|\Delta(z)| < 0.2$ and $|\Delta(xy)| < 0.045$.

1674 In addition, a cut is applied on the muon relative isolation (defined in Section
1675 5.1.2), to be less than 0.15 in a cone size of $\Delta R = 0.4$, which corresponds to the
1676 Tight Particle Flow isolation requirement [90].

1677 The τ_h is required to pass a cut on its impact parameter of $|\Delta(z)| < 0.2$. The τ_h
1678 is also required to pass the VLoose (Very Loose) DeepTau working point vs. elec-
1679 tron, the Tight DeepTau working point vs. muons, and the VVVLoose and Medium
1680 DeepTau working point vs. jets. Events with taus reconstructed in two of the decay
1681 modes (labeled 5 and 6) are rejected, since these decay modes are meant to recover
1682 3-prong taus, but are only recommended for use in analyses where the benefits in
1683 final significance outweigh the resulting increase in background [63].

1684 For the estimation of the background from jets faking τ_h , which is described in Sec-
1685 tion 7.7, anti-isolated events are selected, by requiring events to pass all the selections
1686 described above, except failing the Medium DeepTau working point vs. jets.

1687 6.3 Event selection in the $e\tau_h$ channel

1688 The HLT trigger paths for the $e\tau_h$ channel are summarized in Tables 6.2, 6.3, and
1689 6.4. Similarly to the $\mu\tau_h$ channel, a single electron trigger is used if the electron has
1690 sufficiently high p_T in 2018 and 2017. For data taken in 2018 (2017), the OR of the
1691 single electron triggers with online p_T thresholds at 32 and 35 (27 and 32) GeV are
1692 used, with the corresponding offline electrons required to have p_T greater than 33
1693 (28) GeV. A $e + \tau_h$ cross-trigger is used for electrons with lower offline p_T between
1694 25 and 33 GeV (25 and 28 GeV). For the 2016 dataset, there is no cross trigger but
1695 only a single electron trigger with online p_T threshold at 25 GeV, which is used if the
1696 offline electron has p_T greater than 26 GeV.

1697 The electron and τ_h are required to have opposite charge and be separated by
1698 $\Delta R > 0.4$. The electron is required to be within $|\eta| < 2.3$ when no cross trigger is
1699 used, and $|\eta| < 2.1$ when the cross trigger is fired. The τ_h is required to have $|\eta| < 2.3$
1700 if no cross trigger is fired, and have $|\eta| < 2.1$ if the cross trigger is fired.

1701 The electron is required to have a relative isolation (same definition as in Section
1702 5.1.2) of less than 0.1 in a cone size of $\Delta R = 0.3$, which is the standard recommended
1703 cone size giving minimal pileup dependence and reduced probability of other objects
1704 overlapping with the cone. The isolation quantity used includes an “effective area”
1705 (EA) correction to remove the effect of pileup in the barrel and endcap parts of the
1706 detector [91].

1707 The electron is also required to pass cuts on its impact parameter of $|\Delta(z)| < 0.2$
1708 and $|\Delta(xy)| < 0.045$. It is also required to pass the non-isolated MVA working point

1709 corresponding to 90% efficiency. The electron's number of missing hits, which are
1710 gaps in its trajectory through the inner tracker [91], must be less than or equal to
1711 1. The electron must pass a conversion veto, which rejects electrons coming from
1712 photon conversions in the tracker, which should instead be reconstructed as part of
1713 the photon [91].

1714 The impact parameter cut for the τ_h is $|\Delta(z)| < 0.2$. In contrast to the $\mu\tau_h$ event
1715 selection, the vs. electron and vs. muon DeepTau working points are flipped, to
1716 reject muons faking the τ_h leg. The τ_h is required to pass the Tight DeepTau working
1717 point vs. electrons, the VLoose DeepTau working point vs. muons, and the Medium
1718 DeepTau working point vs. jets.

1719 As in the $\mu\tau_h$ channel, for the estimation of the background from jets faking τ_h ,
1720 which is described in Section 7.7, anti-isolated events are selected, by requiring events
1721 to pass all the selections described above, except failing the Medium DeepTau working
1722 point vs. jets.

1723 6.4 Event selection in the $e\mu$ channel

1724 The HLT trigger paths for the $e\mu$ channel are summarized in Tables 6.2, 6.3, and
1725 6.4. Events are selected with the logical OR of two $e + \mu$ cross triggers, where either
1726 the electron or muon can have larger p_T : (1) leading electron, where the electron has
1727 online $p_T > 23$ GeV and muon has online $p_T > 8$ GeV, or (2) leading muon, where
1728 electron has online $p_T > 12$ GeV and muon has online $p_T > 23$ GeV.

1729 The leading and sub-leading leptons are required to have an offline p_T greater
1730 than 1 GeV above the online threshold (i.e. $p_T > 24$ GeV). If the sub-leading lepton
1731 is the electron, the offline p_T threshold is 1 GeV above the online threshold ($p_T > 13$
1732 GeV), but if it is a muon, the offline p_T threshold is required to be at least 5 GeV
1733 greater than the online threshold (i.e. $p_T > 13$ GeV). This is because of poor data

1734 and simulation agreement for low- p_T muons with p_T between 9 GeV and 13 GeV, and
1735 the higher probability of mis-identifying jets as muons at lower p_T . With no effect on
1736 the expected limits, the offline p_T threshold for muons is raised to 13 GeV instead of
1737 9 GeV, even though it may lead to loss in signal acceptance. Both the electron and
1738 muon are required to have $|\eta| < 2.4$.

1739 The electron and muon are required to have opposite charge and be separated
1740 by $\Delta R > 0.3$ (note the decreased separation requirement compared to the other
1741 two channels). The electron is required to pass the non-isolated MVA identification
1742 working point corresponding to 90% efficiency, and to have a relative isolation less
1743 than 0.1 for a cone size of $\Delta R = 0.3$ with the EA pileup subtraction correction.
1744 The electron must have one or fewer missing hits and pass the conversion veto (both
1745 described previously in Section 6.3).

1746 The muon is required to pass the medium identification working point (described
1747 earlier in 6.2), and to have a relative isolation less than 0.15 for a cone size of $\Delta R =$
1748 0.4. The muon impact parameter is required to have $|\Delta(z)| > 0.2$ and $|\Delta(xy)| < 0.045$.

1749 For the QCD multijet background estimation described in Section 7.8, the same-
1750 sign region is selected by requiring all the above selections, except the legs are required
1751 to have the same electric charge rather than opposite.

1752 6.5 Extra lepton vetoes in all channels

1753 Events containing a third lepton (electron or muon) that is neither of the leading $\tau\tau$
1754 legs are rejected, and events with di-muons and di-electrons are vetoed, with criteria
1755 taken from the Standard Model $H \rightarrow \tau\tau$ working group [66].

1756 The event is vetoed if a third electron is found with the following properties:
1757 $p_T > 10$ GeV, $|\eta| < 2.5$, impact parameter $|\Delta(z)| < 0.2$ and $|\Delta(xy)| < 0.045$, passing
1758 non-isolation MVA identification with 90% efficiency, conversion veto, ≤ 1 missing

2016 $\mu\tau_h$ trigger paths	
Notes	HLT Path
	HLT_IsoMu22_v
	HLT_IsoMu22_eta2p1_v
	HLT_IsoTkMu22_v
	HLT_IsoTkMu22_eta2p1_v
	HLT_IsoMu19_eta2p1_LooseIsoPFTau20_v
	HLT_IsoMu19_eta2p1_LooseIsoPFTau20_SingleL1_v

2016 $e\tau_h$ trigger paths	
Notes	HLT Path
	HLT_Ele25_eta2p1_WPTight_Gsf_v

2016 $e\mu$ trigger paths	
Notes	HLT Path
runs B-F and MC	HLT_Mu23_TrkIsoVVL_Ele12_CaloIdL_TrackIdL_IsoVL_v
runs B-F and MC	HLT_Mu8_TrkIsoVVL_Ele23_CaloIdL_TrackIdL_IsoVL_v
runs G-H	HLT_Mu23_TrkIsoVVL_Ele12_CaloIdL_TrackIdL_IsoVL_DZ_v
runs G-H	HLT_Mu8_TrkIsoVVL_Ele23_CaloIdL_TrackIdL_IsoVL_DZ_v

Table 6.2: High-Level Trigger (HLT) paths used to select data and simulation events in 2016 for the three $\tau\tau$ channels.

2017 $\mu\tau_h$ trigger paths	
Notes	HLT Path
	HLT_IsoMu24_v
	HLT_IsoMu27_v
	HLT_IsoMu20_eta2p1_LooseChargedIso_PFTau27_eta2p1_CrossL1_v

2017 $e\tau_h$ trigger paths	
Notes	HLT Path
	HLT_Ele32_WPTight_Gsf_v
	HLT_Ele35_WPTight_Gsf_v
	HLT_Ele24_eta2p1_WPTight_Gsf_Loose_ChargedIsoPFTau30_eta2p1_CrossL1_v

2017 $e\mu$ trigger paths	
Notes	HLT Path
	HLT_Mu23_TrkIsoVVL_Ele12_CaloIdL_TrackIdL_IsoVL_DZ_v
	HLT_Mu8_TrkIsoVVL_Ele23_CaloIdL_TrackIdL_IsoVL_DZ_v

Table 6.3: High-Level Trigger (HLT) paths used to select data and simulation events in 2017 for the three $\tau\tau$ channels.

2018 $\mu\tau_h$ trigger paths	
Notes	HLT Path
	HLT_IsoMu24_v
	HLT_IsoMu27_v
only data run < 317509	HLT_IsoMu20_eta2p1_ (contd.)
	LooseChargedIsoPFTauHPS27_eta2p1_CrossL1_v
MC and data run \geq 317509	HLT_IsoMu20_eta2p1_ (contd.)
	LooseChargedIsoPFTauHPS27_eta2p1_TightID_CrossL1_v
2018 $e\tau_h$ trigger paths	
Notes	HLT Path
	HLT_Ele32_WPTight_Gsf_v
	HLT_Ele35_WPTight_Gsf_v
only data run < 317509	HLT_Ele24_eta2p1_WPTight_Gsf_ (contd.)
	LooseChargedIsoPFTauHPS30_eta2p1_CrossL1_v
MC and data run \geq 317509	HLT_Ele24_eta2p1_WPTight_Gsf_ (contd.)
	LooseChargedIsoPFTauHPS30_eta2p1_TightID_CrossL1_v
2018 $e\mu$ trigger paths	
Notes	HLT Path
	HLT_Mu23_TrkIsoVVL_Ele12_CaloIdL_TrackIdL_IsoVL_DZ_v
	HLT_Mu8_TrkIsoVVL_Ele23_CaloIdL_TrackIdL_IsoVL_DZ_v

Table 6.4: High-Level Trigger (HLT) paths used to select data and simulation events in 2018 for the three $\tau\tau$ channels. In 2018 a HLT trigger path using the hadron plus strips (HPS) tau reconstruction algorithm became available.

1759 hits, and relative isolation < 0.3 with cone size $\Delta R = 0.3$. The event is also vetoed if
1760 a third muon is found with the following properties: $p_T > 10$ GeV, $|\eta| < 2.4$, impact
1761 parameter $|\Delta(z)| < 0.2$ and $|\Delta(xy)| < 0.045$, medium ID, and isolation < 0.3 with
1762 cone size $\Delta R = 0.4$.

1763 A di-muon veto is applied, which rejects events containing a pair of muons with
1764 opposite charge and separation of $\Delta R > 0.15$, that both pass the following selections:
1765 $p_T > 15$ GeV, $|\eta| < 2.4$, flag for global muons, flag for tracker muon, flag for Particle
1766 Flow muon, $|\Delta(z)| < 0.2$, $|\Delta(xy)| < 0.045$, and isolation < 0.3 with cone size $\Delta R =$
1767 0.4.

1768 A similar di-electron veto is applied to reject events containing a pair of electrons
1769 with opposite charge and separation of $\Delta R > 0.15$, that both pass the following
1770 selections: $p_T > 15$ GeV, $|\eta| < 2.5$, a dedicated electron ID (cut-based) for vetoing
1771 third leptons, $|\Delta(z)| < 0.2$, $|\Delta(xy)| < 0.045$, with pileup-corrected relative isolation
1772 < 0.3 with cone size $\Delta R = 0.3$.

1773 These vetoes on extra leptons also ensure orthogonality of events to analyses such
1774 as the $bb\mu\mu$ final state, whose results are combined with this $bb\tau\tau$ final state as
1775 described in Section ??.

₁₇₇₆

Chapter 7

₁₇₇₇

Background estimation

₁₇₇₈ This section describes methods used to estimate sources of background from Standard
₁₇₇₉ Model processes in the search for $h \rightarrow aa \rightarrow bb\tau\tau$. Similar background estimation
₁₇₈₀ methods are being used for the $h \rightarrow a_1a_2$ analysis. The background contributions
₁₇₈₁ directly taken from MC are described first, followed by backgrounds estimated from
₁₇₈₂ data-driven methods to produce sufficient statistics in the signal region.

₁₇₈₃

7.1 Z+jets

₁₇₈₄ A major source of background for $\tau\tau$ analyses is the Drell-Yan (DY) process (Z+jets).
₁₇₈₅ The Z boson decays to $\tau\tau/\mu\mu/ee$ with equal probability of 3.4% each, with the dom-
₁₇₈₆ inant decay modes being to hadrons (around 70%) and neutrinos (invisible) (20%)
₁₇₈₇ [26].

₁₇₈₈ The Drell-Yan contribution with genuine taus, $Z \rightarrow \tau\tau$, is estimated using embed-
₁₇₈₉ ded samples, described in Section 4.3. To avoid double-counting between embedded
₁₇₉₀ and MC samples, in all MC samples, events with legs that originated from genuine τ
₁₇₉₁ are discarded.

₁₇₉₂ The other decays of the Z, $Z \rightarrow ee$ and $Z \rightarrow \mu\mu$, are estimated from MC simulation,
₁₇₉₃ and are hereafter referred to as simply the Drell-Yan background. These MC samples

1794 are generated to leading order (LO) with different numbers of jets (jet multiplicity) in
1795 the matrix element: Z+1 jet, Z+2jets, Z+3 jets, Z+4 jets, and inclusive Z+jets. The
1796 cross-sections of the samples with ≥ 1 jets are normalized to next-to-NLO (NNLO)
1797 in QCD.

1798 For the inclusive Drell-Yan sample, two samples are used with different thresholds
1799 for the di-lepton invariant mass ($m_{\ell\ell}$) at the generator level: one with $m_{\ell\ell} > 50$ GeV
1800 and the other with $10 < m_{\ell\ell} < 50$.

1801 **7.2 W+jets**

1802 The dominant W boson decay modes are to hadrons (67.4%), $e + \nu_e$ (10.7%), $\mu + \nu_\mu$
1803 (10.6%), and $\tau + \nu_\tau$ (11.4%) [26]. The W+jets background is estimated from MC
1804 simulation. Similarly to the Z+jets, the W+jets samples are generated with different
1805 jet multiplicities in the matrix element. LO samples are used for greater statistics
1806 and are normalized to NNLO cross sections.

1807 **7.3 $t\bar{t}$ + jets**

1808 In hadron collisions, top quarks are produced singly with the weak interaction, or in
1809 pairs via the strong interaction, with interference between these leading-order pro-
1810 cesses possible in higher orders of the perturbation theory. The top quark is the
1811 heaviest fermion in the Standard Model and has a short lifetime ($\sim 10^{-25}$ s), decay-
1812 ing without hadronization into a bottom quark and a W boson [26], with the decay
1813 modes of the W boson as listed in the previous section. With two top quarks, the
1814 final states of the two resulting W bosons can be described as fully leptonic, semilep-
1815 tonic, and fully hadronic. These three final states are modeled separately with MC
1816 simulation in 2018 and 2017, while for 2016 the sample used is inclusive.

1817 7.4 Single top

1818 There are three main production modes of the single top in pp collisions [92]: the
1819 exchange of a virtual W boson (t channel), the production and decay of a virtual W
1820 boson (s channel), and the associated production of a top quark and W boson (tW ,
1821 or W-associated) channel. As the s channel process is rare and only 3% of the total
1822 production, the dominant production mode of the t -channel and the tW production
1823 are considered and modeled with MC.

1824 7.5 Diboson

1825 In pp collisions, the production of dibosons (pairs of electroweak gauge bosons, i.e.
1826 WW, WZ, and ZZ) is dominated by quark-antiquark annihilation, with a small con-
1827 tribution from gluon-gluon interaction [93]. MC is used to model the pair production
1828 and decays of VV to $2\ell 2\nu$, WZ to $2q 2\ell$ and $3\ell\nu$, and ZZ to 4ℓ and $2q 2\ell$ (q being
1829 quarks and ℓ being leptons).

1830 7.6 Standard Model Higgs

1831 MC is used to simulate backgrounds from major production modes of the Standard
1832 Model 125 GeV Higgs boson: gluon-gluon fusion (ggH), vector boson fusion (VBF),
1833 associated production with a W or Z (WH, ZH), and associated production with a
1834 top pair (ttH) (see Fig. 7.1 for leading-order diagrams). For these production modes,
1835 samples with the Higgs decaying to $\tau\tau$ or to WW are used. Samples made with
1836 higher-order diagrams for WH and ZH that include the production of a jet, with the
1837 Higgs decaying to WW, are also used.

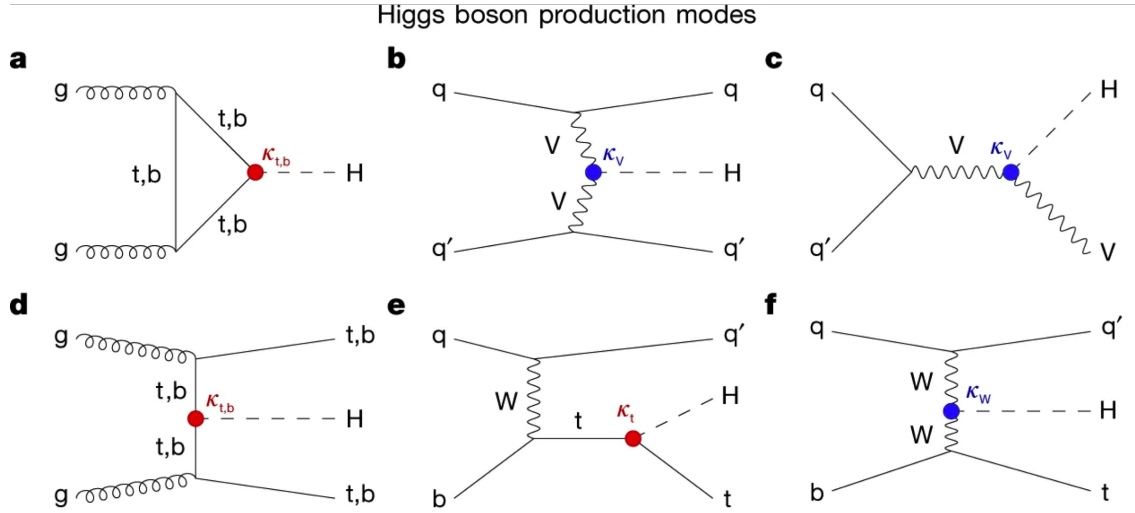


Figure 7.1: Leading-order Feynman diagrams of Higgs production from [94], in ggH (a) and vector boson fusion (VBF; b), associated production with a W or Z (V) boson (VH; c), associated production with a top or bottom quark pair (ttH or bbH); d, and associated production with a single top quark (tH; e, f).

1838 7.7 Jet faking τ_h

1839 Events with a jet mis-reconstructed as the hadronic tau leg τ_h are a major source of
 1840 background in the $\mu\tau_h$ and $e\tau_h$ channels. The main processes contributing to jet $\rightarrow \tau_h$
 1841 events are QCD multijet, W+jets, and $t\bar{t}$ production. These events are estimated
 1842 using a data-driven method adapted from past analyses [48] [82]. This background
 1843 includes contributions from W+jets, QCD multijets, and $t\bar{t}$ +jets. To estimate this
 1844 background, a sideband region is constructed, where events are required to pass all
 1845 baseline $\mu\tau_h/e\tau_h$ selection criteria, but fail the τ_h isolation criteria. The events in
 1846 this sideband region is reweighed with a factor $f/(1 - f)$, where f is the probability
 1847 for a jet to be misidentified as a τ_h . The jet $\rightarrow \tau_h$ background is the anti-isolated,
 1848 reweighed MC and embedded events subtracted from the anti-isolated, reweighted
 1849 data events.

1850 The fake factor is measured in $Z \rightarrow \mu\mu + \text{jets}$ events in data in the $\mu\mu\tau_h$ final
 1851 state, as any reconstructed τ_h in these events must originate from a jet. The two
 1852 muons are required to be isolated (< 0.15), have opposite electric charge, and have

1853 an invariant mass between 76 and 106 GeV (close to the Z mass). These events are
1854 selected with a double muon trigger, with the leading muon having offline $p_T > 20$
1855 GeV and the subleading muon $p_T > 10$ GeV. Simulated diboson (ZZ and WZ) events
1856 are subtracted to avoid contamination from events with real τ_h . The denominator of
1857 the fake rate corresponds to fake taus passing the VVVLoose working point of the
1858 discriminator vs. jets, while the numerator corresponds to those passing the Medium
1859 working point, i.e. $f = N_{\text{jet passing tight}} / N_{\text{jet passing loose}}$.

1860 f is measured as a function of the τ_h transverse momentum and is 8% - 10% in
1861 each of the data-taking years. f is derived separately for the $\mu\tau_h$ and $e\tau_h$ channels
1862 because the channels use different anti-lepton identification working points.

1863 7.8 QCD multijet background

1864 In the $e\mu$ channel, events with jets faking electrons or muons originating from QCD
1865 multijet, is estimated from data events with the same baseline selection as in the
1866 signal region, except with same-signed (SS) charged $e + \mu$, ensuring orthogonality
1867 with the signal region which requires opposite-sign (OS) $e\mu$ pairs. All same-sign MC
1868 events (both events with real and fake $e + \mu$) are subtracted from same-sign data
1869 events to remove contamination from other backgrounds. i.e. $\text{QCD}_{\text{SS}} = \text{Data}_{\text{SS}} -$
1870 MC_{SS} .

1871 Three scale factors are applied to the QCD_{SS} events to compute the QCD multijet
1872 background [82] [42]:

- 1873 • *OS-to-SS scale factor*: This scales the SS QCD to the OS region, and is mea-
1874 sured from an orthogonal region with an isolated electron and an anti-isolated
1875 muon. Only the muon is chosen to be anti-isolated because this scale factor was
1876 observed to depend more strongly on electron isolation than that of the muon.
1877 This scale factor is treated as a function of the ΔR separation of the trajectories

1878 of the electron and muon, and is measured separately for events with 0 jets, 1,
1879 jet, and greater than 1 jet.

- 1880 • *2D closure correction for the lepton p_T :* This factor accounts for subleading
1881 dependencies of the first scale factor on the p_T of the two leptons. A 2D weight
1882 is derived in a similar fashion, as a ratio of QCD_{OS} events to QCD_{SS} events,
1883 but parameterized by both electron and muon p_T , where the SS events have the
1884 previous scale factor applied.
- 1885 • *Isolation correction for the muon:* The third and final factor is an isolation
1886 correction, which is a bias correction to account for the fact that the fake
1887 factor was determined for less-isolated muons. This factor is obtained as the
1888 ratio of the OS-to-SS scale factors measured in two other control regions: (1)
1889 events where the electron is anti-isolated ($0.15 < \text{iso} < 0.5$) and the muon is
1890 isolated, and (2) events where both leptons are anti-isolated.

1891 **Chapter 8**

1892 **Systematic uncertainties**

1893 The handling of systematic uncertainties is separated into normalization uncertainties
1894 (those that affect the total yield of a variables' distribution) and shape uncertainties
1895 (those that shift the distribution of events). Normalization uncertainties are expressed
1896 as multiplicative factors, while shape uncertainties are represented as up and down
1897 shifts of a variable's distribution.

1898 Up/down shifts of shape uncertainties can change the number of background
1899 events in a distribution. For instance, hadronic taus receive corrections from the
1900 nominal tau energy scale, with the nominal, up, and down energy scales provided
1901 centrally by CMS. For the $\mu\tau_h$ channel, an event could have a τ_h with p_T just below
1902 the offline threshold of 20 GeV (for instance, 19.5 GeV), so in the nominal distribution
1903 of $m_{\tau\tau}$ (or any other variable for this channel), the event is excluded. However, when
1904 we build our distributions with the tau energy scale “up” shift, the energy of this τ_h
1905 may be scaled up to, say, 20.5 GeV, and now the event passes the offline p_T threshold
1906 for the single muon trigger, leading to the event's inclusion in the distributions made
1907 with the tau energy scale “up” shift.

1908 In evaluating the up and down shifts of a specific source of uncertainty, all other
1909 corrections and scale factors are held at their nominal values, and the full chain

1910 of object and event selection and event categorization is performed to obtain the
1911 observable distributions. Any “downstream” variables that depend on the shifted
1912 variable, e.g. the invariant di-tau mass $m_{\tau\tau}$, must be computed for the nominal case,
1913 and then re-computed separately for each up and down shift of the tau legs’ energy
1914 scale. The objective of this process is to quantify the effect of a single source of
1915 uncertainty on the resulting observable distributions.

1916 8.1 Uncertainties associated with physics objects

1917 Each scale factor and correction described in Section 5.3 has an associated uncertainty.
1918 The binning of the uncertainties follows that of the nominal scale factor value.

1919 8.1.1 Uncertainties in the lepton energy scales

1920 The uncertainties in the tau energy scales [63] are binned by the tau decay mode and
1921 are taken as shape uncertainties treated as uncorrelated across the tau decay modes
1922 and years. Same as with the application of the nominal scale factor, when applying
1923 the up or down shifts, the missing transverse energy (p_T^{miss}) of the event is adjusted
1924 so that the 4-vector sum of the tau p_T^{miss} is unchanged.

1925 The uncertainties in the muon energy scale [64] are 0.4% for $|\eta| < 1.2$, 0.9% for
1926 $1.2 < |\eta| < 2.1$, and 2.7% for $2.1 < |\eta| < 2.4$, and are treated as shape uncertainties,
1927 fully uncorrelated between embedded and MC samples.

1928 The uncertainties in the electron energy scale [67] in MC are binned in the electron
1929 $|\eta|$ and p_T , and are shown in Fig. 5.2. The uncertainties range from 0.5% to 2.2% in
1930 the barrel, and 0.3% to 4.1% in the endcap, across the p_T range. The uncertainties
1931 for the embedded sample are binned only in $|\eta|$ and are on the order of 0.5% and
1932 1.25% for the barrel and endcap [71].

1933 There are also uncertainties in the energy scales for electrons and muons misiden-

1934 tified as τ_h . The uncertainty for muons misidentified as τ_h is 1% [63]. For electrons
1935 misidentified as τ_h , the uncertainty is binned in barrel/endcap η and by 1-prong and
1936 1-prong + π_0 decays. The probability for e/μ faking a 3-prong decay mode is much
1937 lower.

1938 8.1.2 Uncertainties from other lepton corrections

1939 Uncertainties associated with the τ_h identification efficiencies are treated as shapes,
1940 uncorrelated across the seven p_T bins and years. The shape uncertainties in the
1941 embedded samples are taken as 50% correlated with those of the MC samples.

1942 The uncertainties on electron and muon identification efficiencies are taken as
1943 normalization uncertainties of 2% each, with a 50% correlation between embedded
1944 and MC samples.

1945 In the $e\tau_h$ channel, there is an additional uncertainty for the vs. jet discrimination
1946 efficiency [63], because the analysis uses a looser anti-lepton working point (VLoose
1947 WP) than the working points used in the measurement of the efficiency (namely,
1948 VLoose WP vs e, and Tight WP vs mu). For nominal $\tau_h p_T < 100$ GeV, an additional
1949 uncertainty of 3% (5%) is used in MC (embedded), and for high p_T an uncertainty of
1950 15% is used for both.

1951 The uncertainties in trigger efficiencies are taken as shapes [63]. In the $e\tau_h$ and $\mu\tau_h$
1952 channels, there are uncertainties for the single and cross lepton triggers, and in the
1953 $e\mu$ channel there is one uncertainty each for the two $e + \mu$ triggers, and one combined
1954 uncertainty since their trigger phase spaces are not mutually exclusive.

1955 8.1.3 Uncertainties from jet energy scale and resolution

1956 The jet energy scale uncertainties are taken as shape uncertainties: there are eleven
1957 in total, with seven correlated across years (labeled “Year” below) and the remainder
1958 uncorrelated across years. They affect the b-tag jet p_T and mass, and hence the

1959 missing transverse energy p_T^{miss} . The shifts are propagated through the b-tagging
1960 scale factor calculation and b-tag jet counting.

1961 The uncertainties in the jet energy correction and resolution [86] [95] are as follows:

1962 • *Absolute, AbsoluteYear*: flat absolute scale uncertainties.

1963 • *BBEC1, BBEC1Year*: for sub-detector regions, with barrel “BB” in $|\eta| < 1.3$
1964 and endcap region 1 “EC1”: $1.3 < |\eta| < 2.5$.

1965 • *EC2, EC2 year*: for sub-detector regions, with endcap region 2 “EC2” in $2.5 <$
1966 $|\eta| < 3.0$.

1967 • *HF, HF year*: for sub-detector regions, with hadron forward “HF” in $|\eta| > 3$.

1968 • *FlavorQCD*: for uncertainty in jet flavor (uds/c/b-quark and gluon) estimates
1969 based on comparing Pythia and Herwig (different MC generator) predictions.

1970 • *RelativeBal*: account for difference between log-linear fits of the two methods
1971 used to study the jet energy response: MPF (missing transverse momentum
1972 projection fraction) and p_T balance.

1973 • *RelativeSample*: account for η -dependent uncertainty due to a difference be-
1974 tween relative residuals, observed with dijet and Z+jets in Run D of 2018 data.

1975 • *JetResolution*: uncertainty in the jet energy resolution.

1976 8.1.4 Uncertainties from b-tagging scale factors

1977 The b-tagging scale factor has its own set of associated uncertainties (not to be
1978 confused with shifts in the b-tagging scale factor due to the propagation of the jet
1979 energy scale uncertainties described in the previous section 8.1.3). They are:

1980 • *hf*: contamination from heavy flavor (b+c) jets in the light flavor region.

- $hfstats1$, $hfstats2$: linear and quadratic statistical fluctuations from b-flavor jets.
 - lf : contamination from light flavor (udsg+c jets) in the heavy flavor region.
 - $lfstats1$, $lfstats2$: linear and quadratic statistical fluctuations from udsg jets.
 - $cferr$, $cferr2$: uncertainty for charm jets.
- The variations for “lf, hf, hfstats1/2, lfstats1/2” are applied to both b and udsg jets.
For c-flavor jets, only “cferr1/2” is applied.

8.1.5 Uncertainties from MET

Samples where recoil corrections were applied (Z+jets, W+jets, and Standard Model Higgs, as described in Section 5.3) have uncertainties from the response and resolution of the hadronic recoil against the leptonic system. These are each binned in jet multiplicity.

8.2 Uncertainties associated with samples used

Normalization uncertainties related to the samples used are:

- *Cross-section uncertainties*: $\sigma(t\bar{t})$: 4.2%, $\sigma(\text{diboson})$: 5%, $\sigma(\text{single top})$: 5%, $\sigma(\text{ggH})$: 3.2%, $\sigma(\text{qqH})$: 2.1%, $\sigma(\text{WH})$: 1.9%, $\sigma(\text{ZH})$: 1.3%, $\sigma(\text{ttH})$: 3.6%
- *Uncertainties in QCD renormalization scale*: QCD scale(qqH): +0.43%-0.33%, QCD scale(WH): +0.5%-0.7%, QCD scale(ttH): +5.8%-9.2%
- *Branching ratio uncertainties*: $\text{BR}(\text{H} \rightarrow \tau\tau)$: 1.8%, and $\text{BR}(\text{H} \rightarrow \text{WW})$: 1.5%
- *Normalization uncertainties*: 2% for Drell-Yan, 4\$ for embedded, 20% pre-fit for the QCD multijet background in the $e\mu$ channel, 20% pre-fit for the jet faking background.

2002 The $t\bar{t}$ process has additional acceptance uncertainties from QCD scale variation
2003 and parton shower uncertainties [96]. Parton shower uncertainties originate from
2004 the modeling of perturbative and non-perturbative QCD effects handled in parton
2005 shower MC generators. The scale variations are determined from the envelope of the
2006 6 provided shapes due to variations in the factorization scale, renormalization scale,
2007 and their combined variation [96].

2008 The Z p_T reweighing uncertainty in Drell-Yan samples is taken to be 10% of the
2009 nominal value, taken as a shape uncertainty.

2010 The fake rate uncertainties are taken as shape uncertainties. For the weight ap-
2011 plied to scale up anti-isolated events in cross-trigger regions, 20% of the nominal
2012 weight is taken as a shape uncertainty.

2013 8.3 Other uncertainties

2014 A 3.6% yield uncertainty in the signal is used to cover uncertainties in the parton
2015 distribution functions, α_s (fine structure constant), and QCD scale.

2016 Normalization uncertainties from luminosity are applied to all MC samples, di-
2017 vided into those uncorrelated across years, those correlated between 2017 and 2018,
2018 and one for 2018 [83].

2019 8.4 Pulls and impacts

2020 The top impacts and pulls computed for the combination of all channels and years is
2021 shown in Fig. 8.1. The top impacts are related to uncertainty in the signal sample and
2022 cross-section of the $t\bar{t}$ cross-section, and also the yields of the jet faking τ_h background,
2023 which is a major background in all channels and expected to be constrained due to
2024 the yield uncertainty which is taken to be 20% pre-fit.

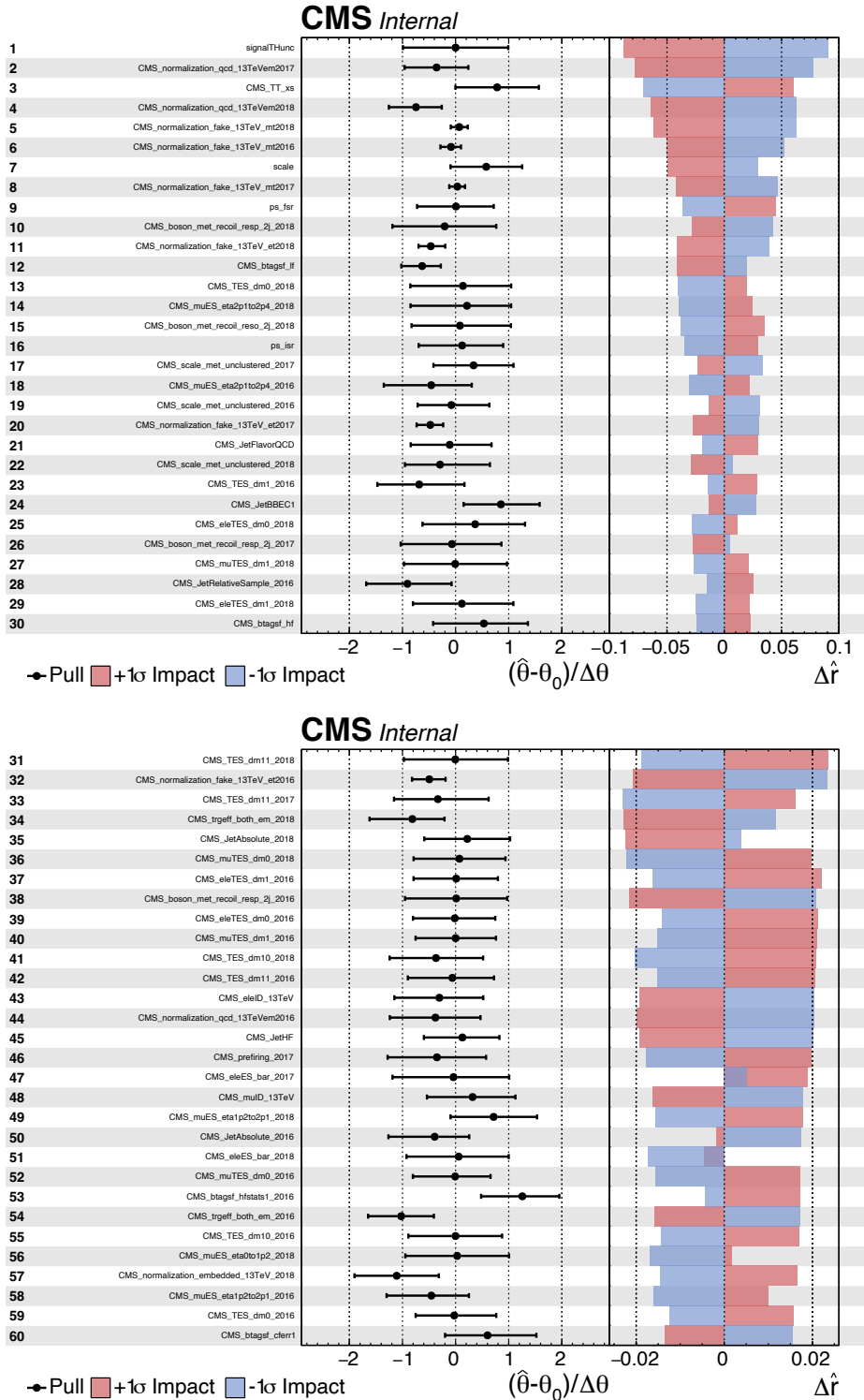


Figure 8.1: Top sixty impacts for the combination of all channels and years [41].

2025 Chapter 9

2026 Event categorization and signal 2027 extraction

2028 9.1 B-tag jet multiplicity

2029 The increased statistics of the full Run-2 dataset enables the separation of events into
2030 events with exactly 1 b-tag jet and events with greater than 1 b-tag jet. Further event
2031 categorization is performed with deep neural networks (DNNs) described below. The
2032 DNNs are used only for separating events into signal and control regions in the 1
2033 b-tag and 2 b-tag jets scenarios. The final results are extracted from the statistical
2034 fitting to the mass of the $\tau\tau$, $m_{\tau\tau}$.

2035 9.2 DNN-based event categorization

2036 A brief overview of the DNN-based event categorization is given below with a focus
2037 on the physics aspects, with full details of the machine learning training in [42] and
2038 associated documentation.

2039 **Training samples**

2040 Neural networks for event categorization are trained for each of the $\mu\tau_h$, $e\tau_h$, and $e\mu$
2041 channels, for 1 and 2 b-tag jets, giving $3 \times 2 = 6$ networks in total. In the training,
2042 the signal is taken to be all of the possible pseudoscalar mass m_a hypotheses together.
2043 The backgrounds for each DNN are taken to be a representative combination of the
2044 three major backgrounds: $Z \rightarrow \tau\tau$, $t\bar{t}$ +jets, and fake backgrounds. The proportions of
2045 each background for each channel and b-tag jet multiplicity are taken from the yields
2046 in the $m_{\tau\tau}$ distribution. For instance, in the $\mu\tau_h$ 1 b-tag jet category, the composition
2047 of the background for training is 17.4% from $Z \rightarrow \tau\tau$, 42.4% from $t\bar{t}$ +jets, and 40.2%
2048 fakes.

2049 **Input variables**

2050 The input variables capture the key differences between the signal and the back-
2051 ground:

- 2052 • Transverse momentum p_T of the electron and muon in the $e\tau_h$ and $\mu\tau_h$ channels,
2053 where the signal tends to have a softer p_T spectrum (lower energy) than the
2054 background.
- 2055 • p_T of the b-tag jet(s). The signal sample b-tag jet(s) tend to have softer p_T .
- 2056 • Invariant masses of the various objects ($\tau\tau$ legs and the b-tag jet(s)), which
2057 tend to be smaller for the signal samples.
- 2058 • The angular separation ΔR between pairs of the objects, where signal samples
2059 peak at smaller ΔR values.
- 2060 • The transverse mass between the missing transverse energy p_T^{miss} and each of

the four objects [82], defined as

$$m_T(\ell, p_T^{\text{miss}}) \equiv \sqrt{2p_T^\ell \cdot p_T^{\text{miss}}[1 - \cos(\Delta\phi)]} \quad (9.1)$$

where p_T^ℓ is the transverse momentum of the object ℓ , and $\Delta\phi$ is the difference in azimuthal angle between the object and the p_T^{miss} . Events from $t\bar{t}$ +jets and jets faking τ_h backgrounds have larger p_T^{miss} resulting in larger transverse mass values compared to the signal, which tends to have smaller p_T^{miss} that is also more aligned with the lepton legs.

- The variable D_ζ [82], defined as

$$D_\zeta \equiv p_\zeta - 0.85p_\zeta^{\text{vis}} \quad (9.2)$$

where the ζ axis is the bisector of the transverse directions of the visible τ decay products. p_ζ is the component of the p_T^{miss} along the ζ axis, and p_ζ^{vis} is the sum of the components of the lepton p_T along the same axis. This variable captures the fact that in signal the p_T^{miss} is small and approximately aligned with the $\tau\tau$. In contrast, the $Z \rightarrow \tau\tau$ background tends towards large D_ζ values because the p_T^{miss} is collinear to the $\tau\tau$, and the $t\bar{t}$ +jets events tend to have small D_ζ due to a large p_T^{miss} not aligned with the $\tau\tau$.

- For events with 2 b-tag jets, one additional variable is defined to capture the difference in the invariant mass of the bb and the $\tau\tau$:

$$\Delta m_{a_1} \equiv (m_{bb} - m_{\tau\tau})/m_{\tau\tau} \quad (9.3)$$

This variable peaks at zero for the $h \rightarrow aa \rightarrow 2b2\tau$ signal.

2078 **Categorization using the DNN score**

2079 After training, events in data, MC, and embedded are evaluated with the six DNNs
 2080 and assigned a raw score between 0 and 1 (background-like or signal-like). In order
 2081 to flatten the distribution of the score and define score thresholds for categorizing
 2082 events, the raw output scores are transformed with the function $\tilde{p}(n) = \text{arctanh}(p \times$
 2083 $\tanh(n))/n$ where n is a positive integer. The thresholds of the DNN score used for
 2084 signal/control region definition are determined using scans that optimize the signal
 2085 sensitivity and are shown in Tables 9.1 and 9.2.

1bNN $\tilde{p}(n = 1.5)$				
	SR1	SR2	SR3	CR
$\mu\tau_h$ 2018	> 0.98	$\in [0.95, 0.98]$	$\in [0.90, 0.95]$	< 0.90
$\mu\tau_h$ 2017	> 0.97	$\in [0.94, 0.97]$	$\in [0.90, 0.94]$	< 0.90
$\mu\tau_h$ 2016	> 0.97	$\in [0.94, 0.97]$	$\in [0.89, 0.94]$	< 0.89
1bNN $\tilde{p}(n = 1.5)$				
	SR1	SR2	SR3	CR
$e\tau_h$ 2018	> 0.97	$\in [0.945, 0.97]$	$\in [0.90, 0.945]$	< 0.90
$e\tau_h$ 2017	> 0.985	$\in [0.965, 0.985]$	$\in [0.93, 0.965]$	< 0.93
$e\tau_h$ 2016	> 0.985	$\in [0.965, 0.985]$	$\in [0.93, 0.965]$	< 0.93
1bNN $\tilde{p}(n = 2.5)$				
	SR1	SR2	SR3	CR
$e\mu$ 2018	> 0.99	$\in [0.95, 0.99]$	$\in [0.85, 0.95]$	< 0.85
$e\mu$ 2017	> 0.985	$\in [0.95, 0.985]$	$\in [0.85, 0.95]$	< 0.85
$e\mu$ 2016	> 0.99	$\in [0.95, 0.99]$	$\in [0.85, 0.95]$	< 0.85

Table 9.1: Event categorization based on DNN scores for events with exactly 1 b-tag jet (1bNN), for the three $\tau\tau$ channels and three eras.

2086 **9.3 Methodology for signal extraction**

2087 In this section we outline the statistics terminology and concepts underlying the
 2088 modified frequentist method CL_S used to perform signal extraction.

	2bNN $\tilde{p}(n = 1.5)$		
	SR1	SR2	CR
$\mu\tau_h$ 2018	> 0.99	$\in [0.96, 0.99]$	< 0.96
$\mu\tau_h$ 2017	> 0.98	$\in [0.94, 0.98]$	< 0.94
$\mu\tau_h$ 2016	> 0.97	$\in [0.93, 0.97]$	< 0.93
	2bNN $\tilde{p}(n = 1.5)$		
	SR1	SR2	CR
$e\tau_h$ 2018	> 0.96	NA	< 0.96
$e\tau_h$ 2017	> 0.985	NA	< 0.985
$e\tau_h$ 2016	> 0.96	NA	< 0.96
	2bNN $\tilde{p}(n = 2.5)$		
	SR1	SR2	CR
$e\mu$ 2018	> 0.98	$\in [0.94, 0.98]$	< 0.94
$e\mu$ 2017	> 0.97	$\in [0.93, 0.97]$	< 0.93
$e\mu$ 2016	> 0.98	$\in [0.94, 0.98]$	< 0.94

Table 9.2: Event categorization based on DNN scores for events with 2 b-tag jets (2bNN), for the three $\tau\tau$ channels and three eras.

9.3.1 Model building and parameter estimation

In the frequentist interpretation of probability, an experiment measuring an observable can be repeated, resulting in different values of the observable, e.g. the invariant mass of a candidate Higgs boson in a search for the Higgs [97]. The ensemble of values of the observable x gives rise to the probability density function (PDF) $f(x)$, which has the important property that it is normalized to unity:

$$\int f(x) dx = 1.$$

A parametric family of PDFs

$$f(x|\alpha),$$

read “ f of x given α ”, is referred to as a probability model or model. The parameters α typically represent parameters of the theory or an unknown property of the detector’s response. The parameters are not frequentist in nature, unlike x . Out of all the

parameters, typically only a few are of interest, and are called the parameters of interest (POI), labeled μ here. The remaining are referred to as nuisance parameters (NP) [97] and are labeled $\boldsymbol{\theta}$.

$f(x)$ is the probability density for the observable in one event and we wish to describe the probability density for a dataset with many events, $\mathcal{D} = \{x_1, \dots, x_n\}$, called the total probability model \mathbf{f} . For instance, if we also have a prediction for the total number of events expected, called ν , we also account for the overall Poisson probability for observing n events given ν expected:

$$\mathbf{f}(\mathcal{D}|\nu, \alpha) = \text{Poisson}(n|\nu) \prod_{e=1}^n f(x_e|\alpha) \quad (9.4)$$

The likelihood function $L(\alpha)$ is numerically equivalent to $f(x|\alpha)$ for fixed x , or $\mathbf{f}(\mathcal{D}|\alpha)$ with \mathcal{D} fixed [97]. The likelihood function is not a probability density for α and is not normalized to unity:

$$\int L(\alpha) d(\alpha) \neq 1.$$

i.e. the likelihood function is the value of f as a function of α given a fixed value of x .

To estimate the parameter α we use an estimator, which is a function of the data. Take for example the measurement of data distributed according to a Gaussian probability density $f(x|\mu, \sigma) = \text{Gauss}(x|\mu, \sigma)$. One possible estimator of the mean μ , is the mean of the measured data points $\bar{x} = \sum_{i=1}^n x_i/n$ [97].

A commonly used estimator in physics is the maximum likelihood estimator (MLE), defined as the value α which maximizes the likelihood function $L(\alpha)$. This value, labeled $\hat{\alpha}$, also maximizes $\ln L(\alpha)$ and minimizes $-\ln L(\alpha)$. By convention the $-\ln L(\alpha)$ is minimized, in a process called “fitting”, and the maximum likelihood estimate is called the “best fit value”.

2112 9.3.2 Hypothesis testing

2113 In this section we next introduce concepts related to hypothesis testing such as the
2114 test statistic constructed from the ratio of likelihood functions.

2115 The objective of a likelihood analysis is to distinguish different models repre-
2116 senting the various hypotheses, and determine the one that best explains the ex-
2117 perimental outcome. In a search for new physics, a signal is additive on top of the
2118 background. The background-only hypothesis is the null hypothesis, and the signal-
2119 plus-background hypothesis is the alternative.

2120 As a simple example, take the p -value test, for an experiment where we count
2121 events in the signal region, n_{SR} , and expect ν_B background events and ν_S events from
2122 the signal [97]. Then

- 2123 1. The null hypothesis (H_0), i.e. the background-only hypothesis in this experi-
2124 ment, with the probability modeled by $\text{Poisson}(n_{SR}|\nu_B)$.
- 2125 2. The alternate hypothesis (H_1), i.e. signal-plus-background hypothesis, with the
2126 probability modeled by $\text{Poisson}(n_{SR}|(\nu_B + \nu_S))$.

2127 The compatibility of the observed data ν_{SR}^0 and the null hypothesis, is quantified as
2128 the probability that the background-only hypothesis would produce at least as many
2129 events as was observed. This probability is the p -value:

$$p = \sum_{n=n_{SR}^0}^{\infty} \text{Poisson}(n|\nu_B). \quad (9.5)$$

2130 If the p -value is very small, we might reject the null hypothesis. The p -value is not the
2131 probability of the null hypothesis given the data; rather, it expresses the probability
2132 that data with a certain property was obtained, assuming the null hypothesis [97].

2133 The p -value is an example of a test statistic T , which maps the data to a single
2134 real number. The Neyman-Pearson lemma states that out of the infinite possibilities

2135 of choices of test statistic, the uniformly most powerful test statistic is the likelihood
2136 ratio T_{NP} [97]:

$$T_{NP}(\mathcal{D}) = \frac{L(\mathcal{D}|H_1)}{L(\mathcal{D}|H_0)} \quad (9.6)$$

To reiterate, the test statistic T is a real-valued function of the data, implying that a particular probability model $\mathbf{f}(\mathcal{D}|\boldsymbol{\alpha})$ implies a distribution of the test statistic, $f(T|\boldsymbol{\alpha})$, which depends on the value of $\boldsymbol{\alpha}$. With this distribution in hand, the p -value can be evaluated in the following equivalent formulations:

$$p(\boldsymbol{\alpha}) = \int_{T_0}^{\infty} f(T|\boldsymbol{\alpha}) dT \quad (9.7)$$

$$= \int \mathbf{f}(\mathcal{D}|\boldsymbol{\alpha}) \theta(T(\mathcal{D}) - T_0) d\mathcal{D} \quad (9.8)$$

$$= P(T \geq T_0|\boldsymbol{\alpha}) \quad (9.9)$$

2137 where T_0 is the value of T based on the observed data, and $\theta()$ is the Heaviside
2138 function. The size of the test is conventionally chosen to be 10%, 5%, or 1%. As
2139 the p -value depends on $\boldsymbol{\alpha}$ (both the POI and NP), the null hypothesis should not be
2140 rejected if the p -value is larger than the size of the test for any value of the nuisance
2141 parameters.

2142 9.3.3 Confidence intervals

2143 In an example of the measurement of the Standard Model Higgs boson, $\boldsymbol{\alpha}_{POI} =$
2144 $(\sigma/\sigma_{SM}, M_H)$, with σ/σ_{SM} is the ratio of the production cross-section for Higgs with
2145 respect to its value in the SM, and M_H is the unknown mass of the Higgs, values
2146 of these parameters outside specific bounds are said to be “excluded at the 95%
2147 confidence level”. These allowed regions are called confidence levels or confidence
2148 regions, and the parameter values outside of them are considered excluded [97]. A

2149 95% confidence interval does not mean that there is a 95% chance that the true value
 2150 of the parameter is inside the interval. Rather, a 95% confidence interval covers the
 2151 true value 95% of the time (even though we do not know the true value).

2152 To construct a confidence interval for a parameter α , the Neyman Construction
 2153 is used to invert a series of hypothesis tests; i.e. for each possible value of α , the null
 2154 hypothesis is treated as α , and we perform a hypothesis test based on a test statistic.
 2155 To construct a 95% confidence interval, we construct a series of hypothesis tests with
 2156 size of 5%. The confidence interval $I(\mathcal{D})$ is constructed by taking the set of parameter
 2157 values $\boldsymbol{\alpha}$ where the null hypothesis is accepted:

$$I(\mathcal{D}) = \{\boldsymbol{\alpha} | P(T(\mathcal{D}) > k_\alpha | \boldsymbol{\alpha}) < \alpha\}, \quad (9.10)$$

2158 where $T(\mathcal{D})$ is the test statistic, and the last α (not bolded) and the subscript k_α
 2159 refer to the size of the test. A schematic of the Neyman construction is shown in Fig.
 2160 9.1. In a more generalized case, the x -axis is the test statistic T .

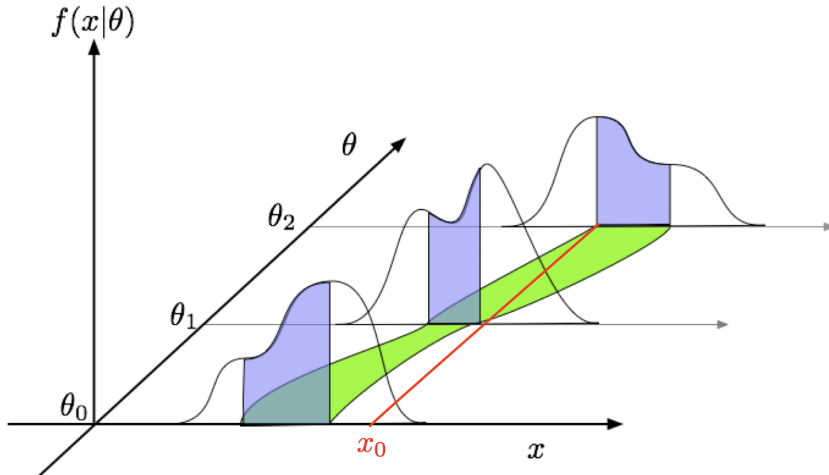


Figure 9.1: Schematic of the Neyman construction for confidence intervals [97]. For each value of θ , we find a region in x where $\int f(x|\theta)dx$ satisfies the size of the test (blue). These regions form a confidence belt (green). The intersection of the observation x_0 (red) with the confidence belt defines the confidence interval $[\theta_1, \theta_2]$ [97].

2161 9.3.4 Profile likelihood ratio

2162 In this section we describe a frequentist statistical procedure based on the profile
 2163 likelihood ratio test statistic, which is implemented using asymptotic distributions.

2164 With a multi-parameter likelihood function $L(\boldsymbol{\alpha})$, the maximum likelihood of
 2165 one specific parameter α_p with other parameters $\boldsymbol{\alpha}_o$ fixed, is called the conditional
 2166 maximum likelihood estimate and is denoted $\hat{\alpha}_p(\boldsymbol{\alpha}_0)$. The process of choosing specific
 2167 values of the nuisance parameters for a given value of μ , $\mathcal{D}_{\text{simulated}}$, and value of global
 2168 observables \mathcal{G} is called profiling. From the full list of parameters $\boldsymbol{\alpha}$, we denote the
 2169 parameter of interest μ , and the nuisance parameters $\boldsymbol{\theta}$.

2170 We construct the profile likelihood ratio,

$$\lambda(\mu) = \frac{L(\mu, \hat{\boldsymbol{\theta}}(\mu))}{L(\mu, \hat{\boldsymbol{\theta}})} \quad (9.11)$$

2171 which depends explicitly on the parameter of interest μ , implicitly on the data \mathcal{D}_{sim}
 2172 and global observables \mathcal{G} , and is independent of the nuisance parameters $\boldsymbol{\theta}$, which
 2173 have been eliminated in profiling [97].

2174 The main conceptual reason for constructing the test statistic from the profile
 2175 likelihood ratio is that asymptotically (i.e. for measurements with many events) the
 2176 distribution of the profile likelihood ratio $\lambda(\mu = \mu_{\text{true}})$ is independent of the values of
 2177 the nuisance parameters [97].

2178 The following p -value is used to quantify the consistency with the hypothesis of a
 2179 signal strength of μ :

$$p_\mu = \int_{\tilde{q}_{\mu, \text{obs}}}^{\infty} f(\tilde{q}_\mu | \mu, \hat{\boldsymbol{\theta}}(\mu, \text{obs})) d\tilde{q}_\mu \quad (9.12)$$

2180 **9.3.5 Modified frequentist method: CL_S**

2181 In the modified frequentist method called CL_S , to test a hypothesis with signal, we
2182 define p'_μ as a ratio of p -values [97]:

$$p'_\mu = \frac{p_\mu}{1 - p_b} \quad (9.13)$$

2183 where p_b is the p -value derived under the background-only hypothesis:

$$p_b = 1 - p_0 \equiv 1 - \int_{\tilde{q}_{\mu,\text{obs}}}^{\infty} f(\tilde{q}_\mu | 0, \hat{\theta}(\mu = 0, \text{obs})) d\tilde{q}_\mu. \quad (9.14)$$

2184 The CL_S upper limit on μ , denoted μ_{up} , is obtained by solving for $p'_{\mu_{up}} = 5\%$.
2185 If testing the compatibility of the data with the background-only hypothesis, we
2186 consider the p_b value defined above and conventionally convert it into the quantile
2187 or “sigma” of a unit Gaussian. z standard deviations (e.g. $z = 5$ in “ 5σ ”) means
2188 that the probability of falling above these standard deviations, equals p_b (e.g. 3σ
2189 corresponds to $p_b = 2.7 \times 10^{-3}$ or 95.43%, and 5σ corresponds to $p_b = 5.7 \times 10^{-7}$ or
2190 99.999943%).

2191 **Chapter 10**

2192 **Results**

2193 **10.1 Results from $bb\tau\tau$**

2194 In each of the three $\tau\tau$ channels studied ($\mu\tau_h$, $e\tau_h$, and $e\mu$), events are divided based
2195 on whether they contain exactly 1 or 2 b-tag jets, and further divided into signal
2196 and control regions (SRs and CRs) using the DNN categorization score as described
2197 in Section 9.2. The control regions demonstrate good agreement between observed
2198 events in data, and the sum of the contributions from expected backgrounds that
2199 are modeled in simulated and embedded samples. The signal regions are defined to
2200 be sensitive to the $h \rightarrow aa \rightarrow bb\tau\tau$ signal. The postfit final observed and expected
2201 distributions of the di-tau invariant mass $m_{\tau\tau}$ reconstructed with SVFit (described
2202 in Section 5.2) are shown in Fig. 10.1 for the $\mu\tau_h$ channel, Fig. 10.2 for the $e\tau_h$
2203 channel, and Fig. 10.3 for the $e\mu$ channel. In all figures, the hypothesized yield for
2204 the $h \rightarrow aa \rightarrow bb\tau\tau$ signal is shown for the pseudoscalar mass $m_a = 35$ GeV and
2205 assuming a branching fraction $B(H \rightarrow aa \rightarrow bb\tau\tau) = 10\%$.

2206 The 95% CL expected and observed exclusion limits on the signal strength of the
2207 branching fraction $B(h \rightarrow aa \rightarrow bb\tau\tau)$ as a function of the pseudoscalar mass m_a
2208 ranging from 12 GeV to 60 GeV, are shown for the three $\tau\tau$ channels and all three

2209 channels combined in Fig. 10.4. The limits are shown as percentages and normalized
2210 to the production cross-section of the Standard Model Higgs boson. No excess of
2211 events above the Standard Model expectations is observed. In the limits for the three
2212 $\tau\tau$ channels combined, expected (observed) limits range from 1.4 to 5.6% (1.7 to
2213 7.6%) for pseudoscalar masses between 12 and 60 GeV.

2214 The $e\mu$ channel is the only channel that has signal sensitivity to the $m_a = 12$
2215 GeV pseudoscalar mass hypothesis, because the minimum required spatial separation
2216 $\Delta R = \sqrt{(\Delta\eta)^2 + (\Delta\phi)^2}$ between the two τ legs is smaller than the other two channels
2217 ($\Delta R < 0.3$ for $e\mu$, compared to $\Delta R < 0.4$ for the other two channels). This decreased
2218 ΔR requirement results in better signal acceptance for low mass signals for the $e\mu$
2219 channel. The $\mu\tau_h$ and $e\tau_h$ channels are most sensitive to the intermediate mass points
2220 studied, since the analysis targets a resolved signature: at low mass points, the tau
2221 legs are boosted, and at high mass points, the $m_{\tau\tau}$ distributions in signal have larger
2222 overlap with background distributions. In the combination of the three $\tau\tau$ channels,
2223 the limit for $m_a = 12$ GeV comes only from the $e\mu$ channel, and the best sensitivity
2224 is attained at intermediate mass points around $m_a = 20$ GeV to 45 GeV.

2225 To set limits on the branching fraction of the 125 GeV Higgs to the two pseu-
2226 doscalars, $B(h \rightarrow aa)$, we interpret the results in four types of 2HDM+S, which were
2227 introduced in Section 1.4. In 2HDM+S, the theorized branching fraction of the pseu-
2228 doscalars depends on the 2HDM+S model type, the pseudoscalar mass m_a , and the
2229 ratio of the two Higgs doublets' vacuum expectation values $\tan\beta$. In Type I models,
2230 the branching fraction is independent of $\tan\beta$, while in Types II, III, and IV, it is
2231 a function of m_a and $\tan\beta$. Limits for the $bb\tau\tau$ final state as a function of m_a for
2232 2HDM+S Type I (valid for all $\tan\beta$ values), Type II with $\tan\beta = 2.0$, Type III with
2233 $\tan\beta = 2.0$, and Type IV with $\tan\beta = 0.6$ are overlaid and shown in Fig. 10.5a.

2234 10.2 Combination with $bb\mu\mu$ final state

2235 Results from this analysis for the $h \rightarrow aa \rightarrow bb\tau\tau$ final state are combined with the
2236 analysis for the $h \rightarrow aa \rightarrow bb\mu\mu$ final state [98]. While the predicted branching ratio
2237 for $aa \rightarrow bb\mu\mu$ is comparatively small, the $bb\mu\mu$ final state has competitive results
2238 due to the excellent di-muon resolution measured by CMS. The $bb\mu\mu$ analysis uses
2239 an unbinned fit to the data using the di-muon mass $m_{\mu\mu}$ distribution. Details can be
2240 found in [98].

2241 Combining the results is possible since the $bb\tau\tau$ analysis explicitly rejects events
2242 with extra leptons, so there is no overlap between the events studied in the $bb\tau\tau$
2243 analysis and the $bb\mu\mu$ analysis. In the statistical combination, several systematic
2244 uncertainties are treated as correlated: the integrated luminosity normalization, the
2245 b-tagging scale factor, the scale factors related to muon reconstruction, identifica-
2246 tion, and trigger efficiencies, the inefficiency in the ECAL trigger readout, and the
2247 theoretical uncertainties related to signal modeling.

2248 Since the results in both final states are statistically limited, the combination ben-
2249 efits from the additional data. For $m_a = 35$ GeV, all systematic uncertainties amount
2250 to around 6% of the total uncertainty, with the dominant systematic uncertainties
2251 coming from jet energy systematics in the $bb\mu\mu$ final state, theoretical uncertainties
2252 in the signal, and uncertainties in the QCD multijet backgrounds in the $e\mu$ channel
2253 of the $bb\tau\tau$ final state.

2254 The mass distributions of the di-muon and di-tau objects ($m_{\mu\mu}$ and $m_{\tau\tau}$) are
2255 compared to the data in a combined maximum likelihood fit to derive upper limits
2256 on $B(h \rightarrow aa)$. The observed limits at 95% CL on $B(h \rightarrow aa)$ for different 2HDM+S
2257 scenarios, are shown for the search for $h \rightarrow aa \rightarrow bb\mu\mu$ in Fig. 10.5b, and the
2258 combined analyses $h \rightarrow aa \rightarrow bb\ell\ell$ in Fig. 10.6.

2259 Exclusion limits in a two-dimensional plane as a function of $\tan\beta$ and m_a are
2260 set for 2HDM+S Types II, III, and IV in Fig. 10.7. The most stringent constraints

are observed for 2HDM+S type III because of large branching fractions predicted in theory, with predicted branching fractions between 0.47 and 0.42 for $\tan \beta = 2.0$ and values of m_a between 15 and 60 GeV, compared to the observed 95% CL upper limits which are between 0.08 and 0.03. For 2HDM+S type IV, the predicted branching fractions from theory are between 0.26 and 0.20 for $\tan \beta = 0.6$ for values of m_a between 15 and 60 GeV, and the 95% CL observed upper limits are between 0.12 and 0.05.

The combined results from $h \rightarrow aa \rightarrow bb\ell\ell$ are compared with CMS results in other final states as a function of the pseudoscalar mass m_a : for 2HDM+S type I in Fig. 10.8, type II with $\tan \beta = 2.0$ in Fig. 10.9, and type III with $\tan \beta = 2.0$ in Fig. 10.10. In other scenarios, e.g. type III with $\tan \beta = 5.0$, more stringent limits are set by analyses in other final states, $\mu\mu\tau\tau$ in this case. Other summary plots for other model types and $\tan \beta$ values can be found at [99].

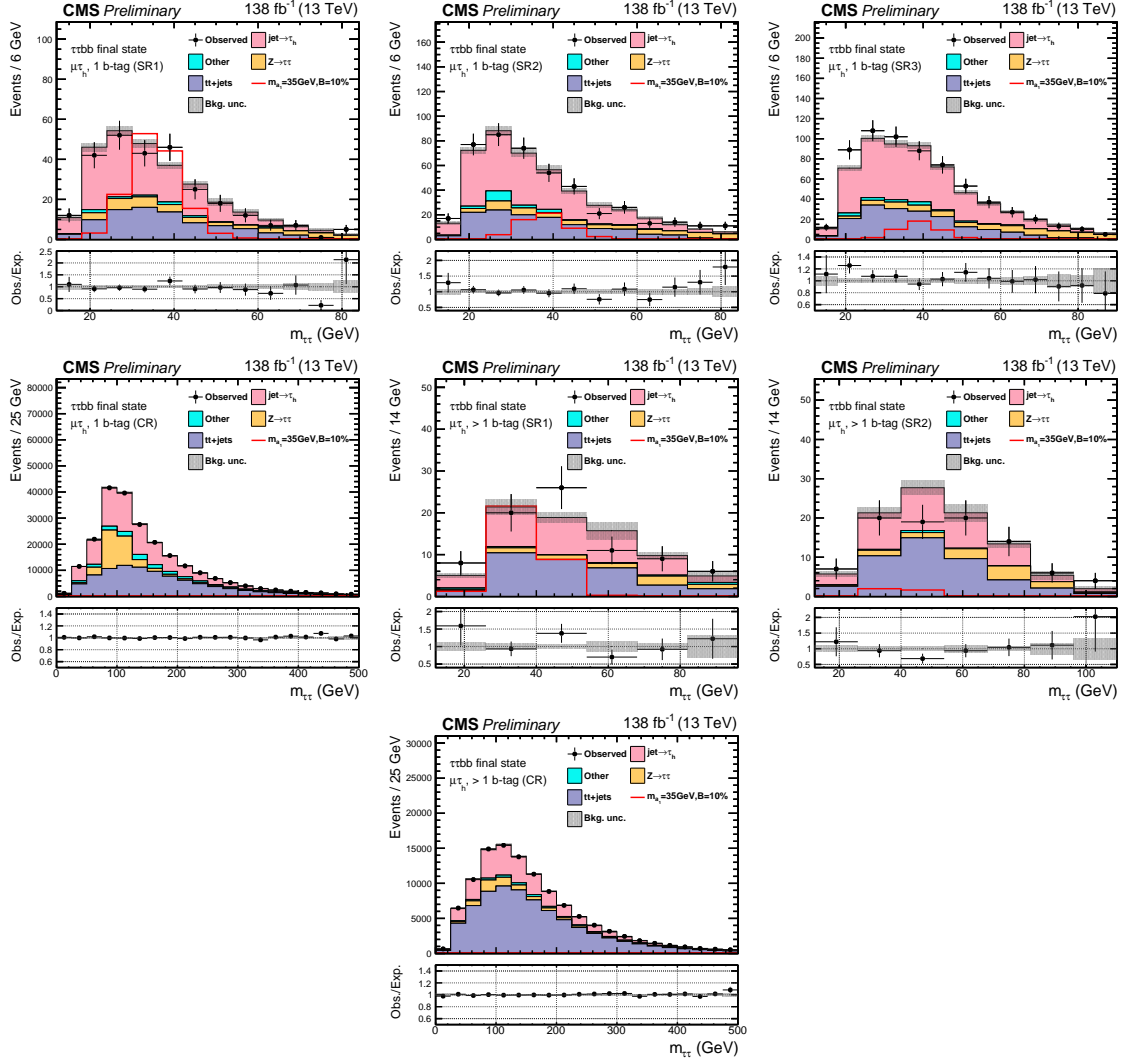


Figure 10.1: Postfit final $m_{\tau\tau}$ observed and expected distributions, and the observed/expected ratios, in the $\mu\tau_h$ channel [41]. Events are divided into the 1 b-tag jet signal regions (SR1, SR2, SR3) (*top row*), 1 b-tag jet control region (*middle row*), 2 b-tag jet signal regions (SR1, SR2) (*middle row*), and lastly the 2 b-tag jet control region (CR) (*bottom*). Statistical and systematic sources of uncertainties in the expected events are added in quadrature and labeled “Bkg. unc” (*shaded gray*). The dominant backgrounds in all categories are jets faking the τ_h leg (*pink*), $Z \rightarrow \tau\tau$ (*orange*), and $t\bar{t}+j$ ets (*purple*). For illustrative purposes, the beyond-Standard Model signal yield from $h \rightarrow aabb\tau\tau$ is shown for the pseudoscalar mass hypothesis $m_a = 35$ GeV, assuming a branching fraction $B(h \rightarrow aa \rightarrow bb\tau\tau) = 10\%$ (*red line*).

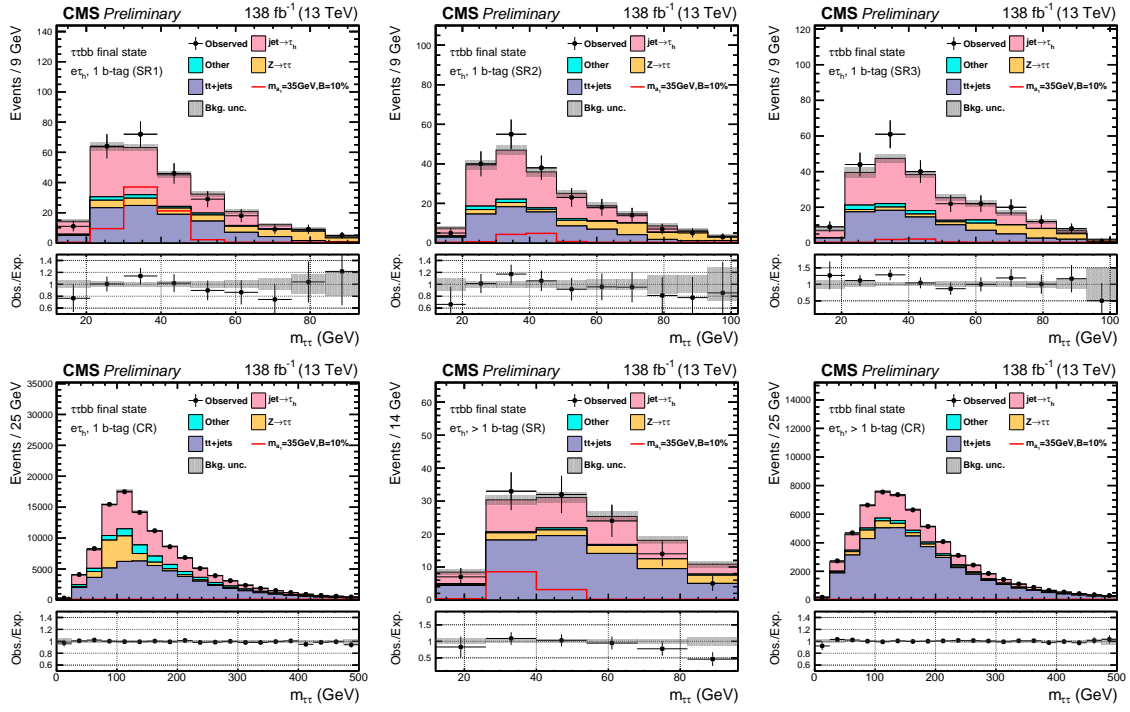


Figure 10.2: Postfit final observed and expected $m_{\tau\tau}$ distributions, and the observed/expected ratios, in the $e\tau_h$ channel [41]. Events are divided into the 1 b-tag jet signal regions (SR1, SR2, SR3) (*top row*), the 1 b-tag jet control region (CR) (*bottom row*), and 2 b-tag jet signal region (SR) and control region (CR) (*bottom row*). Statistical and systematic sources of uncertainties in the expected events are added in quadrature and labeled “Bkg. unc” (*shaded gray*). In this channel, the dominant backgrounds are jets faking the τ_h leg (*pink*), $Z \rightarrow \tau\tau$ (*orange*), and $t\bar{t}+jets$ (*purple*). For illustrative purposes, the beyond-Standard Model signal yield from $h \rightarrow aabb\tau\tau$ is shown for the pseudoscalar mass hypothesis $m_a = 35$ GeV, assuming a branching fraction $B(h \rightarrow aa \rightarrow bb\tau\tau) = 10\%$ (*red line*).

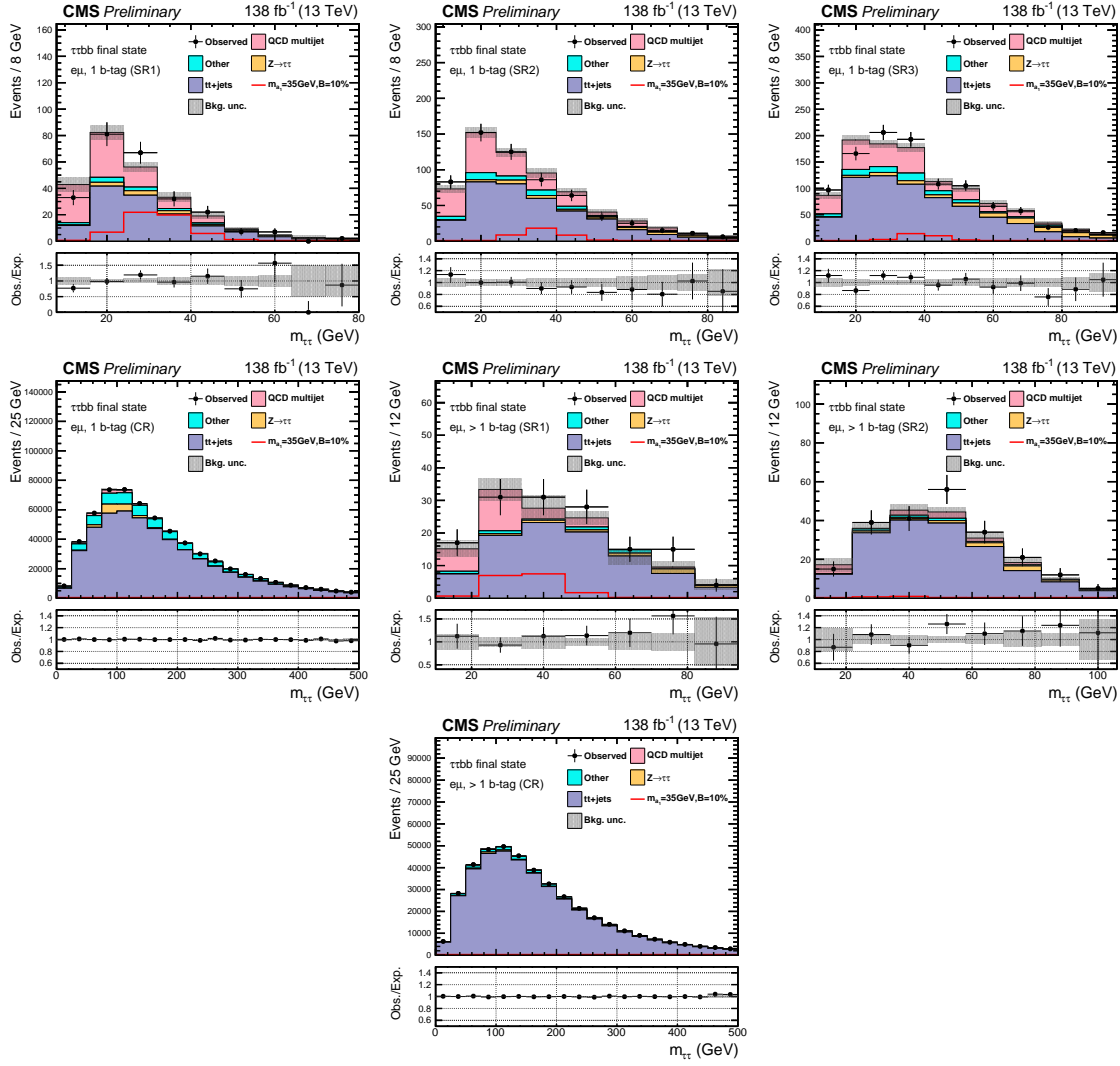


Figure 10.3: Postfit final observed and expected $m_{\tau\tau}$ distributions, and the observed/expected ratios, in the $e\mu$ channel [41]. Events are divided into the 1 b-tag jet signal regions (SR1, SR2, and SR3) (*top row*), 1 b-tag jet control region (CR) (*middle row*), 2 b-tag jet signal regions (SR1 and SR2) (*middle row*), and 2 b-tag jet control region (CR) (*bottom row*). Statistical and systematic sources of uncertainties in the expected events are added in quadrature and labeled “Bkg. unc” (*shaded gray*). The $t\bar{t}+j$ process (*purple*) is a major background, and in the signal regions the QCD multijet (*pink*) is also a major background. For illustrative purposes, the beyond-Standard Model signal yield from $h \rightarrow aabb\tau\tau$ is shown for the pseudoscalar mass hypothesis $m_a = 35$ GeV, assuming a branching fraction $B(h \rightarrow aa \rightarrow bb\tau\tau) = 10\%$ (*red line*).

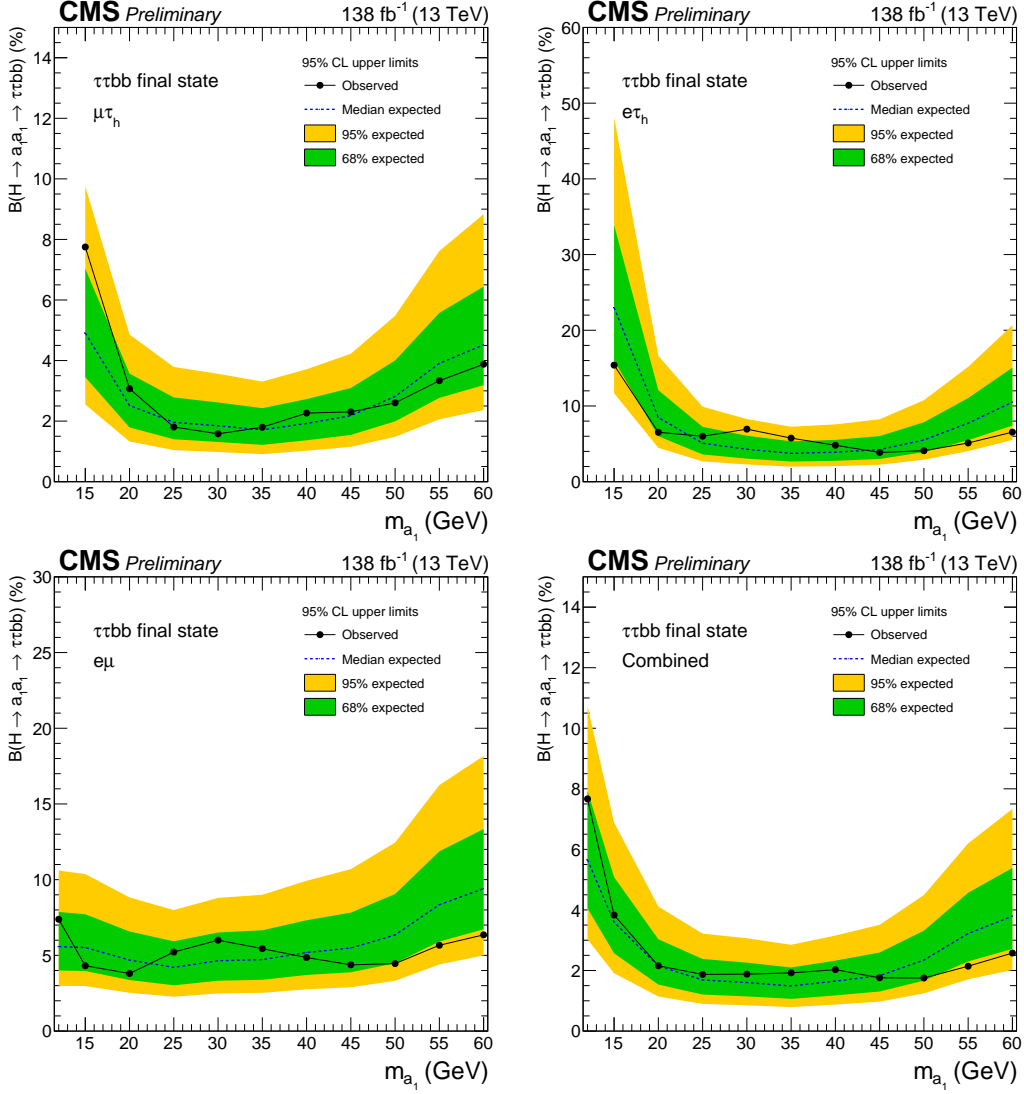
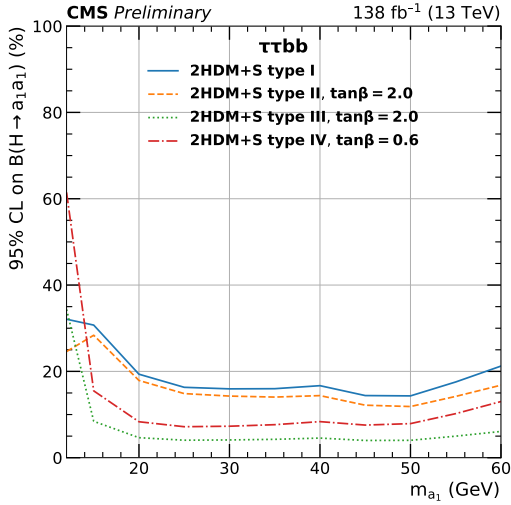
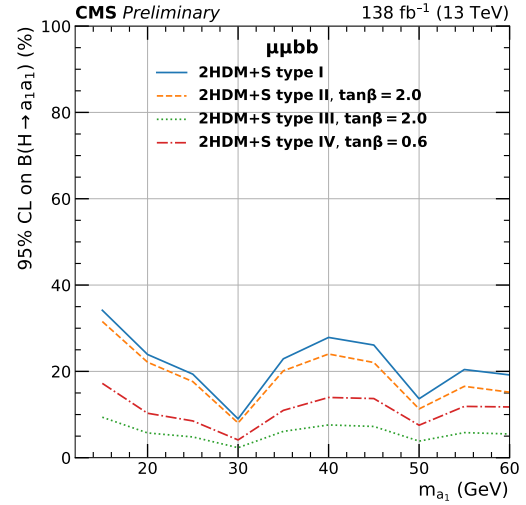


Figure 10.4: Observed 95% CL exclusion limits (*black, solid lines*) and expected 95% CL and 68% CL limits (*shaded yellow and green*) on the branching fraction $B(h \rightarrow aa \rightarrow bb\tau\tau)$ in percentages, assuming the Standard Model production for the 125 GeV Higgs (h). Limits are shown for the $\mu\tau_h$ channel (*top left*), the $e\tau_h$ channel (*top right*), and the $e\mu$ channel (*bottom left*), and lastly the combination of all three channels (*bottom right*) [41]. The dataset corresponds to 138 fb^{-1} of data collected in the years 2016-2018 at a center-of-mass energy 13 TeV. Only the $e\mu$ channel has sensitivity to the mass hypothesis $m_a = 12 \text{ GeV}$. The best sensitivity is attained at intermediate mass points.



(a) $bb\tau\tau$ final state.



(b) $bb\mu\mu$ final state.

Figure 10.5: Observed 95% CL upper limits on $B(h \rightarrow aa)$ in %, for the $bb\tau\tau$ final state (*left*) and $bb\mu\mu$ final state (*right*) using the full Run 2 integrated luminosity of 138 fb^{-1} in 2HDM+S type I (blue), type II with $\tan\beta = 2.0$ (orange dashed), type III with $\tan\beta = 2.0$ (dotted green), and type IV with $\tan\beta = 0.6$ (red dashed) [41]. Linear interpolation is used between points in the graphs. The $\tan\beta$ values chosen here correspond to the most stringent limits in each model.

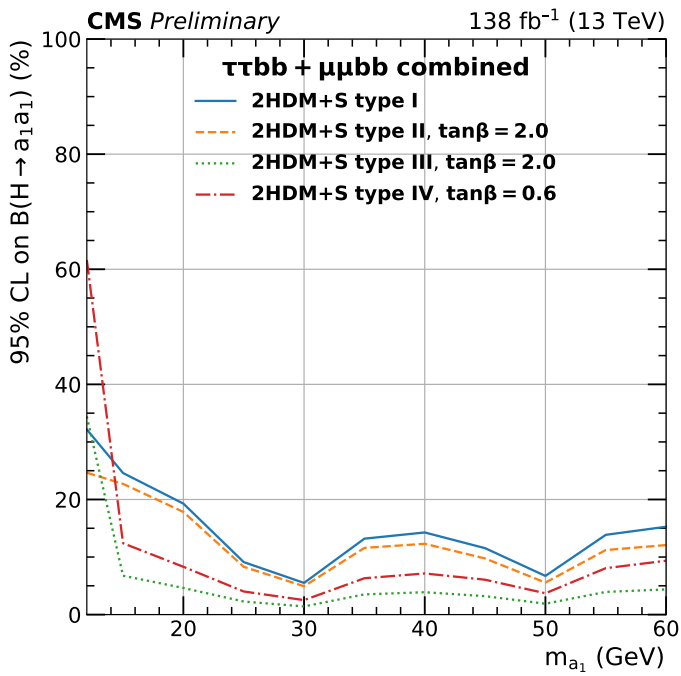


Figure 10.6: Observed 95% CL upper limits on the branching fraction of the 125 GeV Higgs boson to two pseudoscalars, $B(h \rightarrow aa)$, in percentages, as a function of the pseudoscalar mass m_a , in 2HDM+S type I (blue), type II with $\tan\beta = 2.0$ (orange dashed), type III with $\tan\beta = 2.0$ (dotted green), and type IV with $\tan\beta = 0.6$ (red dashed), for the combination of $bb\mu\mu$ and $bb\tau\tau$ channels using the full Run 2 integrated luminosity of 138 fb^{-1} [41].

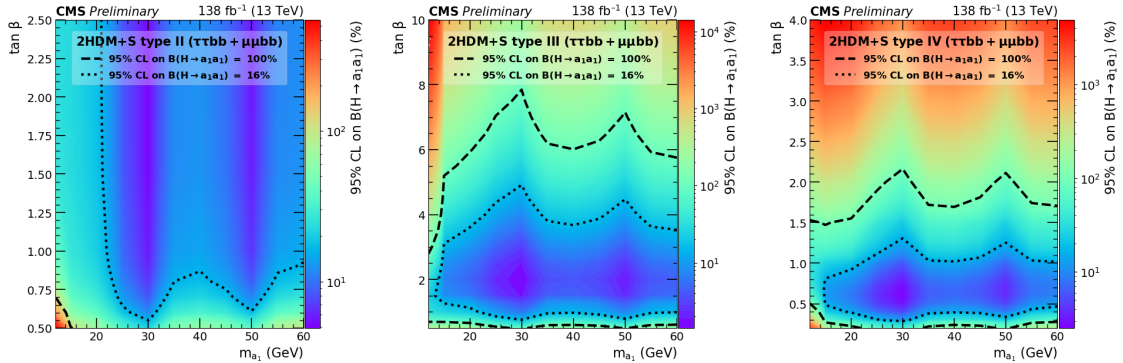


Figure 10.7: Observed 95% CL upper limits on $\mathcal{B}(h \rightarrow aa)$ in %, for the combination of $bb\mu\mu$ and $bb\tau\tau$ channels using the full Run 2 integrated luminosity of 138 fb^{-1} for Type II (*left*), Type III (*middle*), and Type IV (*right*) 2HDM+S in the $\tan \beta$ vs. m_a phase space. The contours (*dashed black*) correspond to branching fractions of 100% and 16%, where 16% is the combined upper limit on Higgs boson to undetected particle decays from previous Run-2 results. All points inside the contour are allowed within that upper limit. Linear extrapolation has been used between different points on the figures [41].

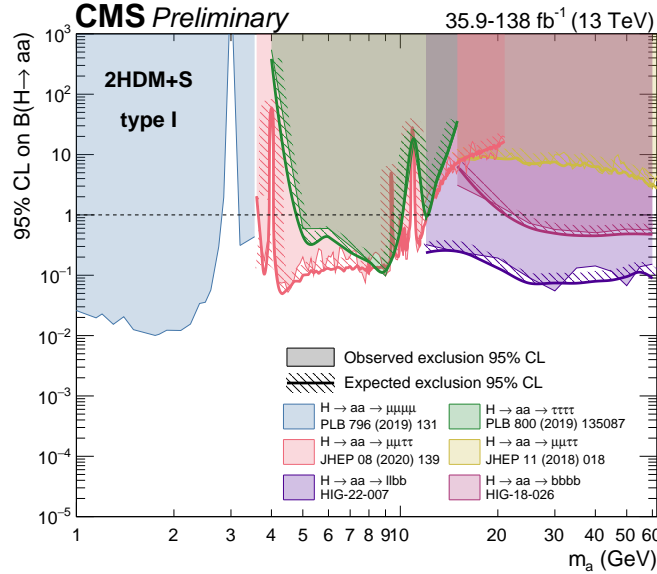


Figure 10.8: Summary plot of current 95% limits on the branching ratio of the 125 GeV Higgs boson to two pseudoscalars, normalized to the Standard Model Higgs production cross-section, $\frac{\sigma(h)}{\sigma_{\text{SM}}} \times B(h \rightarrow aa)$ in the 2HDM+S type I scenario performed with data collected at 13 TeV [99]. Results from different final states studied at CMS are overlaid on this figure: $\mu\mu\mu\mu$ (blue), $\tau\tau\tau\tau$ (green), boosted $2\mu 2\tau$ (red), resolved $2\mu 2\tau$ (yellow), $bbbb$ (magenta), and the combined result for $\ell\ell bb$ ($\ell = \mu, \tau$) (purple).

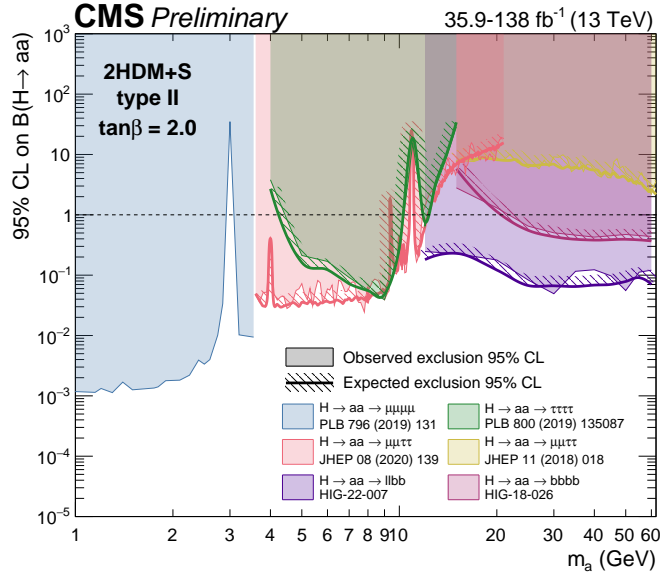


Figure 10.9: Summary plot of current observed and expected 95% CL limits on the branching ratio of the 125 GeV Higgs boson to two pseudoscalars, normalized to the Standard Model Higgs production cross-section, $\frac{\sigma(h)}{\sigma_{\text{SM}}} \times B(h \rightarrow aa)$, in the 2HDM+S type II scenario with $\tan \beta = 2.0$, obtained at CMS with data collected at 13 TeV [99]. Results from different final states studied at CMS are overlaid on this figure: $\mu\mu\mu\mu$ (blue), $\tau\tau\tau\tau$ (green), boosted $2\mu 2\tau$ (red), resolved $2\mu 2\tau$ (yellow), $bbbb$ (magenta), and the combined result for $\ell\ell bb$ ($\ell = \mu, \tau$) (purple).

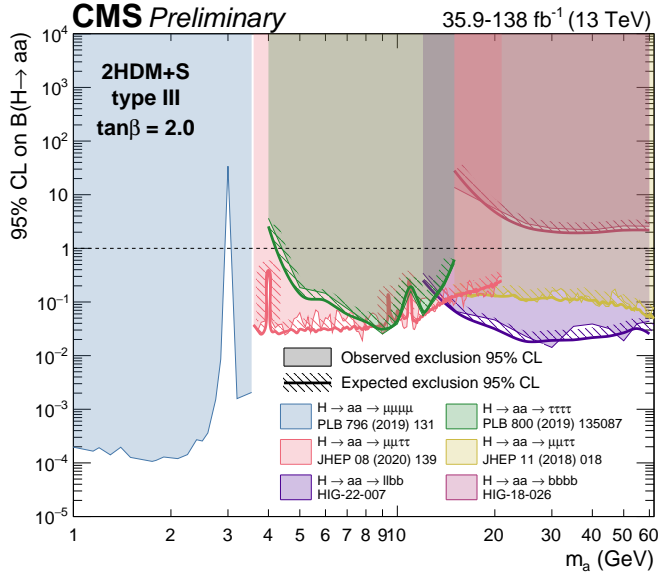


Figure 10.10: Summary plot of current observed and expected 95% CL limits on the branching ratio of the 125 GeV Higgs boson to two pseudoscalars, normalized to the Standard Model Higgs production cross section, $\frac{\sigma(h)}{\sigma_{SM}} \times B(h \rightarrow aa)$ in the 2HDM+S type-III scenario with $\tan \beta = 2.0$, obtained at CMS with data collected at 13 TeV [99]. Results from different final states studied at CMS are overlaid on this figure: $\mu\mu\mu\mu$ (blue), $\tau\tau\tau\tau$ (green), boosted $2\mu 2\tau$ (red), resolved $2\mu 2\tau$ (yellow), $bbbb$ (magenta), and the combined result for $\ell\ell bb$ ($\ell = \mu, \tau$) (purple).

2274 **Chapter 11**

2275 **Asymmetric exotic Higgs decays**

2276 This chapter presents progress towards a search for exotic Higgs decays to two light
2277 scalars with unequal mass ($h \rightarrow a_1 a_2$) final states with bottom quarks and τ leptons,
2278 with plans to interpret the results in the context of Two Real Singlet Models (TRSMs),
2279 described in Section 1.5. Compared to the symmetric decay scenario $h \rightarrow aa$ which
2280 has been studied in multiple final states at CMS with stringent limits set on the
2281 various 2HDM+S scenarios, this asymmetric decay scenario has not been directly
2282 searched for at the CMS experiment. Section 11.1 lists the mass hypotheses of the
2283 new particles a_1 and a_2 that will be studied. Section 11.2 describes the studies on
2284 which channels the analysis will be carried out in. Section 11.3 shows the control
2285 plots produced using the analysis framework that will be used for this analysis.

2286 **11.1 Signal masses**

2287 As discussed in Section 1.5, $h \rightarrow a_1 a_2$ can result in a “cascade” decay if one of the
2288 scalars, a_2 is sufficiently heavy ($m_{a_2} > 2m_{a_1}$). The “non-cascade” case is where the
2289 light scalars decay directly to Standard Model particles.

2290 The mass hypotheses (mass points) (m_{a_1}, m_{a_2}) studied here are:

- *Cascade mass points:* (15, 30), (15, 40), (15, 50), (15, 60), (15, 70), (15, 80), (15, 90), (15, 100), (15, 110), (20, 40), (20, 50), (20, 60), (20, 70), (20, 80), (20, 90), (20, 100), (30, 60), (30, 70), (30, 80), and (30, 90) GeV
- *Non-cascade mass points:* (15, 20), (15, 30), (20, 30), (20, 40), (30, 40), (30, 50), (30, 60), (40, 50), (40, 60), (40, 70), (40, 80), (50, 60), and (50, 70) GeV

Samples were produced using the MadGraph5_aMCatNLO event generator, for each signal mass point in the gluon-gluon fusion (ggF) and vector boson fusion (VBF) production modes of the 125 GeV Higgs boson. In the sample generation, the decays of a to Standard Model particles were specified to be decays to bottom quarks or τ leptons.

11.2 Cascade scenario signal studies

Studies of the signal phenomenology in the cascade scenario were performed to determine the viability of the $4b2\tau$ and/or $2b4\tau$ channels.

Cross sections and branching fractions of the $4b2\tau$ and $2b4\tau$ final states were compared using cross-section predictions provided by the authors of [7]. For an example mass point $m_{a_2} = 80$ GeV, $m_{a_1} = 30$ GeV, the branching fractions to $4b2\tau$ is ten times larger than $2b4\tau$: $B(h \rightarrow a_1 a_2 \rightarrow 3a_1 \rightarrow 4b2\tau) = 0.00857$, vs. $B(h \rightarrow a_1 a_2 \rightarrow 3a_1 \rightarrow 2b4\tau) = 0.00068$. The $4b2\tau$ final state is chosen for this analysis.

In general the four b-flavor jets have low p_T at generator level, as illustrated for example mass points (100, 15) GeV and (40, 20) GeV in Fig. 11.1. The p_T distribution of the sub-leading jet peaks at an energy below 20 GeV, with the third and fourth jets tending to have even softer energies.

An event category with three or more b-tag jets was determined to be infeasible due to low statistics in this category, due to the difficulties in reconstructing the third

2316 and fourth b-flavor jets which have very low transverse momenta p_T . Event categories
 2317 with exactly 1 b-tag jet and ≥ 2 b-tag jets will be used.

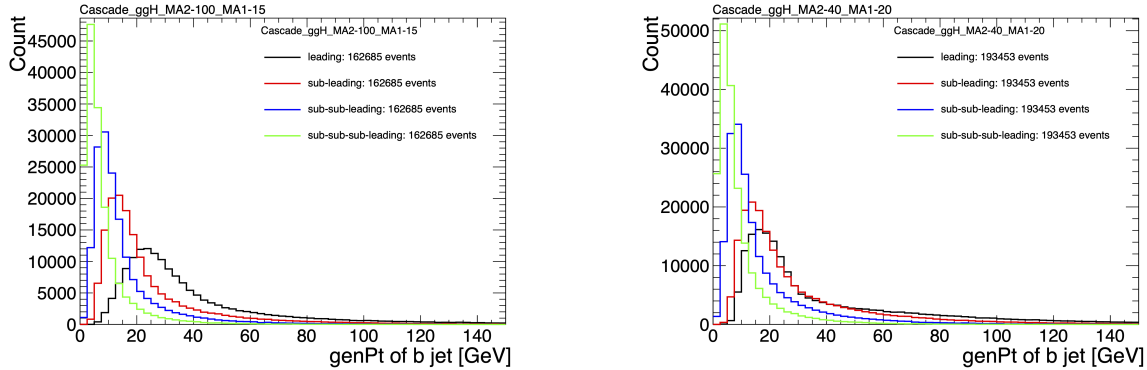


Figure 11.1: Generator-level b-flavor jet transverse momenta p_T , for $h \rightarrow a_1 a_2$ cascade scenario in the $4b2\tau$ final state, for mass hypotheses $(m_{a_1}, m_{a_2}) = (100, 15)$ GeV (*left*) and $(40, 20)$ GeV (*right*). In each plot the generator-level p_T of the leading (*black*), sub-leading (*red*), third (*blue*), and fourth (*light green*) are overlaid.

2318 In the $4b2\tau$ final state, the possibility of the leading and sub-leading b-tag jets
 2319 being sufficiently close in ΔR to require boosted jet reconstruction techniques was
 2320 explored. In the $4b2\tau$ case, the two b-flavor-jets in the generated event that were
 2321 spatially closest in ΔR were considered as one object. This two b-flavor jet object was
 2322 spatially matched in ΔR to the jets reconstructed with the standard AK4 algorithm
 2323 which uses a cone size of $\Delta R = 0.4$. The quality of the p_T resolution (computed as
 2324 $(p_{T,\text{reconstructed}} - p_{T,\text{gen}})/p_{T,\text{gen}}$) and closeness in distance ΔR of the reconstructed jet
 2325 to the nearest generator-level jets, was seen to depend on the absolute and relative
 2326 masses of the light scalars. The best (worst) performance occurred in samples with
 2327 large (small) mass differences between the heavier scalar a_2 and the lighter scalar a_1 ,
 2328 as illustrated for the mass hypotheses (m_{a_1}, m_{a_2}) (100, 15) GeV and (40, 20) GeV in
 2329 Fig. 11.2.

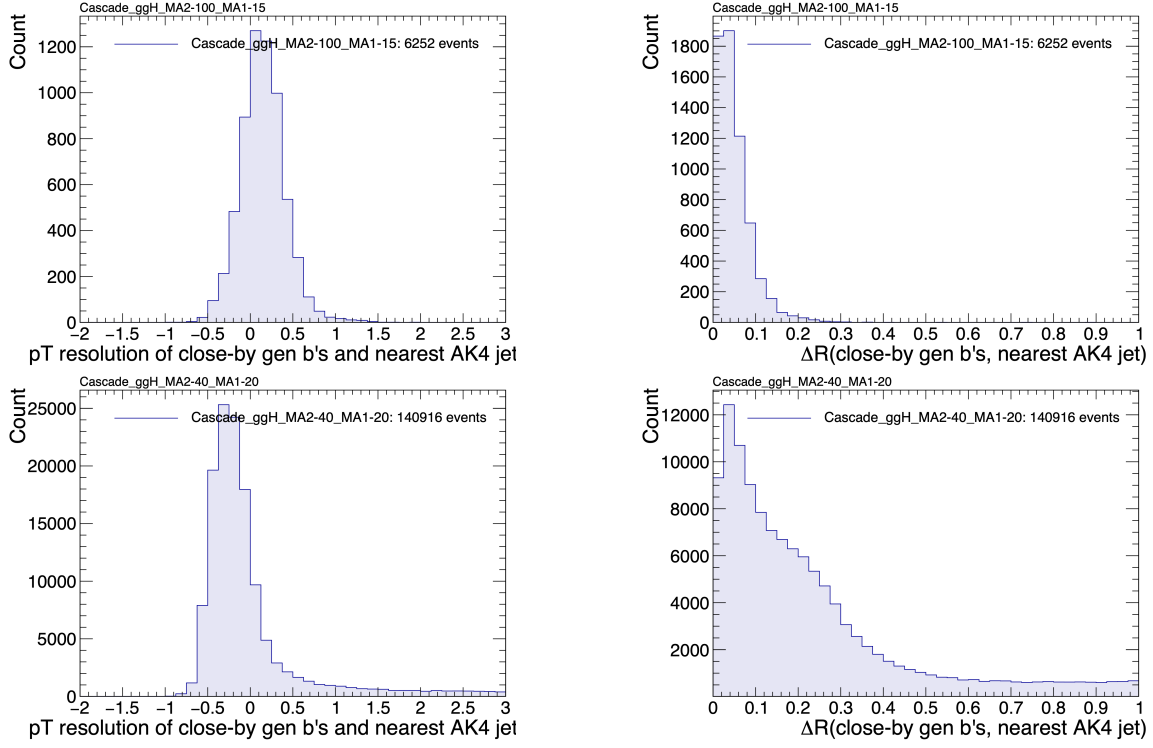


Figure 11.2: Distributions (arbitrary units) of transverse momentum p_T resolution and ΔR between the two closest generator-level b jets, treated as one object, and the nearest reconstructed AK4 jet, for two different $h \rightarrow a_1 a_2$ mass hypotheses (m_{a_1}, m_{a_2}) = (100, 15) GeV (top left, top right) and (40, 20) GeV (bottom left, bottom right) in the ggH production of the 125 GeV h . In the (40, 20) GeV mass point, the longer p_T resolution tail (bottom left) indicates that the reconstructed jet underestimates the generator b -flavor jets' energy, and the significant fraction of events with larger ΔR values (bottom right) indicate worse matching.

11.3 Current control plots for $\mu\tau_h$ channel

The $\tau\tau$ states for the $h \rightarrow a_1 a_2$ to $4b2\tau$ analysis will be similar to those studied in $h \rightarrow aa \rightarrow bb\tau\tau$. For the $\mu\tau_h$ channel, histograms of the key kinematic variables are made for data and the sum of the expected backgrounds, which are estimated from Monte Carlo samples, embedded samples, and the data-driven method for estimating jets faking τ_h as described in Chapter 7. Nominal values of the scale factors and event reweighting are applied, as described in Chapter ???. The errors shown in the figures only include statistical errors and only several of the full set of systematic errors (only those associated with the lepton energy scales and τ_h identification efficiency,

2339 described in Sections 5.3.1, 5.3.2, and 5.3.4).

2340 The p_T , η , and ϕ of the leading muon and hadronic tau τ_h , and the di-tau visible
2341 mass m_{vis} and momentum $p_{T,\text{vis}}$, are shown in Fig. 11.3. The p_T , η , and ϕ of the the
2342 leading and sub-leading b-tag jets, and the missing transverse energy magnitude and
2343 azimuthal direction, are shown in Fig. 11.4.

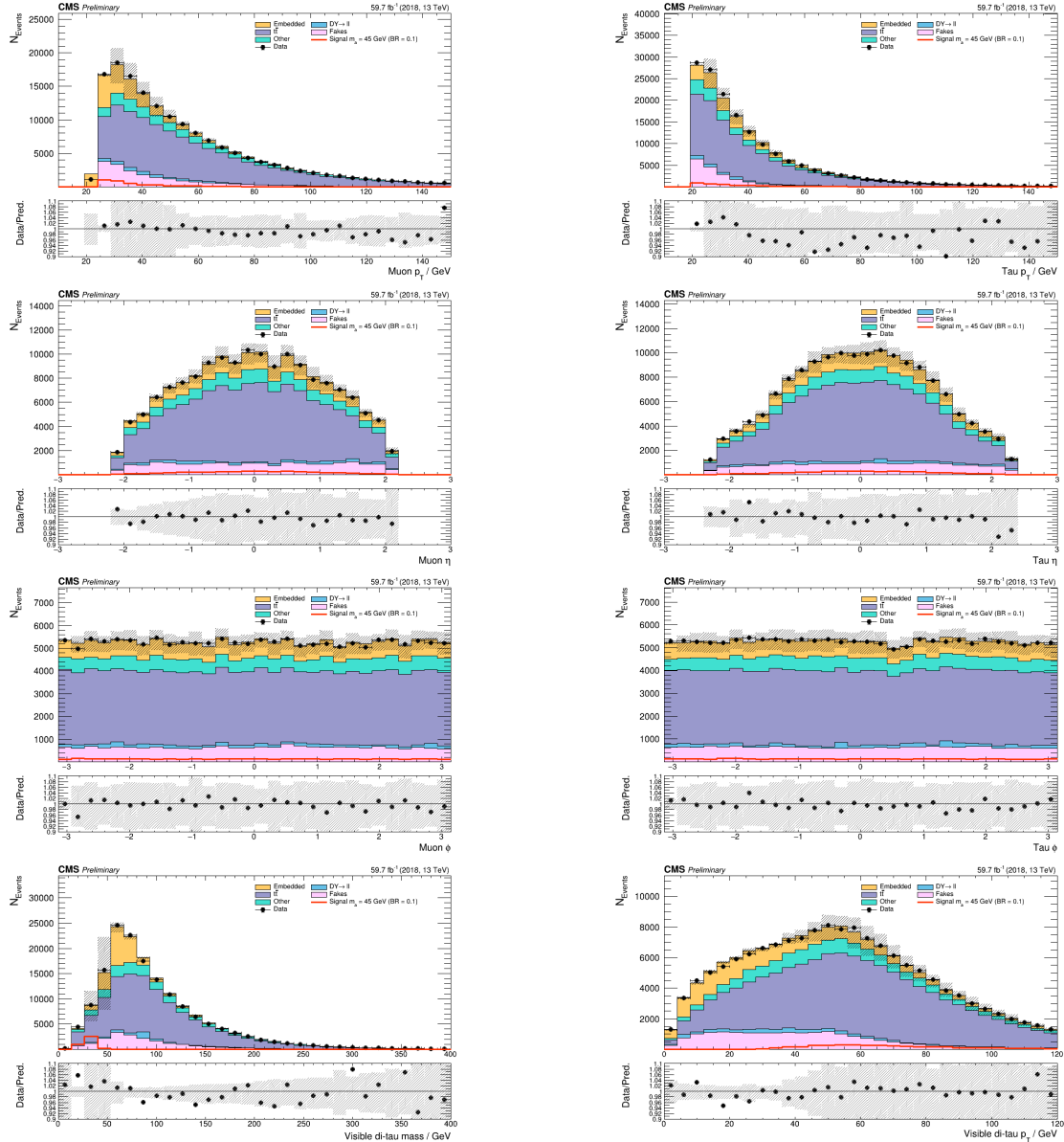


Figure 11.3: Kinematic properties of the leading muon and τ_h in the $\mu\tau_h$ channel: p_T (top row), η (second row), and ϕ (third row). The visible 4-momenta of the muon and τ_h are summed, giving the visible di-tau mass m_{vis} and transverse momentum $p_{T,\text{vis}}$. The errors shown in the figures only include statistical errors and only several of the full set of systematic errors (only those associated with the lepton energy scales and τ_h identification efficiency).

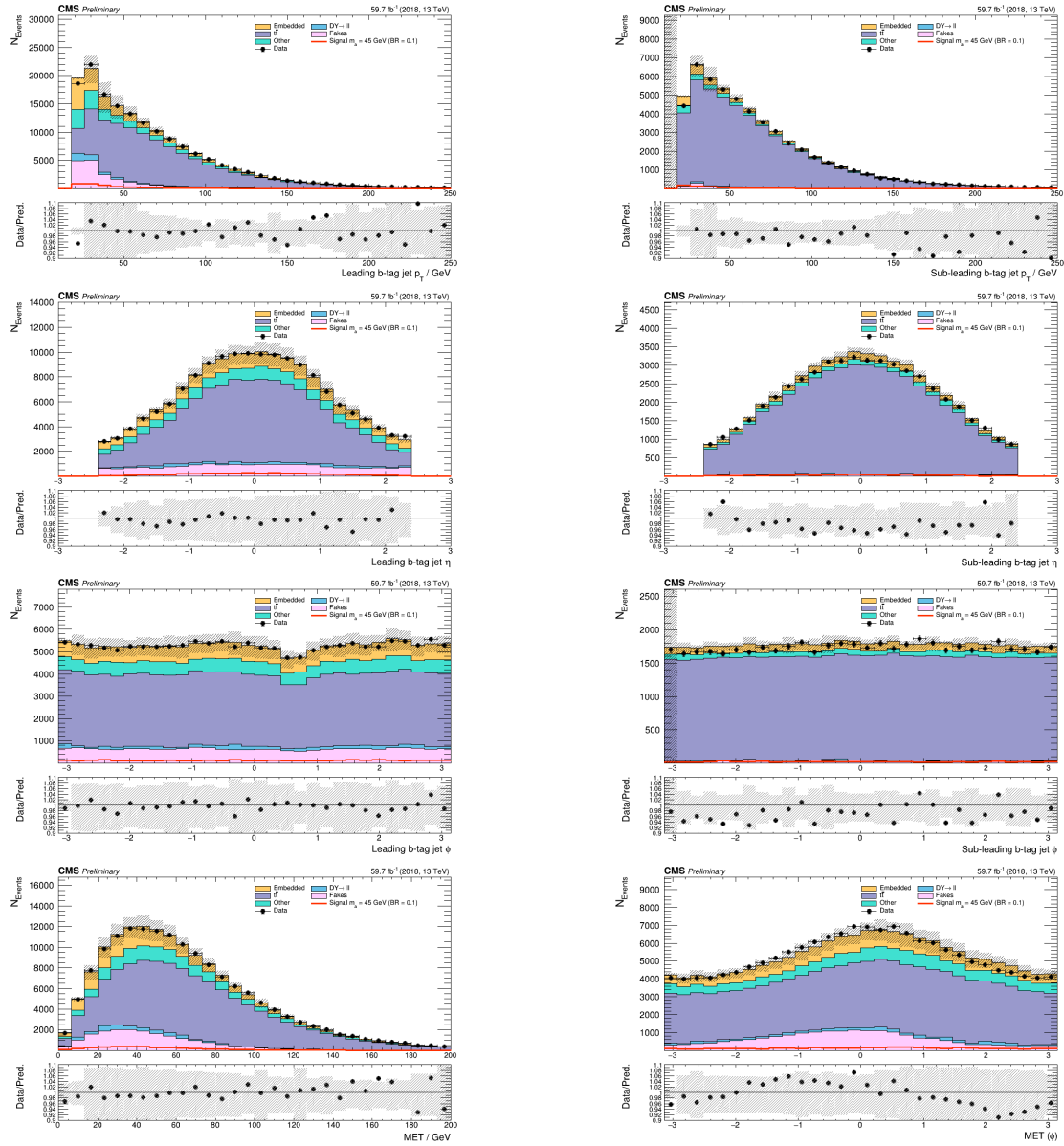


Figure 11.4: Kinematic properties of the leading and sub-leading b-tag jets in the $\mu\tau_h$ final state: jet p_T (*top row*), η (*second row*), ϕ (*third row*), as well as the missing transverse energy magnitude and azimuthal direction (*bottom row*). The errors shown in the figures only include statistical errors and only several of the full set of systematic errors (only those associated with the lepton energy scales and τ_h identification efficiency).

²³⁴⁴ **Chapter 12**

²³⁴⁵ **Conclusion and outlook**

²³⁴⁶ With the discovery of a Higgs boson with mass 125 GeV at the LHC in 2012, the LHC
²³⁴⁷ and CMS physics program has evolved to include the precise characterization of the
²³⁴⁸ 125 GeV Higgs boson and searching for evidence of additional Higgs particles in an
²³⁴⁹ extended Higgs sector. This thesis presents a direct search at CMS for exotic decays
²³⁵⁰ of the Higgs boson with mass 125 GeV in data collected in the years 2016-2018 in
²³⁵¹ proton-proton collisions at center-of-mass energy 13 TeV, to two light neutral scalar
²³⁵² particles that decay to two bottom quarks and two tau leptons ($h \rightarrow aa \rightarrow bb\tau\tau$). The
²³⁵³ results are combined with another search that was performed in the $h \rightarrow aa \rightarrow bb\mu\mu$
²³⁵⁴ final state, giving the most stringent limits to date for theories with Two Higgs
²³⁵⁵ Doublet Models extended with a singlet scalar (2HDM+S), for pseudoscalar masses
²³⁵⁶ m_a ranging from 15 GeV to 60 GeV, in a number of 2HDM+S scenarios such as type
²³⁵⁷ II and III with $\tan\beta = 2.0$.

²³⁵⁸ As the rich physics program of CMS has set stringent limits on the exotic decay
²³⁵⁹ $h \rightarrow aa$, we turn our attention to direct searches for decays to light neutral scalars
²³⁶⁰ with potentially unequal mass, $h \rightarrow a_1a_2$, which has not been performed at CMS
²³⁶¹ to date. Preliminary studies on $h \rightarrow a_1a_2$ signals in the Two Real Singlet Model
²³⁶² (TRSM) are shown, and work is ongoing to develop the analysis for $h \rightarrow a_1a_2$ in final

2363 states with bottom quarks and tau leptons.

2364 To ensure the continued performance of the CMS detector and to enhance its
2365 data-taking capabilities in the intense pileup conditions of the Phase-2 upgrade of
2366 the High-Luminosity LHC, upgrades of the Level-1 Trigger are paramount for filter-
2367 ing the increased data rate of the HL-LHC. This thesis presents work on the stan-
2368 dalone barrel calorimeter algorithm for reconstructing and identifying electron and
2369 photon candidates, using high granularity crystal-level information from the ECAL
2370 subdetector. For Phase-2, the increase in the granularity of information sent from
2371 the electromagnetic calorimeter to the Level-1 trigger, from energy sums over towers
2372 (which are 5×5 in crystals) to crystal-level information, allows for the implementation
2373 of a more sophisticated clustering algorithm that can exploit the fact that genuine
2374 electrons and photons tend to leave energies concentrated a 3×5 window in crystals,
2375 and use shape and isolation information to distinguish genuine electrons and photons
2376 from noise. Electrons and photons are key to characterizing Standard Model pro-
2377 cesses and performing searches for new physics, and this represents one of the many
2378 upgrades of the CMS detector in preparation for Phase-2. With the ongoing Run-3
2379 data collecting period, and wealth of ongoing and scheduled upgrades, there remains
2380 an abundance of directions for detector development and physics at CMS heading
2381 into Phase-2 of the LHC.

Bibliography

- [1] Paul H. Frampton. Journeys Beyond the Standard Model. 54(1):52–52. ISSN 0031-9228. doi: 10.1063/1.1349615. URL <https://doi.org/10.1063/1.1349615>. eprint: https://pubs.aip.org/physicstoday/article-pdf/54/1/52/11109432/52_1_online.pdf.
- [2] Meinard Kuhlmann. Quantum Field Theory. In Edward N. Zalta and Uri Nodelman, editors, *The Stanford Encyclopedia of Philosophy*. Metaphysics Research Lab, Stanford University, Summer 2023 edition, 2023.
- [3] Steven Weinberg. The Making of the Standard Model. *Eur. Phys. J. C*, 34:5–13, 2004. URL <https://cds.cern.ch/record/799984>.
- [4] Christopher G. Tully. *Elementary Particle Physics in a Nutshell*. Princeton University Press, Princeton, 2012. ISBN 9781400839353. doi: doi:10.1515/9781400839353. URL <https://doi.org/10.1515/9781400839353>.
- [5] John Ellis. Higgs Physics. In *2013 European School of High-Energy Physics*, pages 117–168, 2015. doi: 10.5170/CERN-2015-004.117.
- [6] David Curtin, Rouven Essig, Stefania Gori, and Others. Exotic decays of the 125 GeV Higgs boson. *Phys. Rev. D*, 90:075004, Oct 2014. doi: 10.1103/PhysRevD.90.075004. URL <https://link.aps.org/doi/10.1103/PhysRevD.90.075004>.
- [7] Tania Robens, Tim Stefański, and Jonas Wittbrodt. Two-real-scalar-singlet

- 2401 extension of the SM: LHC phenomenology and benchmark scenarios. *Eur. Phys.*
2402 *J. C*, 80(2):151, 2020. doi: 10.1140/epjc/s10052-020-7655-x.
- 2403 [8] CERN. The history of CERN, 2024. URL <https://timeline.web.cern.ch/timeline-header/89>.
- 2404
2405 [9] R. Schmidt. Accelerator physics and technology of the LHC. In *ROXIE: Routine*
2406 *for the Optimizazation of Magnet X-Sections, Inverse Field Calculation and Coil*
2407 *End Design*, pages 7–17, 1998.
- 2408 [10] J. Vollaire et al. *Linac4 design report*, volume 6/2020 of *CERN Yellow Reports: Monographs*. CERN, Geneva, 9 2020. ISBN 978-92-9083-579-0, 978-92-9083-580-6. doi: 10.23731/CYRM-2020-006.
- 2409
2410
2411 [11] Antonella Del Rosso. Aerial view of the LHC and the four major experiments.
2412 2017. URL <https://cds.cern.ch/record/2253966>. General Photo.
- 2413 [12] ATLAS Collaboration. ATLAS: Detector and physics performance technical
2414 design report. Volume 1. 5 1999.
- 2415 [13] CMS Collaboration. CMS Physics: Technical Design Report Volume 1: Detector
2416 Performance and Software. 2006.
- 2417 [14] L Musa. Conceptual Design Report for the Upgrade of the ALICE ITS. Technical
2418 report, CERN, Geneva, 2012. URL <https://cds.cern.ch/record/1431539>.
- 2419 [15] S. Amato et al. LHCb technical proposal: A Large Hadron Collider Beauty
2420 Experiment for Precision Measurements of CP Violation and Rare Decays. 2
2421 1998.
- 2422 [16] Werner Herr and B Muratori. Concept of luminosity. 2006. doi: 10.5170/
2423 CERN-2006-002.361. URL <https://cds.cern.ch/record/941318>.

- 2424 [17] Olivier S. Brning and Frank Zimmerman. Parameter space for the LHC lumi-
2425 nosity upgrade. ISBN 978-3-95450-115-1. URL <https://accelconf.web.cern.ch/IPAC2012/papers/moppc005.pdf>.
- 2427 [18] CMS Collaboration. Pileup mitigation at CMS in 13 TeV data. *JINST*, 15(09):
2428 P09018, 2020. doi: 10.1088/1748-0221/15/09/P09018.
- 2429 [19] CMS Collaboration. Measurement of the inelastic proton-proton cross section at
2430 $\sqrt{s} = 13$ TeV. *JHEP*, 07:161, 2018. doi: 10.1007/JHEP07(2018)161.
- 2431 [20] CMS Collaboration. High-Luminosity Large Hadron Collider (HL-LHC): Tech-
2432 nical design report. 10/2020, 12 2020. doi: 10.23731/CYRM-2020-0010.
- 2433 [21] CMS Collaboration. The CMS Experiment at the CERN LHC. *JINST*, 3:S08004,
2434 2008. doi: 10.1088/1748-0221/3/08/S08004.
- 2435 [22] CMS Collaboration. Particle-flow reconstruction and global event description
2436 with the CMS detector. *JINST*, 12(10):P10003, 2017. doi: 10.1088/1748-0221/
2437 12/10/P10003.
- 2438 [23] V Karimki, M Mannelli, P Siegrist, H Breuker, A Caner, R Castaldi, K Freudens-
2439 reich, G Hall, R Horisberger, M Huhtinen, and A Cattai. *The CMS tracker*
2440 *system project: Technical Design Report*. Technical design report. CMS. CERN,
2441 Geneva, 1997. URL <https://cds.cern.ch/record/368412>.
- 2442 [24] The Phase-2 Upgrade of the CMS Tracker. Technical report, CERN, Geneva,
2443 2017. URL <https://cds.cern.ch/record/2272264>.
- 2444 [25] CMS Collaboration. CMS Technical Design Report for the Pixel Detector Up-
2445 grade. 9 2012. doi: 10.2172/1151650.
- 2446 [26] R. L. Workman and Others. Review of particle physics. 2022:083C01. doi:
2447 10.1093/ptep/ptac097.

- 2448 [27] CMS Technical Design Report for the Phase 1 Upgrade of the Hadron Calorime-
2449 ter. 9 2012. doi: 10.2172/1151651.
- 2450 [28] CMS Technical Design Report for the Level-1 Trigger Upgrade. 6 2013.
- 2451 [29] S. Dasu et al. CMS. The TriDAS project. Technical design report, vol. 1: The
2452 trigger systems. 12 2000.
- 2453 [30] CMS Collaboration. The Phase-2 Upgrade of the CMS Data Acquisition and
2454 High Level Trigger. Technical report, CERN, Geneva, 2021. URL <https://cds.cern.ch/record/2759072>. This is the final version of the document, approved
2455 by the LHCC.
- 2456 [31] C. Foudas. The CMS Level-1 Trigger at LHC and Super-LHC. In *34th Interna-*
2457 *tional Conference on High Energy Physics*, 10 2008.
- 2458 [32] CMS Software Guide. High Level Trigger (TWiki), 2024. URL <https://twiki.cern.ch/twiki/bin/view/CMSPublic/SWGuideHighLevelTrigger>.
- 2459 [33] The Worldwide LHC Computing Grid. 2012. URL <https://cds.cern.ch/record/1997398>.
- 2460 [34] Douglas Thain, Todd Tannenbaum, and Miron Livny. Distributed computing in
2461 practice: the Condor experience. *Concurrency and Computation: Practice and*
2462 *Experience*, 17(2-4):323–356, 2005. doi: <https://doi.org/10.1002/cpe.938>. URL
2463 <https://onlinelibrary.wiley.com/doi/abs/10.1002/cpe.938>.
- 2464 [35] Alexandre Zabi, Jeffrey Wayne Berryhill, Emmanuelle Perez, and Alexander D.
2465 Tapper. The Phase-2 Upgrade of the CMS Level-1 Trigger. 2020.
- 2466 [36] Technical proposal for a MIP timing detector in the CMS experiment Phase 2
2467 upgrade. Technical report, CERN, Geneva, 2017. URL <https://cds.cern.ch/record/2296612>.

- 2472 [37] CMS Collaboration. CMS luminosity measurement for the 2016 data-taking
2473 period. CMS Physics Analysis Summary CMS-PAS-LUM-17-001, 2017. URL
2474 <https://cds.cern.ch/record/2257069>.
- 2475 [38] CMS Collaboration. CMS luminosity measurement for the 2017 data-taking
2476 period at $\sqrt{s} = 13$ TeV. CMS Physics Analysis Summary CMS-PAS-LUM-17-
2477 004, 2018. URL <https://cds.cern.ch/record/2621960>.
- 2478 [39] CMS Collaboration. CMS luminosity measurement for the 2018 data-taking
2479 period at $\sqrt{s} = 13$ TeV. CMS Physics Analysis Summary CMS-PAS-LUM-18-
2480 002, 2019. URL <https://cds.cern.ch/record/2676164>.
- 2481 [40] CMS LUMI Group. CMS Luminosity Public Results (TWiki), 2024. URL <https://twiki.cern.ch/twiki/bin/view/CMSPublic/LumiPublicResults>.
- 2483 [41] Cécile Caillol, Pallabi Das, Sridhara Dasu, Pieter Everaerts, Stephanie Kwan,
2484 Isobel Ojalvo, and Ho-Fung Tsoi. CMS AN-20-213 (internal): Search for an
2485 exotic decay of the 125 GeV Higgs boson to light pseudoscalars, with a pair of b
2486 jets and a pair of tau leptons in the final state, 2020.
- 2487 [42] CMS Collaboration. Search for exotic decays of the Higgs boson to a pair of
2488 pseudoscalars in the $\mu\mu bb$ and $\tau\tau bb$ final states. *European Physical Journal C*,
2489 2 2024.
- 2490 [43] J. Alwall, R. Frederix, S. Frixione, et al. The automated computation of tree-
2491 level and next-to-leading order differential cross sections, and their matching to
2492 parton shower simulations. *Journal of High Energy Physics*, 2014(7), July 2014.
2493 ISSN 1029-8479. doi: 10.1007/jhep07(2014)079. URL [http://dx.doi.org/10.1007/JHEP07\(2014\)079](http://dx.doi.org/10.1007/JHEP07(2014)079).
- 2495 [44] R. Frederix, S. Frixione, V. Hirschi, et al. The automation of next-to-leading
2496 order electroweak calculations. *Journal of High Energy Physics*, 2018(7), July

- 2497 2018. ISSN 1029-8479. doi: 10.1007/jhep07(2018)185. URL [http://dx.doi.org/10.1007/JHEP07\(2018\)185](http://dx.doi.org/10.1007/JHEP07(2018)185).
- 2499 [45] S. Agostinelli, J. Allison, K. Amako, et al. Geant4 - a simulation toolkit. 506(3):
2500 250–303. ISSN 0168-9002. doi: 10.1016/S0168-9002(03)01368-8. URL <https://www.sciencedirect.com/science/article/pii/S0168900203013688>.
- 2502 [46] CMS Collaboration. An embedding technique to determine $\tau\tau$ backgrounds
2503 in proton-proton collision data. *JINST*, 14(06):P06032, 2019. doi: 10.1088/
2504 1748-0221/14/06/P06032.
- 2505 [47] CMS Collaboration. Search for neutral MSSM Higgs bosons decaying to a pair of
2506 tau leptons in pp collisions. *JHEP*, 10:160, 2014. doi: 10.1007/JHEP10(2014)160.
- 2507 [48] CMS Collaboration. Measurements of Higgs boson production in the decay chan-
2508 nel with a pair of τ leptons in proton-proton collisions at $\sqrt{s} = 13$ TeV. *Eur.*
2509 *Phys. J. C*, 83(7):562, 2023. doi: 10.1140/epjc/s10052-023-11452-8.
- 2510 [49] CMS Collaboration. Reconstruction and identification of tau lepton decays to
2511 hadrons and tau neutrinos at CMS. *Journal of Instrumentation*, 11(01):P01019–
2512 P01019, January 2016. ISSN 1748-0221. doi: 10.1088/1748-0221/11/01/p01019.
2513 URL <http://dx.doi.org/10.1088/1748-0221/11/01/P01019>.
- 2514 [50] CMS Collaboration. Performance of τ -lepton reconstruction and identification
2515 in CMS. *Journal of Instrumentation*, 7(01):P01001, jan 2012. doi: 10.1088/
2516 1748-0221/7/01/P01001. URL <https://dx.doi.org/10.1088/1748-0221/7/01/P01001>.
- 2518 [51] CMS Collaboration. Performance of reconstruction and identification of τ leptons
2519 decaying to hadrons and ν_τ in pp collisions at $\sqrt{s} = 13$ TeV. *JINST*, 13(10):
2520 P10005, 2018. doi: 10.1088/1748-0221/13/10/P10005.

- 2521 [52] CMS Collaboration. Identification of hadronic tau lepton decays using a deep
2522 neural network. *JINST*, 17:P07023, 2022. doi: 10.1088/1748-0221/17/07/
2523 P07023.
- 2524 [53] CMS Collaboration. Performance of CMS muon reconstruction in pp collision
2525 events at $\sqrt{s} = 7$ TeV. *Journal of Instrumentation*, 7(10):P10002–P10002,
2526 October 2012. ISSN 1748-0221. doi: 10.1088/1748-0221/7/10/p10002. URL
2527 <http://dx.doi.org/10.1088/1748-0221/7/10/P10002>.
- 2528 [54] CMS Collaboration. Performance of electron reconstruction and selection with
2529 the CMS detector in proton-proton collisions at $\sqrt{s} = 8$ TeV. *Journal of Instru-*
2530 *mentation*, 10(06):P06005, 2015. doi: 10.1088/1748-0221/10/06/P06005. URL
2531 <https://dx.doi.org/10.1088/1748-0221/10/06/P06005>.
- 2532 [55] CMS Collaboration. Identification of b-quark jets with the CMS experiment.
2533 *Journal of Instrumentation*, 8(04):P04013–P04013, April 2013. ISSN 1748-
2534 0221. doi: 10.1088/1748-0221/8/04/p04013. URL <http://dx.doi.org/10.1088/1748-0221/8/04/P04013>.
- 2536 [56] CMS Collaboration. Pileup Removal Algorithms. Technical report, CERN,
2537 Geneva, 2014. URL <https://cds.cern.ch/record/1751454>.
- 2538 [57] CMS Collaboration. CMS Phase 1 heavy flavour identification performance and
2539 developments. 2017. URL <https://cds.cern.ch/record/2263802>.
- 2540 [58] CMS Collaboration. Performance of the DeepJet b tagging algorithm using 41.9
2541 fb^{-1} of data from proton-proton collisions at 13 TeV with Phase 1 CMS detector.
2542 2018. URL <https://cds.cern.ch/record/2646773>.
- 2543 [59] Lorenzo Bianchini, John Conway, Evan Klose Friis, and Christian Veelken. Re-
2544 construction of the Higgs mass in $H \rightarrow \tau\tau$ Events by Dynamical Likelihood

- 2545 techniques. *Journal of Physics: Conference Series*, 513(2):022035, jun 2014.
2546 doi: 10.1088/1742-6596/513/2/022035. URL <https://dx.doi.org/10.1088/1742-6596/513/2/022035>.
- 2548 [60] CMS Collaboration. Evidence for the 125 GeV Higgs boson decaying to a pair
2549 of τ leptons. *JHEP*, 05:104, 2014. doi: 10.1007/JHEP05(2014)104.
- 2550 [61] CMS Collaboration. Missing transverse energy performance of the CMS detector.
2551 *JINST*, 6:P09001, 2011. doi: 10.1088/1748-0221/6/09/P09001.
- 2552 [62] Artur Kalinowski. CMS AN-19-032 (internal): Reconstruction of a τ pair invariant
2553 mass with a simplified likelihood scan, 2019.
- 2554 [63] CMS TAU POG. Tau Physics Object Group: Tau ID Recommendation For Run 2, 2024. URL <https://twiki.cern.ch/twiki/bin/view/CMS/TauIDRecommendationForRun2>.
- 2557 [64] CMS MUO POG. Muon Physics Object Group: Recommendations, 2024. URL
2558 <https://twiki.cern.ch/twiki/bin/view/CMS/MuonPOG>.
- 2559 [65] CMS MUO POG. Muon Physics Object Group: Reference guidelines and results
2560 for muon momentum scale and resolution in Run II, 2024. URL <https://twiki.cern.ch/twiki/bin/view/CMS/MuonReferenceScaleResolRun2>.
- 2562 [66] CMS HTT working group. Higgs To Tau Tau Working TWiki for the full Run-
2563 2 legacy analysis, 2024. URL <https://twiki.cern.ch/twiki/bin/view/CMS/HiggsToTauTauWorkingLegacyRun2>.
- 2565 [67] CMS ELE POG. Electron Physics Object Group: Recommendations,
2566 2024. URL <https://twiki.cern.ch/twiki/bin/view/CMS/EgammaRunIIRecommendations>.

- 2568 [68] CMS ELE POG. Electron Physics Object Group: Recommendations for
2569 2016 to 2018 UL, 2024. URL <https://twiki.cern.ch/twiki/bin/view/CMS/EgammaUL2016To2018>.
2570
- 2571 [69] CMS TAU Embedding Group. Tau embedded samples using 2016
2572 data, 2024. URL <https://twiki.cern.ch/twiki/bin/view/CMS/TauTauEmbeddingSamples2016Legacy>.
2573
- 2574 [70] CMS TAU Embedding Group. Tau embedded samples using 2017
2575 data, 2024. URL <https://twiki.cern.ch/twiki/bin/viewauth/CMS/TauTauEmbeddingSamples2017>.
2576
- 2577 [71] CMS TAU Embedding Group. Tau embedded samples using 2018
2578 data, 2024. URL <https://twiki.cern.ch/twiki/bin/viewauth/CMS/TauTauEmbeddingSamples2018>.
2579
- 2580 [72] Tau Lepton Run 2 Trigger Performance. 2019. URL <https://cds.cern.ch/record/2678958>.
2581
- 2582 [73] CMS Taus High Level Trigger Studies. Tau Lepton Run 2 Trigger Performance
2583 (CMS DP-2019/012), 2024. URL <https://twiki.cern.ch/twiki/bin/view/CMSPublic/HLTTauAllRun2>.
2584
- 2585 [74] Muon HLT Performance with 2018 Data. 2018. URL <https://cds.cern.ch/record/2627469>.
2586
- 2587 [75] Single and Double Electron Trigger Efficiencies using the full Run 2 dataset.
2588 2020. URL <https://cds.cern.ch/record/2888577>.
2589
- 2590 [76] Run II Trigger Performance For $e\mu$ Triggers. 2019. URL <https://cds.cern.ch/record/2687013>.

- 2591 [77] Performance of electron and photon reconstruction in Run 2 with the CMS ex-
2592 periment. 2020. URL <https://cds.cern.ch/record/2725004>.
- 2593 [78] CMS Collaboration. Performance of the CMS muon detector and muon recon-
2594 struction with proton-proton collisions at $\sqrt{s} = 13$ TeV. *JINST*, 13(06):P06015,
2595 2018. doi: 10.1088/1748-0221/13/06/P06015.
- 2596 [79] Piet Verwilligen. Muons in the cms high level trigger system. *Nuclear
2597 and Particle Physics Proceedings*, 273-275:2509–2511, 2016. ISSN 2405-6014.
2598 doi: <https://doi.org/10.1016/j.nuclphysbps.2015.09.441>. URL <https://www.sciencedirect.com/science/article/pii/S240560141500930X>. 37th Interna-
2599 tional Conference on High Energy Physics (ICHEP).
2600
- 2601 [80] Muon tracking performance in the CMS Run-2 Legacy data using the tag-and-
2602 probe technique. 2020. URL <https://cds.cern.ch/record/2724492>.
- 2603 [81] V.M. Abazov, B. Abbott, M. Abolins, et al. A novel method for modeling the
2604 recoil in W boson events at hadron colliders. *Nuclear Instruments and Methods
2605 in Physics Research Section A: Accelerators, Spectrometers, Detectors and Asso-
2606 ciated Equipment*, 609(2):250–262, 2009. ISSN 0168-9002. doi: <https://doi.org/10.1016/j.nima.2009.08.056>. URL <https://www.sciencedirect.com/science/article/pii/S0168900209016623>.
- 2607 [82] CMS Collaboration. Search for an exotic decay of the Higgs boson to a pair
2608 of light pseudoscalars in the final state with two b quarks and two τ leptons in
2609 proton-proton collisions at $\sqrt{s} = 13$ TeV. *Phys. Lett. B*, 785:462, 2018. doi:
2610 10.1016/j.physletb.2018.08.057.
- 2611 [83] CMS LUMI POG. Luminosity Physics Object Group: Recommendations, 2024.
2612 URL <https://twiki.cern.ch/twiki/bin/view/CMS/TWikiLUM>.

- 2615 [84] The modeling of the top quark p_T (TWiki), 2024. URL <https://twiki.cern.ch/twiki/bin/view/CMS/TopPtReweighting>.
- 2617 [85] CMS BTV group. Methods to apply b-tagging efficiency scale fac-
2618 tors (TWiki), 2024. URL <https://twiki.cern.ch/twiki/bin/view/CMS/BTagShapeCalibration>.
- 2620 [86] CMS Collaboration. Jet energy scale and resolution in the CMS experiment in
2621 pp collisions at 8 TeV. *JINST*, 12(02):P02014, 2017. doi: 10.1088/1748-0221/
2622 12/02/P02014.
- 2623 [87] Garvita Agarwal. Jet Energy Scale and Resolution Measurements in CMS. *PoS*,
2624 ICHEP2022:652, 2022. doi: 10.22323/1.414.0652.
- 2625 [88] CMS JERC group. Jet Energy Corrections (TWiki), 2024. URL <https://twiki.cern.ch/twiki/bin/view/CMS/JECDataMC>.
- 2627 [89] CMS JERC group. Jet Energy Resolution (TWiki), 2024. URL <https://twiki.cern.ch/twiki/bin/view/CMS/JetResolution>.
- 2629 [90] CMS MUO POG. Muon Physics Object Group: Baseline muon selec-
2630 tions for Run-II, 2024. URL <https://twiki.cern.ch/twiki/bin/view/CMS/SWGuideMuonIdRun2>.
- 2632 [91] CMS ELE POG. Electron Identification Based on Simple Cuts, 2024. URL
2633 <https://twiki.cern.ch/twiki/bin/view/CMSPublic/EgammaPublicData>.
- 2634 [92] Jose Enrique Palencia Cortezon. Single top quark production at CMS. Technical
2635 report, CERN, Geneva, 2018. URL <https://cds.cern.ch/record/2640578>.
- 2636 [93] CMS Collaboration. Measurements of the electroweak diboson production cross
2637 sections in proton-proton collisions at $\sqrt{s} = 5.02$ TeV using leptonic decays.
2638 *Phys. Rev. Lett.*, 127(19):191801, 2021. doi: 10.1103/PhysRevLett.127.191801.

- 2639 [94] CMS Collaboration. A portrait of the Higgs boson by the CMS experiment
2640 ten years after the discovery. *Nature*, 607(7917):60–68, 2022. doi: 10.1038/
2641 s41586-022-04892-x.
- 2642 [95] CMS JERC group. Jet energy scale uncertainty sources (TWiki), 2024. URL
2643 <https://twiki.cern.ch/twiki/bin/view/CMS/JECUncertaintySources>.
- 2644 [96] TOP Systematic Uncertainties (Run 2) (TWiki), 2024. URL <https://twiki.cern.ch/twiki/bin/viewauth/CMS/TopSystematics>.
- 2645 [97] Kyle Cranmer. Practical Statistics for the LHC. In *2011 European School of
High-Energy Physics*, pages 267–308, 2014. doi: 10.5170/CERN-2014-003.267.
- 2646 [98] Elham Khazaie, Maryam Zeinali, Hamed Bakhshiansohi, and Abideh Jafari.
2647 CMS AN-21-058 (internal): Search for exotic decays of the Higgs boson to a
2648 pair of new light bosons with two muons and two b jets in the final states at
2649 $\sqrt{s} = 13$ TeV, 2021.
- 2650 [99] CMS Higgs Physics Analysis Group. Summary of 2HDM+S searches at 13 TeV
2651 (Run 2), 2024. URL <https://twiki.cern.ch/twiki/bin/view/CMSPublic/Summary2HDMSRun2>.